Final Report to

RPSEA
Research Partnership to Secure Energy for America

Integrated Experimental and Modeling Approaches to Studying the Fracture-Matrix Interaction in Gas Recovery from Barnett Shale

Project Number 09122-12

FINAL REPORT

February 28, 2014

Dr. Qinhong (Max) Hu (PI)
The University of Texas at Arlington
500 Yates Street
Arlington, TX 76019-0049
Phone: (817) 272-5398
E-mail: maxhu@uta.edu

Dr. Robert P. Ewing (co-PI)
Iowa State University
2101 Agronomy Hall
Ames, IA 50011-1010
Phone: (515) 294-7856
E-mail: ewing@iastate.edu

LEGAL NOTICE

This report was prepared by the University of Texas at Arlington as an account of work sponsored by the Research Partnership to Secure Energy for America, RPSEA. Neither RPSEA, members of RPSEA, the National Energy Technology Laboratory, the U.S. Department of Energy, nor any person acting on behalf of any of the entities:

a. MAKES ANY WARRANTY OR REPRESENTATION, EXPRESS OR IMPLIED WITH RESPECT TO ACCURANCY, COMPLETENESS, OR USEFULNESS OF THE INFORMATION CONTAINED IN THIS DOCUMENT, OR THAT THE USE OF ANY INFORMATION, APPARATUS, METHOD, OR PROCESS DISCLOSED IN THIS DOCUMENT MAY NOT INFRINGE PRIVATELY OWNED RIGHTS, OR

b. ASSUME ANY LIABILITY WITH RESECT TO THE USE OF, OR FOR ANY AND ALL DEMAGES RESULTING FROM THE USE OF, ANY INFORMATION, APPARATUS, METHOD, OR PROCESS DISCLOSED IN THIS DOCUMENT.

THIS IS A FINAL REPORT. THE DATA, CALCULATION, INFORMATION, CONCLUSION, AND/OR RECOMMENDATION REPORTED HEREIN ARE THE PROPERTY OF THE U.S. DEPARTMENT OF ENERGY.

REFERENCE TO TRADE NAMES OR SPECIFIC COMMERCIAL PRODUCTS, COMMODITIES, OR SERVICES IN THIS REPORT DOES NOT REPRESENT OR CONSTITUTE AN ENDORSEMENT, RECOMMENDATION, OR FAVORING BY RPSEA OR ITS CONTRACTORS OF THE SPECIFIC COMMERCIAL PRODUCT, COMMODITY, OR SERVICE.

This page intentionally left blank.

Signature and Date Stamp

(Max) Qinhong Hu, Ph.D.

Principal Investigator's signature:

Date: February 28, 2014

Table of Contents

Signature and Date Stamp 4

List of Acronyms 7

List of Figures 8

Executive Summary 13

Introduction 15

Task 1: Acquisition and Characterization of Shale Samples 17

Objectives 17

Methods 19

Results and Discussion 25

Task 2: Imbibition Tests 30

Objectives 30

Methods 31

Results and Discussion 32

Task 3: Edge-Only Accessible Porosity Distribution 34

Objectives 34

Methods 35

Results and Discussion 36

Task 4: Pore Structure Imaging using Wood's Metal Alloy Intrusion 40

Objectives 40

Methods 40

Results and Discussion 41

Task 5: Methane Sorption and Gas Diffusion in Crushed Shale 48

Objectives 48

Methods 49
Results and Discussion 53
Task 6: Fracture-Matrix Interaction in Intact Shale 56
Objectives 56
Methods 58
Results and Discussion 61
Task 7: Pore-Scale Network Modeling 69
Objectives 69
Methods 71
Results and Discussion 71
Conclusions 76
Acknowledgements 77
References 78
Impact on Producers 86
Technology Transfer Efforts 86
Peer-Reviewed Journal Publications 86
Conference Presentations 87
Invited Presentations to Academia and the Oil/Gas Industry 89
Media Coverage 90
Appendix 1 91

List of Acronyms

2-D	two-dimensional
3-D	three-dimensional
AAPG	American Association of Petroleum Geologists
ACS	American Chemical Society
AGU	American Geophysical Union
BEG	Bureau of Economic Geology
BET	Brunauer, Emmett and Teller
bgs	below ground surface
BJH	Barrett–Joyner–Halenda
DOE	Department of Energy
Empa	Swiss Federal Laboratories for Materials Science and Technology
GRI	Gas Research Institute
GSA	Geological Society of America
ICP–MS	inductively coupled plasma–mass spectrometry
ISU	Iowa State University
IUPAC	International Union of Pure and Applied Chemistry
LA	laser ablation
mcf	thousand cubic feet
MICP	mercury injection capillary pressure
NLDFT	Non-local Density Functional Theory
PI	principal investigator
psia	pounds per square inch absolute
RH	relative humidity
RPSEA	Research Partnership to Secure Energy for America
SCF	standard cubic feet
SEM	scanning electron microscopy
SPE	Society of Petroleum Engineers
UTA	the University of Texas at Arlington
XRD	x-ray diffraction

List of Figures

Figure 1. Photographs of shale and limestone core samples, taken from different depths in the Texas United Blakeley #1 well. 19

Figure 2. A MICP apparatus, the Micromeritics AutoPore IV 9510. 21

Figure 3. A nitrogen sorption isotherm apparatus, the Micromeritics Tristar® II 3020. 24

Figure 4. An apparatus for vacuum saturation. 25

Figure 5. Triplicate MICP measurements of a Barnett shale sample for pore-throat distribution. 27

Figure 6. MICP pore-throat distribution measurements on Barnett shale samples. 27

Figure 7. Comparison of pore-size distribution measurements by MICP and nitrogen sorption methods. N_2 A and B were analyzed at Saitama University, while N_2 Z was measured by the Quantachrome Instrument. 28

Figure 8. The apparatus for a fluid imbibition test. 32

Figure 9. Water imbibition results for a typical Barnett shale sample. 33

Figure 10. The LA–ICP–MS apparatus for micro-scale elemental mapping. 35

Figure 11. 3-D mapping results of non-sorbing perrhenate (ReO_4^-; mg/kg in the scale bar) by LA–ICP–MS for Barnett shale 7,136 ft (Forestburg limestone) sample; top to bottom layers are sampled at 2, 12, 54, and 224 µm from sample surface, respectively. This 2,000 µm × 2,000 µm grid was selected in the middle of a face of 15 mm-sided cube, and mapped with a 100 µm laser spot size and 200 µm spacing between spots. 37

Figure 12. Average concentrations of tracers vs. depth for Barnett shale 7,136 ft (Forestburg limestone); the dashed line indicates the slope expected from percolation theory. 38

Figure 13. 2-D mapping by LA–ICP–MS of non-sorbing perrhenate distribution from in a Barnett shale sample from 7,136 ft (Forestburg limestone). Laser spot size is 100 µm; spacing between spots is 500 µm; X and Y distances are in µm. 39

Figure 14. Mapped area of 10 mm × 5 mm for Figure 13 in a Barnett shale sample from 7,136 ft (Forestburg limestone). 39

Figure 15. SEM-BSE images of connective pores occupied by the alloy Wood's metal (bright graytone) in an Eagle Ford test shale sample at 600 bars. 42

Figure 16. SEM-BSE images of connective pores occupied by the alloy Wood's metal (bright graytone) in Barnett shale sample of 7,169 ft at 1,542 bars..... 43

Figure 17. SEM-BSE images of Wood's metal impregnated Barnett shale sample from 7,136 ft (Forestburg limestone) at 4,000 bars. 44

Figure 18. SEM-BSE images of Wood's metal impregnated Barnett shale sample from 7,219 ft (lower Barnett) at 6,000 bars. 45

Figure 19. Microscope images of micro-cracks in Barnett shale samples..... 46

Figure 20. 2-D mapping by LA–ICP–MS of Pb (lead) distribution in a Barnett shale sample from 7,136 ft (Forestburg limestone). Wood's metal alloy is high in Pb, so Pb concentration identifies porous regions that are connected to the sample's exterior. Laser spot size is 100 µm; spacing between spots is 500 µm..... 47

Figure 21. 2-D mapping by LA–ICP–MS of Pb (lead) distribution in a sample from 7,219 ft (lower Barnett) following Wood's metal alloy injection at 6,000 bars pressure. Laser spot size is 100 µm, and spacing between spots is 175 µm. 48

Figure 22. The BEG apparatus for measuring methane sorption isotherms. 49

Figure 23. An apparatus for measuring gas diffusion of crushed shale powder..... 51

Figure 24. Methane sorption as a function of pressure and temperature. For Y-axis, 1 mmol/g = 711.2 scf/ton. Experimental temperatures of 35.4, 50.4, and 65.4°C are equivalent to 95.7, 123, and 150°F. 54

Figure 25. Methane sorption and desorption as a function of pressure at 65.4°C (150°F)... 54

Figure 26. Measured oxygen concentration in natural log scale vs. experimental time for Barnett shale powder..... 55

Figure 27. Conceptual model of fracture-matrix interaction and resultant shale gas production (modified from Pflug, 2009)..... 57

Figure 28. Aqueous tracer imbibition penetration profile, mapped on the interior face, for the non-sorbing tracer ReO_4^- in Barnett shale 7,136 ft, the Forestburg limestone. Top (A) initially dry (imbibition time of 46.6 hr); Middle (B) equilibrated at 75% RH (imbibition time of 47.9 hr); and Bottom (C) equilibrated at 98% RH (imbibition time of 48.4 hr). Imbibition proceeded from left to right, and the X- and Y-scales are in µm. The LA–ICP–MS detection limit for Re in Barnett shales is about 0.05 mg/kg. 62

Figure 29. Aqueous tracer distribution, mapped on the imbibing face in the middle region of 15 mm×15 mm face, for non-sorbing tracer ReO_4^- in Barnett shale 7,136 ft (Forestburg limestone) under initially dry condition after imbibition time of 46.6 hr. The X- and Y-scales are in µm. 63

Figure 30. Aqueous tracer imbibition penetration profile, mapped on the interior face, for sorbing tracer Cs^+ in Barnett shale 7,136 ft (Forestburg limestone) under initially dry condition after an imbibition time of 46.6 hr. Imbibition proceeded from left to right, and the X- and Y-scales are in µm. Pink areas indicate a concentration below 2 mg/kg, and the Cs background level detected by LA–ICP–MS in Barnett shales is about 1.5 mg/kg. 64

Figure 31. Aqueous tracer imbibition penetration profile, mapped on the side face, for the non-sorbing tracer ReO_4^- in Barnett shale 7,136 ft (Forestburg limestone) under initial sample saturation equilibrated at 98% relative humidity after an imbibition time of 48.4 hr. Left side is the imbibition face, and the X- and Y-scales are in µm. 64

Figure 32. *n*-decane tracer imbibition penetration profile for non-sorbing tracer Re in Barnett shale 7,169 ft under initially dry condition at imbibition time of 72.2 hr. Left side is the imbibition face, and the X- and Y-scales are in µm. White areas indicate a concentration below 0.2 mg/kg. 65

Figure 33. Field Emission-SEM images of kerogen and mineral phases and associated pore spaces in Barnett shale 7,109 ft, obtained from UTA's Hitachi S-3000 variable pressure SEM. Figures 33A and 33B are shown at different observational scale bars and associated resolutions, with Figure 33B focusing on the kerogen area. 66

Figure 34. Diffusion profile and measured effective diffusion coefficient for non-sorbing tracer ReO_4^- in surface (sample exterior) and interior faces of Barnett shale 7,136 ft (Forestburg limestone); red dashed lines are the background levels (±1 standard deviation) of ReO_4^-. 67

Figure 35. Diffusion profile for non-sorbing tracer ReO_4^-on the sample's exterior (top panel; 500 µm spacing between spots) and interior (bottom panel; 150 µm spacing between spots) faces. Sample is Barnett shale from 7,136 ft (Forestburg limestone). 69

Figure 36. The drilling pad and 24 horizontal wells into the Barnett shale near UTA campus. 71

Figure 37. Gas production data from all 22 UTA wells in Tarrant County. Wells 1–6 went operational on Nov.-Dec. 2008, while the rest came online during or after April 2010. mcf: thousand cubic feet. 72

Figure 38. Gas production data in log-log scale from eleven UTA wells in Tarrant County. 73

Figure 39. Gas production data in log-log scale from the eight earliest Barnett Shale wells in Johnson County..... 74

List of Tables

Table 1: Barnett shale sample list and vacuum-saturation results 18

Table 2: MICP results for Barnett shale samples..... 26

Table 3: Barnett shale sample properties measured by nitrogen sorption isotherm 29

Table 4: Water imbibition slopes for Barnett shale samples 34

Table 5: Measured effective diffusion coefficient and tortuosity of Barnett shale powder as a function of water saturation 56

Table 6: Humidity and capillary pressure over saturated salt solutions at 22.5°C 59

Executive Summary

Fluid flow and mass transport are macroscopic consequences of the pore structure, which integrates geometry (e.g., pore size and shape, pore-size distribution) and topology (e.g., pore connectivity). The Barnett shale is a profitable gas play, but the current gas recovery rate is only about 10–30% of the estimated gas in place. Recovery in this extremely tight formation is limited by diffusive gas transport from the matrix storage to the stimulated fracture network. But there are no systematic studies, in the published literature, on pore connectivity in the Barnett shale and its effect on gas diffusion and production. Diffusion in poorly-connected pore spaces will be anomalous (non-Fickian) and unexpectedly slow, leading to steep decline and low gas recovery. The objectives of this work are to examine, and evaluate the implications of, low pore space connectivity on gas recovery in fractured shale, in the context of fracture-matrix interactions.

A suite of complementary and innovative experimental and modeling approaches is utilized to achieve the objectives. They include (1) acquisition and basic characterization of petrophysical properties (porosity, median pore diameter, pore-size distribution, permeability, etc.); (2) water imbibition studies to monitor spontaneous water uptake over time on samples of different shapes and different bedding plane orientation; (3) edge-only accessible porosity distribution using micro-scale Laser Ablation–Inductively Coupled Plasma–Mass Spectrometry (LA–ICP–MS) to map chemical tracers following full vacuum saturation; (4) pore structure imaging with scanning electron microscopy (SEM) and LA–ICP–MS elemental mapping after injecting molten Wood's metal alloy at high pressures; (5) methane sorption and gas (oxygen tracer) diffusion in crushed shale at different water saturations; (6) for cm-sized shale matrix samples, tracer diffusion under saturated conditions, and spontaneous tracer imbibition of both water (under three different initial saturations) and *n*-decane; and (7) pore-scale network modeling to simulate experimental results and link our findings regarding shale matrix pore connectivity and fracture-matrix interactions to field-scale gas production decline behavior.

We find that the Barnett shale, and likely other shales as well, have very limited edge-accessible pore spaces. This is shown from low pore connectivity behavior of fluid (water and *n*-decane) imbibition, steep decline of edge–accessible porosity from vacuum saturation, the heterogeneous presence of only trace (at about 1/100 of the released concentration) amount of

diffusing solutes beyond a few mm from a sample edge, and a limited connected pathways of Wood's metal alloy injected even under pressures of 4,000 and 6,000 bars. The extremely sensitive detection of Wood's metal component elements by LA–ICP–MS reveals that only about 1/1000 of edge-accessible porosity is connected in the sample interior, which is consistent with other experimental approaches and theoretical interpretation of pore connectivity based on percolation theory. This sparse, and limited, pore space connection within the shale matrix will lead to the limited fracture-matrix interactions in fractured shale, and consequently steep initial production decline and overall low recovery.

The outcomes of this project bridge knowledge gaps in nano-scale pore structure effects on macro-scale fluid migration in hydraulically stimulated shale formations, which can lead to the development of viable approaches to improving fluid productivity and associated economic benefits of unconventional resource utilization.

In addition to undergraduates, graduates, and postdocs of UTA, the scientists and organizations involved in performing this work include Stefan Dultz (University of Hannover, Germany), Josef Kaufmann (Swiss Federal Laboratories for Materials Science and Technology [Empa]), Shoichiro Hamamoto of Saitama University (now with the University of Tokyo) in Japan, and Tongwei Zhang of BEG–UT Austin. Key deliverables are peer–reviewed journal articles, presentations at scientific conferences (AAPG, ACS, AGU, GSA, SPE), academic institutions (BEG–UT Austin, Texas A&M University, University of Utah, University of Arizona, University of Texas at San Antonio, and Los Alamos National Laboratory) and oil/gas companies (ConocoPhillips and Baker Hughes), and project meetings and reports to RPSEA. DrillingInfo has provided complimentary access to its database to UTA for academic usage, and access to their database helps the work of linking our laboratory studies of physical and chemical processes underlying gas migration in fractured shale matrix to real-world, field-scale production.

Introduction

Natural gas is a widely-used fossil fuel consisting primarily of methane (70–90%), but often including significant quantities of ethane (5–15%), propane, butane, and pentane, plus carbon dioxide, nitrogen, helium, and hydrogen sulfide. Since 2000, the technological development of horizontal drilling and hydraulic fracturing in US has led to a dramatic increase in hydrocarbon (gas and oil) production from shale formations, changing the energy landscape in the US and worldwide (DOE, 2009; Jarvie, 2012; EIA, 2014).The production of shale gas has significantly increased, and it is predicted that shale gas will become the source of 50% of total dry gas production in the USA by 2040, an increase from 34% in 2011 (EIA, 2014).

Despite the increased gas and oil production from shale formations, analysis of data from 65,000 shale wells in 30 shale-gas and 21 tight-oil fields in the US led Hughes (2013a, b) to argue that the shale revolution will be hard to sustain. The data indicated that production from a given well declines rapidly within a few years. For example, the top five US plays typically produced 80–95% less gas after 3 years, and the productivity of new wells in two leading tight-oil plays (Bakken and Eagle Ford) dropped by about 60% within the first year. Total gas recovery from the Barnett, the most developed shale play, was reported to be only 8–15% of gas in place in 2002 (Curtis, 2002), and 12–30% in 2012 (King, 2012), even with hydraulic stimulation. While Hughes' articles (2013a, b) mention this steep decline and low overall recovery, investigations into their root cause(s) are surprisingly scarce (Hu and Ewing, 2013); **this work highlights these root causes**.

Located under at least 17 counties of the Fort Worth Basin in north-central Texas, the Barnett shale is a Mississippian-age marine shelf deposit, ranging in thickness from about 60 m (200 feet) in the southwest region to 305 m (1000 feet) to the northeast. The Barnett Formation can be divided into three members: the upper Barnett section, the Forestburg limestone (where present), and the lower Barnett section. The upper and lower Barnett sections mainly consist of a variety of siliceous mudstones with less abundant interbedded lime mudstones and skeletal packstones, while the Forestburg section is a laminated, argillaceous lime mudstone (Loucks and Ruppel, 2007). The upper and lower sections area black, organic-rich shale with extremely low permeability (0.07–5 μD, micro-darcy) (Grieser et al., 2008). Powder X-ray diffraction (XRD)

analyses of 35 cuttings from three wells in Wise and Denton counties give the following shale composition by weight: 45–55% silts (mostly quartz with some plagioclase); 15–25% carbonates (mostly calcite, with some dolomite and siderite); 20–35% clay minerals; and 2–6% pyrite (Loucks and Ruppel, 2007; Zhao et al., 2007). Total organic carbon ranges from 3.5 to 4.5% by weight, which translates to 7–9% by volume because the organic matter has a lower density than the minerals. Organic matter in the shale is mainly type II kerogen, which can generate both oil and gas directly (Zhao et al., 2007).

In Wise County, the Barnett shale has a net thickness of 50–200 ft, TOC 4.5%, gas-filled porosity of 2.5%, water-filled porosity of 1.9%, and adsorbed gas content of 20% (Curtis, 2002). The 120 foot long (37 m) Texas United Blakely #1 core, taken from Wise County within the Fort Worth Basin, includes part of the upper Barnett section (7105 to 7117 ft below ground surface (bgs), the Forestburg limestone (7,117 to 7,155 ft bgs), and the upper part of the lower Barnett section (7,155 to 7,225 ft bgs) (Loucks and Ruppel, 2007). Loucks and Ruppel (2007) also found a well-developed hardground at 7,198 ft bgs (2193 m) in the Blakely core, and noted that this hardground has well-developed phosphate-coated grains (ooids) and massive pyrite replacement.

The Barnett shale currently has some16,000 producing wells (EIA, 2011; Browning et al., 2013). The reservoir produces at commercially viable levels only with hydraulic fracturing that establishes long and wide fractures, which connect large surface areas of the formation through a complex fracture network. However, gas production in such tight shale is still technically challenging, partly from the lack of the understanding of nanopore structure characteristics of shale matrix.

Fluid flow and solute transport in rock are macroscopic consequences of the pore structure, which integrates geometry (e.g., pore size and shape, pore-size distribution; Bear, 1972) and topology (e.g., pore connectivity; Dullien, 1992). Especially when pore connectivity is low, topological factors outweigh the better-known geometrical factors (Ewing and Horton, 2002; Hu et al., 2002; Hunt et al., 2014). However, the prevalence of low pore connectivity in some rocks (for example, tight shales), and its impacts on fluid flow and chemical transport, are poorly documented and understood.

Understanding the pore structure of these extremely low-permeability reservoirs (often in the nano-darcy [nD] range) has been a challenging task, due to limitations of applicable characterization tools and techniques. Recently the Barnett shale, one of the world's most successful unconventional reservoirs, has been the subject of several studies incorporating different approaches to investigating pore structure characteristics. For example, Slatt and O'Brien (2011) characterized the pore types of the Barnett and Woodford gas shales using scanning electron microscopy. Chalmers et al. (2012) investigated the pore systems of Barnett shale using multiple approaches, including mercury injection capillary pressure (MICP). In addition, Hu et al. (2012) investigated the low pore connectivity of Barnett shale using spontaneous water imbibition, tracer concentration profiles, and imaging in combination with pore network modeling.

Gas movement in tight shale is mainly by diffusion, with rates limited by tortuous pathways through sparsely-connected nano-sized pores. Chemical diffusion in sparsely-connected pore spaces is not well described by classical Fickian behavior; rather, anomalous diffusion is suggested by percolation theory (Hunt and Ewing, 2009; Ewing et al., 2010; Hu et al., 2012).This work studies the pore connectivity and resultant tortuous fluid migration pathways in the Barnett shale using complementary laboratory experiments and network modeling, and gas production decline behavior analyses of field data. The text below documents the objectives and methods, and presents results and discussion for the tasks of the project.

Task 1: Acquisition and Characterization of Shale Samples

Objectives

Although the lithological layers in the Barnett shale vary somewhat in thickness, the upper and lower Barnett sections are relatively uniform at ~30 m and ~91 m, respectively. The term "Barnett shale" is somewhat of a misnomer, as the formation is composed of various mudstones; nonetheless in this report we will use the term "shale" except when distinguishing between the siliceous and lime mudstone members. Core samples from the Barnett Formation in the Ft. Worth area were obtained from the core repository of the Texas Bureau of Economic Geology (BEG). All samples are from the Texas United Blakely #1 well (API 497–33041) in southeastern

Wise County. Samples secured for this work were from five different depths:7,109 ft (2,167 m) (upper Barnett), 7,136 ft (2,175 m) (Forestburg limestone), and 7,169 ft (2,185 m), 7,199 ft (2,194 m) and 7,219 ft (2,200 m) (upper part of the lower Barnett) (Table 1). A detailed elemental analysis is given in Appendix 1.

Table 1: Barnett shale sample list and vacuum-saturation results

Depth (replicates)	Porosity† (%)	Bulk density (g/cm^3)	Particle density (g/cm^3)
7,109 ft (2,167 m) (N=5)	2.77±0.98	2.31±0.04	2.38±0.04
7,136 ft (2,175 m) (N=6)	1.27±0.24	2.52±0.06	2.56±0.07
7,169 ft (2,185 m) (N=6)	3.08±0.84	2.40±0.06	2.47±0.07
7,199 ft (2,194 m) (N=6)	3.77±1.21	2.25±0.05	2.34±0.06
7,219 ft (2,200 m) (N=6)	2.67±1.15	2.40±0.07	2.47±0.08

†Average ± standard deviation for replicate measurements on the same sample depth.

Photographs of the core samples are shown in Figure 1.

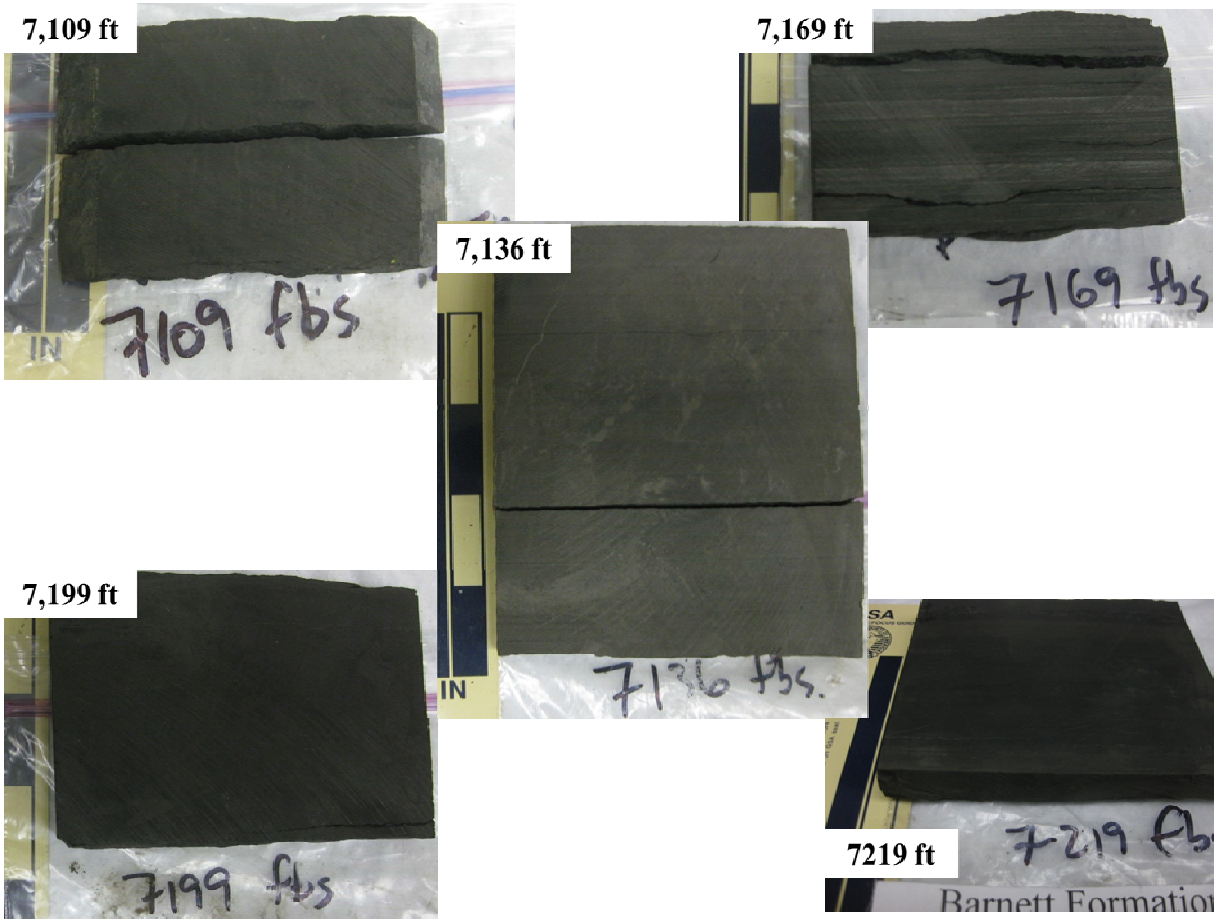

Figure 1. Photographs of shale and limestone core samples, taken from different depths in the Texas United Blakeley #1 well.

Methods

Initial characterization of core samples includes the measurement of porosity, particle and bulk density, permeability, and pore-size distribution. Porosity and pore-size distribution were analyzed using the mercury intrusion porosimeter (AutoPore IV 9510) manufactured by Micromeritics Instrument Corporation (Norcross, GA). Mercury injection capillary pressure (MICP) is applicable to pore-throat size measurements from 3 nm up to 300 µm in diameter. The approach of MICP can also indirectly evaluate other pore characteristics, such as total pore surface area, permeability, and tortuosity.

As a non-wetting fluid to most porous media, mercury will not invade pores unless an external pressure is applied. The diameter of the pore-throats invaded by mercury is inversely proportional to the applied pressure; the higher the applied pressure, the smaller are the pores invaded by mercury. Washburn (1921) developed the following equation based on the assumption that all the pores are cylindrical in shape:

$$\boldsymbol{\Delta P} = -\frac{2\gamma cos\theta}{\boldsymbol{R}} \quad (1)$$

where $\boldsymbol{\Delta P}$ is the pressure difference across the curved mercury interface; γ is the surface tension of mercury; θ is the contact angle between mercury and the porous medium; $\boldsymbol{R}$ is the corresponding pore-throat radius. Using γ=485 dynes/cm and θ=130°, equation (1) becomes

$$\boldsymbol{\Delta P} = \frac{90.43}{\boldsymbol{R}} \quad (2)$$

with $\boldsymbol{\Delta P}$ in psia and $\boldsymbol{R}$ in micrometers (μm).

Each shale sample (rectangular prisms with the largest linear dimension about 15 mm) was oven-dried at 60 °C for at least 48 hours to remove moisture, then cooled to room temperature (~23°C) in a desiccator with less than10% RH before the MICP test. Samples were then evacuated to 50 μmHg (0.05 torr, 0.000972 psi, or 6.7 Pa). During a MICP test, each sample underwent both low-pressure and high-pressure analyses. The highest pressure produced by our Micromeritics AutoPore IV 9510 (Figure 2) is 60,000 psia (413 MPa), corresponding (via the Washburn equation) to a pore-throat diameter of about 3 nm. Under low-pressure analysis, the largest pore-throat diameter recorded by MICP is about 300 μm. Equilibration time (the minimum time elapsed to achieve a stable mercury volume before proceeding to the next pressure; the instrument is capable of detecting a miniscule mercury change of 0.1 μL) was chosen to be 50 seconds.

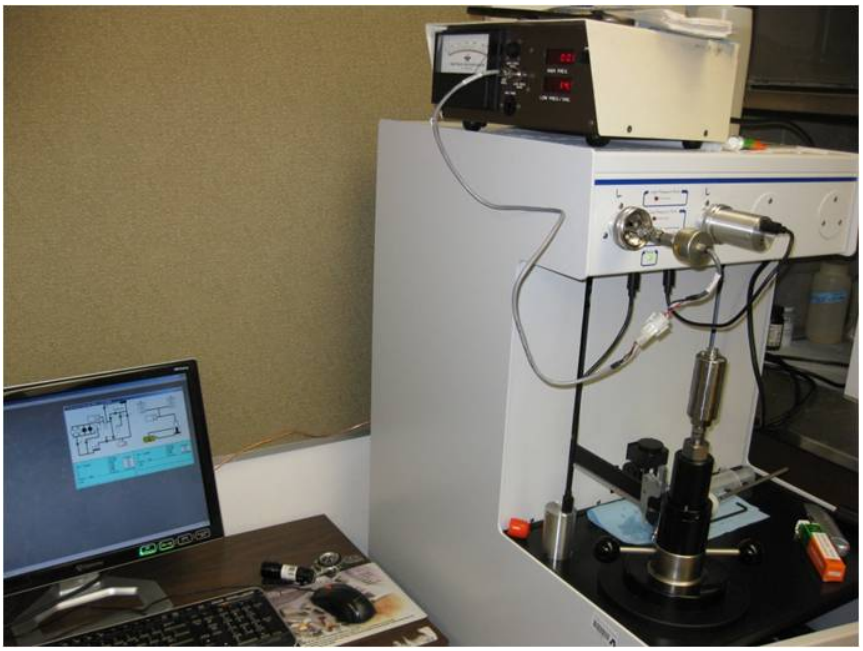

Figure 2. A MICP apparatus, the Micromeritics AutoPore IV 9510.

As reported by Gao and Hu (2013), porosity, median pore-throat diameter, and permeability for the shale samples were calculated by the method of Katz and Thompson (1986; 1987), and tortuosity by Hager (1998) and Webb (2001). Using percolation theory, Katz and Thompson (1986) developed a theoretical relationship (Equation 3) between permeability and critical pore diameter for sedimentary (sandstones and carbonates) rock.

$$k = \frac{1}{226} L_c^2 \frac{\sigma}{\sigma_0} \tag{3}$$

where k= absolute permeability (m^2), L_c=critical pore diameter (m) corresponding to the critical/threshold pressure when mercury spans the sample, σ/σ_0= conductivity formation factor (or conductance ratio; dimensionless), σ=conductivity of bulk rock (S/m), and σ_0=conductivity of pore solution (S/m). The concrete work of Halamickova et al. (1995) found that a constant of 1/226 was good for cement paste of 0.50 water to cement ratio, but a value of 1/180 for the water to cement ratio of 0.40 gave a better correlation between measured and calculated permeability.

The formation factor can also be calculated from pore parameters of mercury intrusion experiments by Equation 4 proposed by Katz and Thompson (1987).

$$\frac{\sigma}{\sigma_0} = \frac{L_{\max}}{L_c} \phi S(L_{\max}) \tag{4}$$

where L_{max}=pore diameter (m) at which hydraulic conductance (from the derivative plot of dV/dP, the differential of volume vs. pressure change) is the maximum ϕ=total porosity, and $S(L_{max})$=fractional volume of pores larger than L_{max}.

Furthermore, formation factor which considers tortuosity and constrictivity of the porous media, can be used to evaluate chemical diffusion (Equation 5; see Task 5 for diffusion), considering the relationship of conductivity and diffusivity by Nernst–Einstein equation (e.g., Nokken and Hooton, 2003).

$$\frac{\sigma}{\sigma_0} = \frac{D_0}{D_e} \tag{5}$$

There is widespread use of the Katz and Thompson (1986; 1987) approach to measuring permeability, especially in cement and concrete, which like shales have very low permeability (Garboczi, 1990; Eldieb and Hooton, 1994; Tumidajski and Lin, 1998; Nokken and Hooton, 2003). Comparatively, the utility of MICP data to evaluate tortuosity is less reported; one publication is to assess the drug release from matrix tablet (Crowley, 2003).

At a given pressure, the incremental mercury intrusion volume corresponds to pore throats that are both (1) invadable by mercury at this pressure and (2) connected to the mercury reservoir surrounding the sample. This connectivity constraint means that MICP gives a different pore-size distribution than does the N_2sorption isotherm method, and more information is obtained from both together than from either one alone. While MICP is widely accepted as the standard approach in determining pore-size distribution, the ink-bottle phenomenon (large pores connected by smaller neck entrances from the sample surface; e.g., Kaufmann, 2010) and pore accessibility issues (e.g., Hunt et al., 2014) cause it to underestimate the volume of large pores and overestimate that of small pores. MICP results are also affected by the size of the sample, and this provides us with an opportunity of examining the pore accessibility of different-sized samples.

The potential damage to the sample caused by MICP analyses probably depends on the sample's mechanical properties. There is a body of literature studying high pressure effects on pore structure change, though most of this research focuses on cement paste and concrete samples. Predominant findings are that the pore structure change is not evident (e.g., Shi and Winslow, 1985; With and Glass, 1997; Penumadu and Dean, 2000; Lawrence, 2006). For example, Penumadu and Dean (2000) evaluated the compressibility effect on pore-size distribution of kaolin clay using mercury intrusion porosimetry. They found that the edges of individual kaolin platelets showed no evidence of breakage, even after these samples were subjected to very high pressures of 210 MPa (2,100 bars).

The limitation of 3 nm pore-throat intrusion by MICP analyses is overcome by the gas sorption isotherm approach. Gas sorption isotherms are an established approach to studying the pore-size distribution of mesoporous (2–50 nm) and macroporous (>50 nm) materials (Gregg and Sing, 1982). Detailed pore-size distributions can be estimated from the sorption isotherms using various theoretical methods, each of which requires assuming an idealized pore shape (Barrett et al., 1951; Gregg and Sing, 1982). In collaboration with Dr. Shoichiro Hamamoto of Saitama University (Japan), we used the Tristar® II 3020 (Micromeritics; Figure 3) to measure pore-size distributions of Barnett shale. A dried sample weighing approximately 0.5 g is placed into the sample cell with a tube inner diameter ~5 mm. The sample cell is installed onto the sample degassing apparatus, and evacuated at 110°C for 72 hours. A tank of liquid nitrogen, at a temperature of -195.8°C (77.2 K, or -320.44 °F), is placed around the sample tube for the isotherm test. The nitrogen gas is dosed to the sample, and allowed to adsorb onto the sample. The quantity adsorbed under different relative pressures of nitrogen is recoded, giving gas adsorption isotherms. Brunauer, Emmett and Teller (BET) theory provides a mathematical model for the process of gas sorption, and the surface area is obtained from the gas adsorption isotherms according to the BET equation (Brunauer et al., 1938). Pore-size distribution is calculated by the BJH model (Barrett et al., 1953).

Figure 3. A nitrogen sorption isotherm apparatus, the Micromeritics Tristar® II 3020.

The medium-priced TriStar II system is limited to pores in the size range 2–300 nm, and sample dimensions <~4 mm. This low detection limit (2 nm) probably misses a sizeable portion of nanopores in tight shales. Quantachrome (Boynton Beach, FL) has a new gas sorption analyzer, the Autosorbi Q–Micropore–XR, which can measure pore sizes from 0.35 to 500 nm, with sample dimension up to 10 mm. This system has an extremely low pressure sensor (0.1torr) for detailed micropore (defined as <2 nm by IUPAC) size measurements, ideal for shale samples. Micropores are determined by NLDFT theory (Non-local Density Functional Theory), proposed by Neimark and co-workers (Neimark et al., 1998; Neimark and Ravikovihtc, 2001). One shale sample was test-measured by the Quantachrome Instrument.

Nitrogen sorption isotherms give narrower pore–size ranges than those from the MICP method, with the upper limit (about several hundreds of nanometers) of pore-size determination related to the pressure sensor capabilities. However, nitrogen sorption does not, at least in adsorption curve, suffer from the ink-bottle effects as the nitrogen will sorb and condensate on the small pores first. Throat (also called neck) pores influence the desorption branch and lead to hysteresis effects (e.g., Seaton, 1991).Hysteresis in both the N_2 sorption and MICP methods contains some information about pore accessibility, but the wetting (sorption) and drying (desorption) loops from both methods together are richer in information about pore accessibility and structure than either alone.

In addition to MICP tests, bulk density, porosity, and particle density was determined by the vacuum saturation method (e.g., Hu et al., 2012). The procedure consists of (1) drying samples at a temperature of 60±2°C, (2) saturating the samples with degassed and de-ionized water under 99.91% vacuum, as indicated by a 275 Series Digital Convectron Gauge (Granville–Phillips; Figure 4), (3) determining the bulk volume of irregularly-shaped samples using Archimedes' water immersion technique (Vennard and Street, 1975), (4) calculating the bulk density and porosity, and (5) using the values of sample dry weight, bulk volume, and porosity to calculate the particle density. Samples are initially dried to a constant weight at a temperature of 60±2 °C, in order to preserve bound water on clays and to ensure that the water removed by drying is derived solely from pore water.

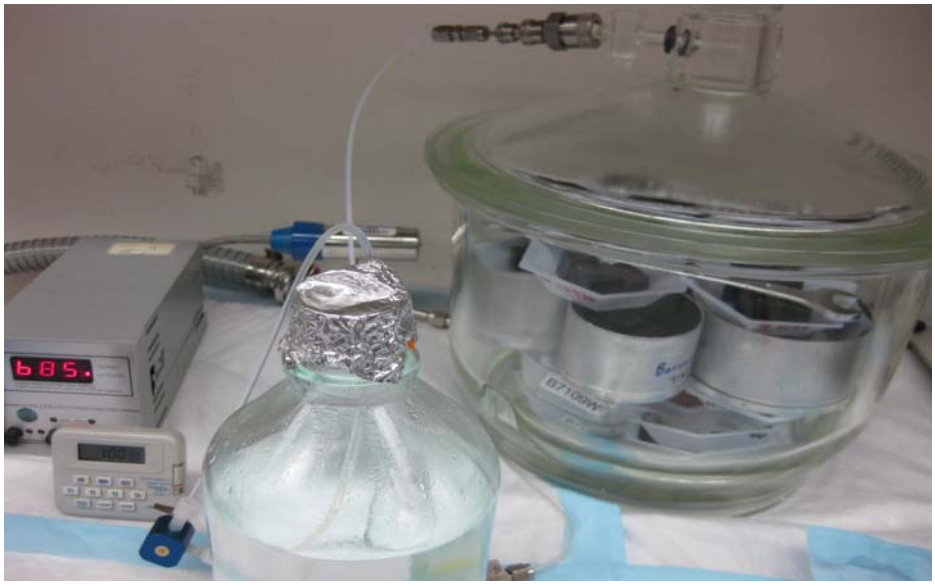

Figure 4. An apparatus for vacuum saturation.

Results and Discussion

Figure 5 shows triplicate measurements of pore-throat distribution of MICP results of Barnett shale samples, indicating good reproducibility. Figure 6 presents the comparison of pore-throat distributions of Barnett shale samples at different depths (separated by at most 100 ft). Note that (1) the sample from a depth of 7,136 ft exhibits different behavior from the other depths; this sample, from the Forestburg limestone member of the Barnett shale, has lower porosity (Table 2);

and (2) the Y-axis of "Cumulative Intrusion Volume" for Figures 5–6 is arbitrarily set to 100% for the minimum measureable pore-throat of 3 nm, dictated by the maximum intrusion pressure of the MICP instrument; there maybe some non-negligible pore volume accessible only through pore-throats <3 nm, quantifiable by nitrogen sorption approach with its theoretical measurement limit of 0.35 nm (the size of the probing nitrogen molecule). However, the volume of pores accessible via pore-throats <3 nm is not expected to be large, or to play an important role in fluid migration.

The MICP results show that most pores (about 60–80% by volume) in four Barnett shales (all but the 7,136 ft sample, the Forestburg limestone) are smaller than 100 nm. These results are consistent with observed pore sizes from field emission-SEM, with the detection limit of 5 nm, by Loucks et al. (2009), who reported that Barnett shales have intraparticle organic nanopores ranging from 5 and 750 nm, with the median nanopore size being 5–15 nm.

Table 2: MICP results for Barnett shale samples

Depth (replicates)	Porosity (%)	Bulk density (g/cm^3)	Apparent density (g/cm^3)	Median pore-throat diameter (nm)	Permeability (nanodarcy)	Tortuosity
7,109 ft (2,167 m)	4.32	2.47	2.58	6.2	3.68	
7,136 ft (2,175 m) (N=3)	0.52±0.46	2.63±0.003	2.65±0.01	22.4±10.7	1.86±1.20	95.2±92.0
7,169 ft (2,185 m)	2.88	2.56	2.64	8.9	2.21	167
7,199 ft (2,194 m) (N=4)	5.97±1.43	2.37±0.04	2.49±0.02	9.1±6.1	4.96±1.42	97.2±67.2
7,219 ft (2,200 m) (N=5)	3.26±0.55	2.45±0.03	2.55±0.03	7.1±0.8	2.48±0.40	92.1±64.8

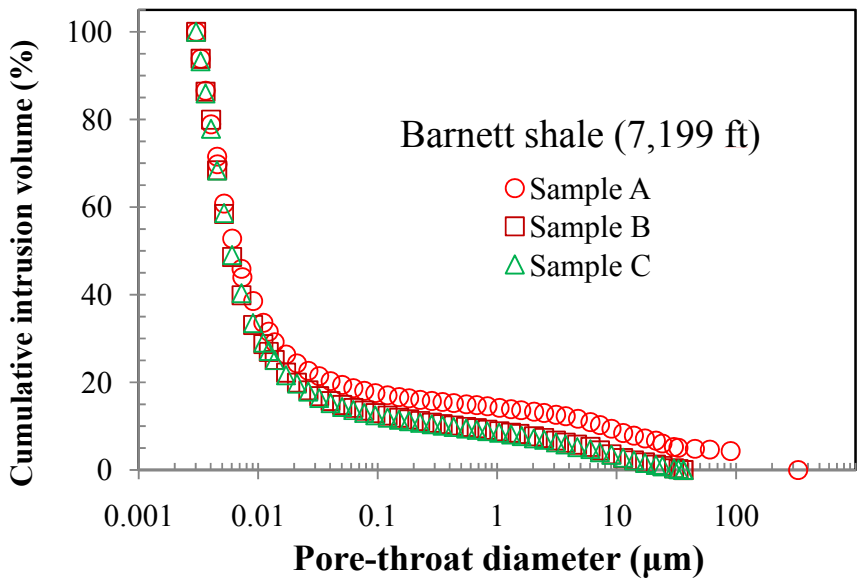

Figure 5. Triplicate MICP measurements of a Barnett shale sample for pore-throat distribution.

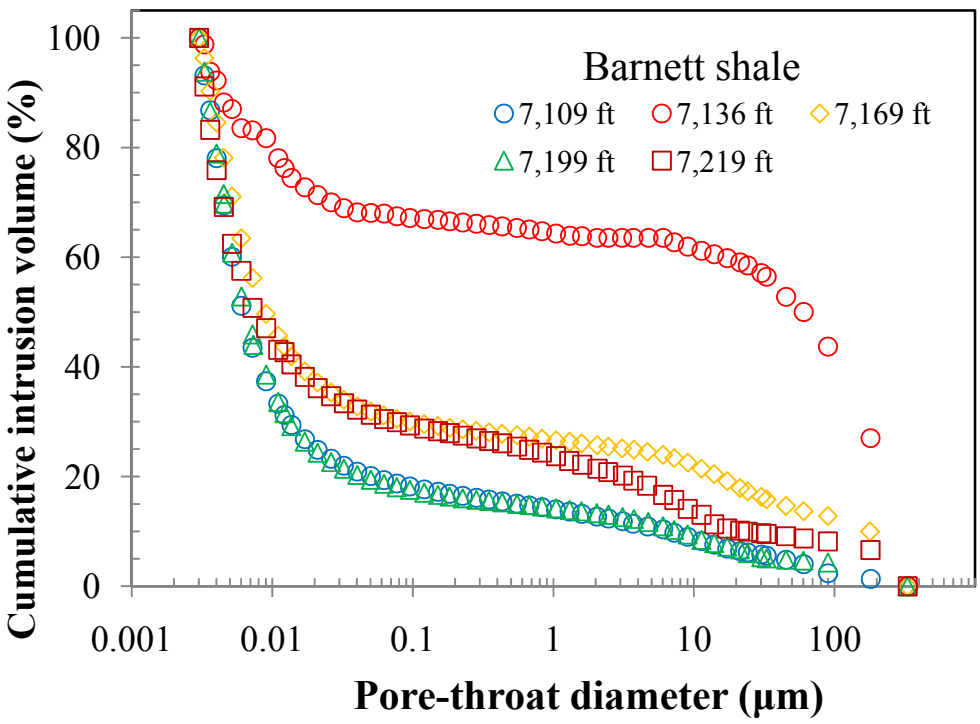

Figure 6. MICP pore-throat distribution measurements on Barnett shale samples.

As shown in Figure 7, Barnett shales possess some pores smaller than 3 nm (0.003 µm), measurable by nitrogen sorption method. Different pore-size interpretation approaches can yield somewhat different results. The NLDFT (Non-local Density Functional Theory) model, able to describe the behavior of fluids that are confined in small pores, is currently the accepted approach for micropore (<2 nm) determination. As a comparison, classical and semi-empirical methods (e.g., BJH) assume that the density of the adsorbed phase remains constant, regardless of the size of the pores that it occupies.

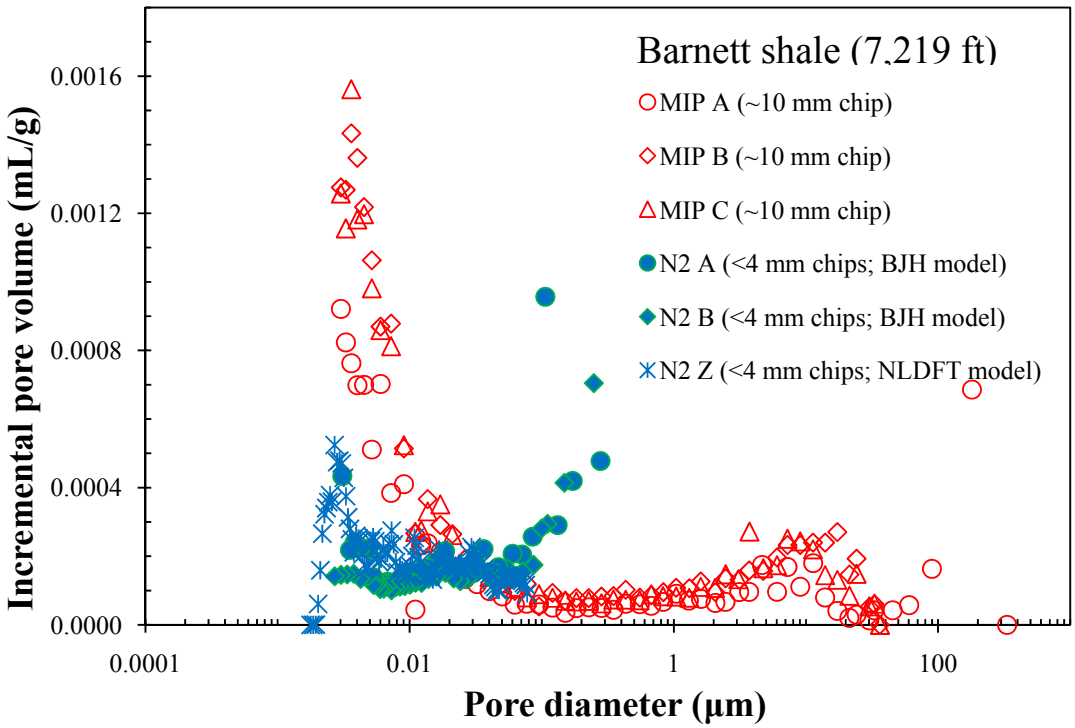

Figure 7. Comparison of pore-size distribution measurements by MICP and nitrogen sorption methods. N_2 A and B were analyzed at Saitama University, while N_2 Z was measured by the Quantachrome Instrument.

Shown at Table 3, the average pore-size measured by the nitrogen sorption isotherm approach is from 3.2 to 8.3 nm for <4 mm chip samples, and about 15 nm for <75 µm powder mixture. Though the difference of average pore-size at two size fractions seems to be small, the

reasons for this observation are unknown. The BET surface area of our four Barnett samples at different depths ranges from 7.9 to 15.8 m^2/g, which is consistent with Clarkson et al.'s (2013) measurement of a 14 m^2/g BET surface area for a Barnett sample.

As measured by MICP, pores in Barnett shale are predominantly in the nm size range with a measured median pore-throat diameter of 6.5 nm, and estimated permeability is 2–5 nD (Table 2). This is consistent with the literature values of Barnett shale matrix pore size of about 5 nm (Bowker, 2007), and permeabilities of 70–5,000 nD by (Grieser et al., 2008), 10–600 nD by Sigal and Qin (2008), and 1–10 nD by pulse-decay permeameter with helium on 1–2 mm sized Barnett chips (Heller and Zoback, 2013). The reported permeability of 20 "black shales" by the GRI (crushed-rock) method for shale permeability measurement ranges in magnitude between 1 and 1,000 nD (Luffel et al., 1993; Guidry et al., 1996); shortcomings of the GRI or crushed-rock technique to measure permeability of shales are discussed by Sinha et al. (2012). Unfortunately, as indicated by Sigal and Qin (2008), most rock property measurements on shale gas reservoir rocks are confidential, as are many of the details of how the measurements were performed.

Table 3: Barnett shale sample properties measured by nitrogen sorption isotherm

Sample ID	BET surface area (m^2/g)	Average pore size (nm)
Barnett shale powder mixture† (7,105–7,164 ft)	8.84±0.077	15.6±0.13
Barnett shale powder mixture (7,164–7,224 ft)	10.2±0.16	14.6±0.12
Barnett shale 7,109 ft	13.4±0.28	6.12±0.23
Barnett shale 7,136 ft	4.94±0.52	7.12±0.042
Barnett shale 7,169 ft	9.77±0.34	8.27±1.31
Barnett shale 7,199 ft	15.8	3.16
Barnett shale 7,219 ft	7.93±0.22	5.51±1.41

† The powder mixture has the sample size <75 µm, and all other samples are less than 4 mm chips.

Using Hager's (1998) analysis, tortuosity is on the order of 100; the definition and discussion of tortuosity will be presented in Tasks 5–6. Note that the standard deviation for the

MICP-derived tortuosity is fairly large. The tortuosity calculation requires the identification of a threshold pressure, the pressure at the inflection point of the cumulative intrusion curve (Webb, 2001); only data points after the threshold pressure are used for calculating tortuosity. In the Barnett shale there are only about 5 data points after the threshold pressure, which is why the estimated tortuosities have large standard deviations. For comparison, in Task 6, tortuosity values for about 15 mm-sized Barnett shale samples, similar to these used in MICP tests, were measured by a saturated diffusion approach.

The MICP and vacuum saturation approaches give similar values for porosity, bulk density and particle density, despite having very different measurement principles. While porosity values for samples 7,136 and 7,169 ft are close between the two methods, MICP gives slightly higher porosity values for the other three samples. This indicates that the high pressure of MICP method can likely invade some edge-connected pores that are not easily accessible by vacuum-pulling approaches, which is not surprising. A more air-tight apparatus capable of reaching lower vacuum, and longer vacuum duration, may be required to evacuate the air present in the poorly-connected pore spaces in shale.

Task 2: Imbibition Tests

Objectives

Spontaneous imbibition is a capillary-force driven process during which a wetting fluid displaces a non-wetting fluid under the influence of capillary suction only. In the process of oil/gas recovery from fractured reservoirs, water is spontaneously imbibed from the fracture system into the rock matrix blocks, with the result that oil and gas in the matrix are displaced by the water. As a result, the oil/gas production rate is strongly dependent on the spontaneous imbibition process, and extensive research has been undertaken to investigate this process in oil and gas industry (Li, 2007; Standnes, 2010; Graue and Fernø, 2011; Shahri et al., 2012).

Because of the mathematical analogy between diffusion and imbibition, liquid imbibition can be used to probe a rock's pore connectivity (Hu et al., 2012). Imbibition tests, which are much faster than diffusion tests, involve exposing one face of a rock sample to liquid (for example, water or *n*-decane), and monitoring the mass uptake over time (e.g., Hu et al., 2001; Schembre

and Kovscek, 2006). Using the network modeling results of Ewing and Horton (2002), we can probe pore connectivity, as indicated by the slope of log imbibed liquid mass versus log time. The imbibition behavior – slope of ¼, ¼ changing to ½, or ½ – roughly classifies a rock's pore connectivity (Hu et al., 2012). Specifically, for a sample with pore connectivity just above the percolation threshold, solute diffusion (analogous to liquid imbibition) is anomalous at short diffusion/imbibition times and distances, but later transitions to "classical" (Fickian) long-term behavior. The distance to the diffusion/wetting front at this transition is the crossover (or correlation) length χ of percolation theory (Stauffer and Aharony, 1994; Hunt et al., 2014).

Methods

For the imbibition experiments, all the samples were cut into rectangular prisms at about 15 mm. All sides except the top and bottom were coated with quick-cure transparent epoxy to avoid evaporation of the imbibing fluid from (and avoid vapor transport and capillary condensation through) the side surfaces of the samples, and the use of modest-viscosity epoxy also allows imbibition up the external surface for us to study 2-D tracer migration along the side, in addition to 3-D migration in the sample interior (see results in Task 6). The imbibition apparatus is shown in Figure 8; the experimental procedure and data processing were described in detail by Hu et al. (2001). Samples first were oven-dried at 60 °C for at least 48 hours before being subjected to the imbibition experiments, in order to achieve a constant initial water saturation state. During the water imbibition experiments, beakers of water were placed inside the experiment chamber to keep the humidity inside the chamber constant. The top of the side-epoxied samples was loosely covered with foil, with a small hole left for air escape, to reduce vapor transport and capillary condensation on to the top face. The sample bottom was submerged to a depth of about 1 mm in a fluid reservoir. The imbibition rate was monitored by automatically recording the sample weight change over time.

Figure 8. The apparatus for a fluid imbibition test.

Imbibition tests are conducted on samples of different height:width ratios (i.e., shape). The crossover length χ is related to both sample shape and pore connectivity. A material with low pore connectivity has a large crossover length, so if the sample height is greater than the crossover length, a sample with diameter equal to its height would be unlikely to have an infinite cluster to percolate (Stauffer and Aharony, 1994). But a sample with width much greater than its height would likely percolate (have an infinite cluster), so varying the height:width ratio provides an additional way to estimate the crossover length.

Because of the layered nature of Barnett shale, we carried out imbibition experiments in two orthogonal directions, both parallel and transverse to the bedding plane, to study anisotropic effects on imbibition. This required epoxying samples differently.

Results and Discussion

Imbibition experiments for Barnett shales consistently produce imbibition slopes of approximately ¼ (Figure 9; Table 4), indicating the low pore connectivity of these shales (Hu et al., 2012).

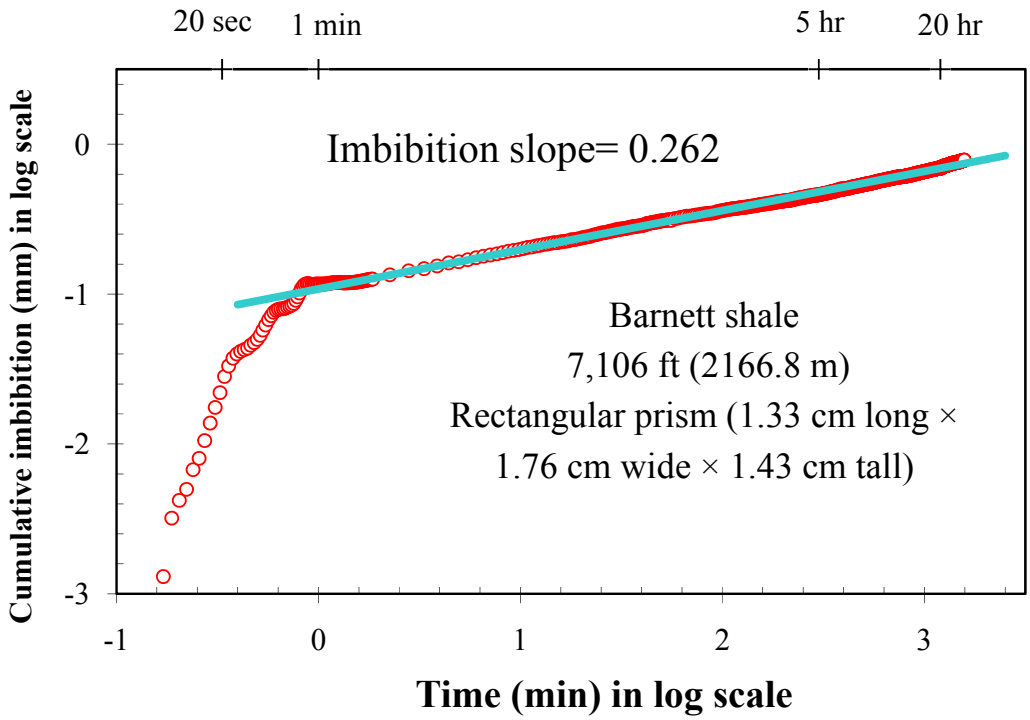

Figure 9. Water imbibition results for a typical Barnett shale sample.

The ¼ slope was consistent across different sample shapes and imbibition directions (parallel/horizontal versus transverse/vertical to the bedding plane), and for all five Barnett shale sample depths (Table 4). From this we conclude that pores in the Barnett shale are poorly connected, with a correlation length (imbibition distance at which behavior becomes Fickian) greater than the sample length (approximately 15 mm). As a comparison, Hu et al. (2012) experimentally observed all three types of imbibition slopes (¼, ¼ changing to ½, and ½), consistent with percolation theory (Hunt et al., 2014). For example, Hu et al. (2012) observed the ½ slope across all sample shapes for Berea sandstone samples, indicating its well-connected pore spaces.

Table 4: Water imbibition slopes for Barnett shale samples

Depth	Sample dimension	Height / width	Imbibition slope (N=3)†
7,109 ft (2,167 m)	1.33 cm L×1.76 cm W ×1.43 cm H (Vertical)	0.93	0.214 ±0.059
	1.76 cm L×1.72 cm W ×1.32 cm H (Horizontal)	0.76	0.291 ±0.027
7,136 ft (2,175 m)	1.38 cm L×1.71 cm W ×1.72 cm H (Vertical)	1.12	0.269 ±0.0045
	1.73 cm L×1.73 cm W ×1.21 cm H (Horizontal)	0.70	0.216 ±0.040
7,169 ft (2,185 m)	1.35 cm L×1.79 cm W ×1.81 cm H (Vertical)	1.16	0.273 ±0.050
	1.24 cm L×1.78 cm W ×1.32 cm H (Horizontal)	0.87	0.357 ±0.006
7,199 ft (2,194 m)	1.24 cm L×1.74 cm W ×1.67 cm H (Vertical)	1.12	0.284 ±0.062
	1.74 cm L×1.72 cm W × 1.26 cm H (Horizontal)	0.67	0.282 ±0.047
7,219 ft (2,200 m)	1.37 cm L×1.74 cm W × 1.95 cm H (Vertical)	1.25	0.306 ±0.019
	1.69 cm L×1.71 cm W ×1.36 cm H (Horizontal)	0.80	0.264 ±0.046

†Average ± standard deviation for replicate measurements on the same sample.

Task 3: Edge-Only Accessible Porosity Distribution

Objectives

In a rock with sparsely-connected pores, the accessible porosity decreases with distance from an edge (e.g., a fracture). In this Task, we measure the decrease in accessible porosity with distance from an exposed face in order to assess pore connectivity in the shale samples. Samples are dried, subjected to vacuum, and wetted with a solution containing both non-sorbing and sorbing tracers. These tracers will occupy the evacuated connected pore spaces, and mapped

using micro-scale Laser Ablation–ICP–MS (LA–ICP–MS; laser ablation–inductively coupled plasma–mass spectrometry; Figure 10). Laser energy vaporizes a hole into the rock sample at the micron scale, and the vaporized sample is analyzed by ICP–MS. In this way, tracer concentration profiles – related to accessible porosity – can be measured directly, rapidly, and with high sensitivity. The LA–ICP–MS method gives both (1) the rate of decrease in concentration from the edge to some plateau (constant) concentration, and (2) the depth at which the plateau concentration is reached; both are related to the pore connectivity of the shale.

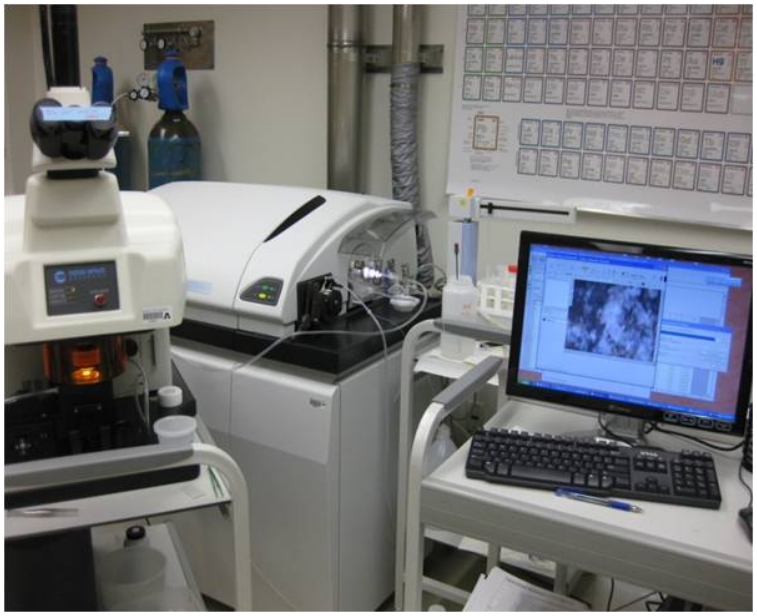

Figure 10. The LA–ICP–MS apparatus for micro-scale elemental mapping.

Methods

Tracer solution containing both non-sorbing (bromide and perrhenate [ReO_4^-]) and sorbing (cobalt, strontium, cesium, and samarium, with different sorption extent) tracers was prepared using ultrapure (Type 1) water and >99% pure reagents ($CoBr_2$, CsBr, CsI, NaBr, $NaReO_4$, $SmBr_3 \cdot 6H_2O$, $SrBr_2 \cdot 2H_2O$; Sigma–Aldrich Co., St. Louis, MO). Concentrations used were 400 mg/L $CoBr_2$, 100 mg/L CsI, 4,000 mg/L NaBr, 100 mg/L $NaReO_4$, 200 mg/L $SmBr_3$, and 400 mg/L $SrBr_2$. This tracer solution was sparged with helium for half an hour to remove dissolved air before usage.

Dry samples at a temperature of 60±2 °C were put under vacuum for one hour to reach a vacuum level of 0.68 torr (99.91% vacuum) as indicated by a 275 Series Digital Convectron Gauge (Granville–Phillips), to remove air from the edge-accessible pore spaces. Then the tracer solution was introduced into the sample chamber, fully submerging the samples, to allow full tracer access to the evacuated edge-accessible pores. Then the chamber was opened to the atmosphere for two days to allow the tracer solution to further invade the pore spaces under atmospheric pressure. The shale samples were then removed from the reservoir, frozen with liquid nitrogen, freeze-dried at -60 °C and near-vacuum (about 1 Pa) for a day, and stored at low relative humidity below 10% prior to LA–ICP–MS analyses.

The laser ablation system (New Wave; Freemont, CA) used a 100 µm spot diameter UP-213 laser to vaporize a hole in the shale sample at sub-micron depth increments; elements entrained in the vapor were analyzed with ICP–MS (PerkinElmer/SCIEX ELAN DRC II; Sheldon, CT). This LA–ICP–MS approach can generate 2-D and 3-D maps of chemical distributions in rock at a spatial resolution of microns, and a concentration limit of low-mg/kg (Hu et al., 2002; Peng et al., 2012b; Hu and Mao, 2013). In this Task, a 2 mm × 2 mm grid of spots mapping routine was performed, with 100 µm laser spot size and 200 µm spacing between spots, resulting in a total of 121 spots for this grid size. For 3-D mapping, a total of 4 layers were ablated at the same spots, at the laser pulse numbers of 5, 20, 80, and 320, which (based on our measured depth/pulse relationship) corresponds to depths of about 2, 12, 54, and 224 µm.

Results and Discussion

Figure 11 shows the 3-D mapping results of the non-sorbing perrhenate tracer (ReO_4^-), which is indicative of the edge-accessible porosity distribution of Barnett shale. Non-sorbing tracer will only occupy the pore spaces and does not interact with the shale matrix. The dramatic decrease of tracers with depth illustrates the poorly-connected pore spaces of Barnett shale. Within a distance of only 224 µm, the concentration of perrhenate dropped from 57.2±15.8 mg/kg (N=121) at the surface to 0.96±0.45 mg/kg (N=121) at layer No. 4, a factor of 60.

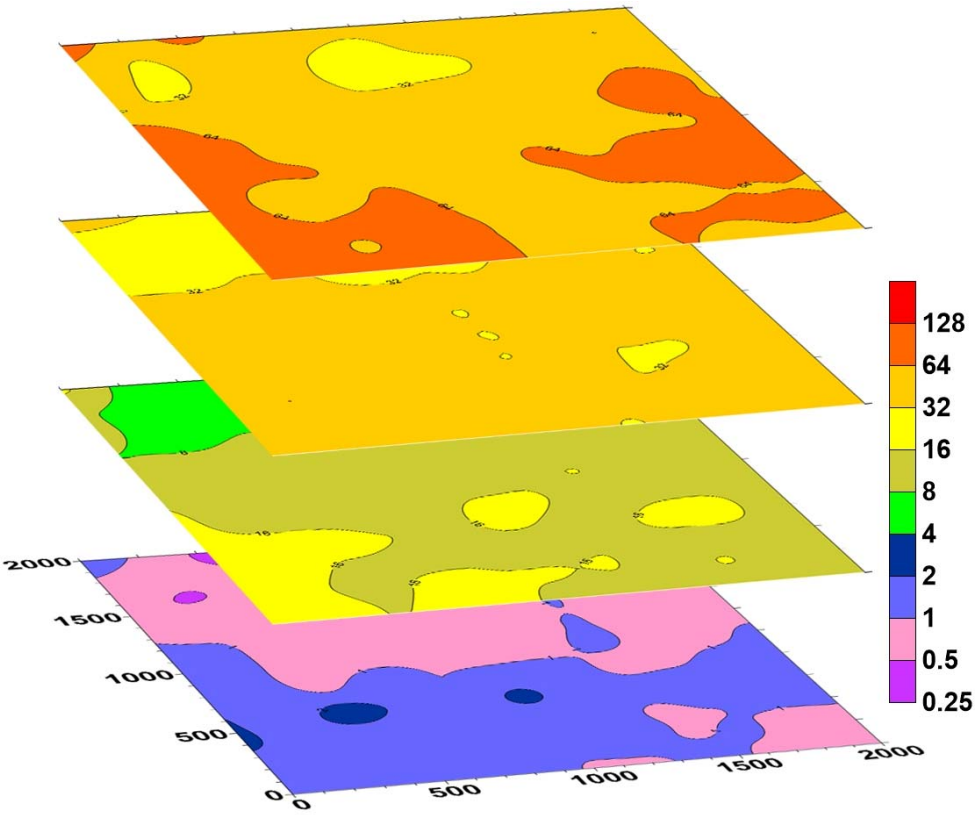

Figure 11. 3-D mapping results of non-sorbing perrhenate (ReO_4^-; mg/kg in the scale bar) by LA–ICP–MS for Barnett shale 7,136 ft (Forestburg limestone) sample; top to bottom layers are sampled at 2, 12, 54, and 224 µm from sample surface, respectively. This 2,000 µm × 2,000 µm grid was selected in the middle of a face of 15 mm-sided cube, and mapped with a 100 µm laser spot size and 200 µm spacing between spots.

Figure 12 presents tracer concentration vs. depth, with concentrations given as the average of all 121 spots in a single layer, along with the line showing the exponent (slope in log space) expected from percolation theory. The exponent β indicates the fraction of the total porosity that is connected to the infinite cluster, while the exponent ν adjusts it for spatial scaling (Ewing et al., 2012; Hunt et al., 2014). It can be seen that the experimental data are consistent with the theory of edge-accessible porosity distribution related to pore connectivity. The steep decline of edge-accessible porosity, over a distance of only about 100 µm from the sample edge, indicates poor pore connectivity for Barnett shale.

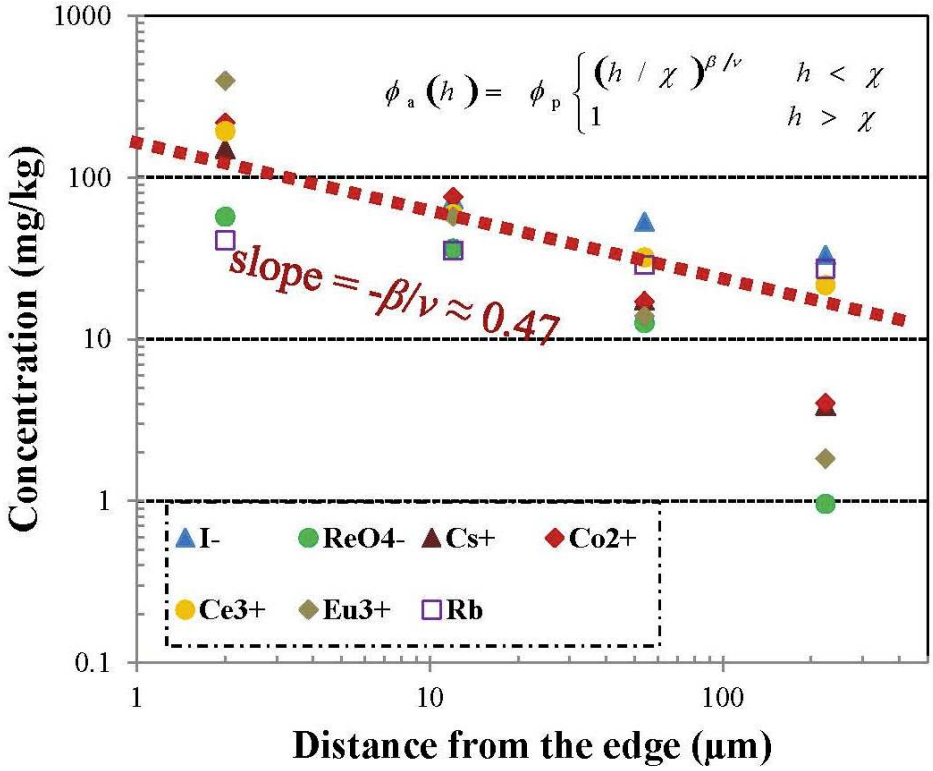

Figure 12. Average concentrations of tracers vs. depth for Barnett shale 7,136 ft (Forestburg limestone); the dashed line indicates the slope expected from percolation theory.

We used a low-speed diamond saw (Buehler IsoMet) to dry-cut the sample to expose the sample interior to conduct 2-D elemental mapping with LC–ICP–MS. Using a laser spot size of 100 µm, we can map a larger interior area to complement sub-micron spatial resolution from the 3-D mapping shown in Figure 11. The 2-D mapping results for non-sorbing ReO_4^- are shown in Figure 13. The data points along the left side (near the Y–axis) are centered at 75 µm from the sample edge, which is between layer 3 and layer 4 of Figure 11; the measured concentration is consistent at about 5 mg/kg. Note that the length for this cube-sized sample is 15 mm (15,000 µm), and the mapped grid did not extend to the other edge of the sample (Figure 14). By a distance of 1,000 µm from the sample edge, the perrhenate concentration has dropped by more than a factor of 100 and remains fairly constant through the rest of the sample, except for higher concentrations (green and yellow) around 5 mm, probably from preferential pathways from the top or bottom. The background level of Re in Barnett shale is about 0.1 mg/kg.

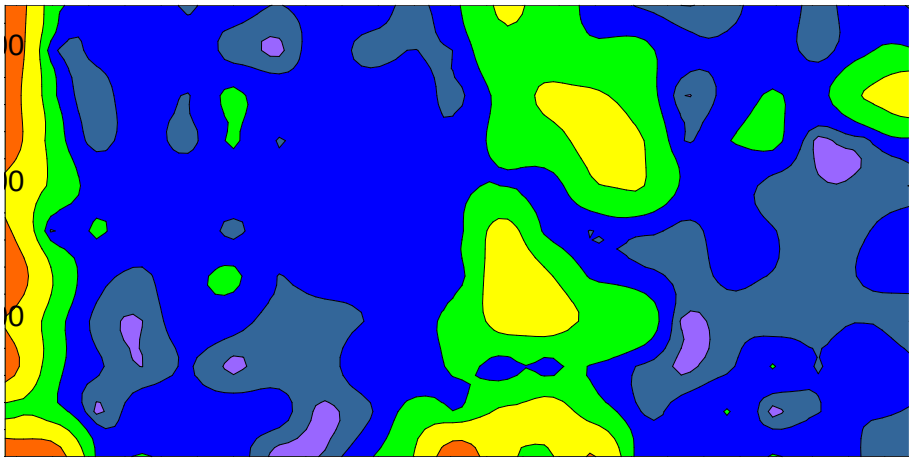

Figure 13. 2-D mapping by LA–ICP–MS of non-sorbing perrhenate distribution from in a Barnett shale sample from 7,136 ft (Forestburg limestone). Laser spot size is 100 µm; spacing between spots is 500 µm; X and Y distances are in µm.

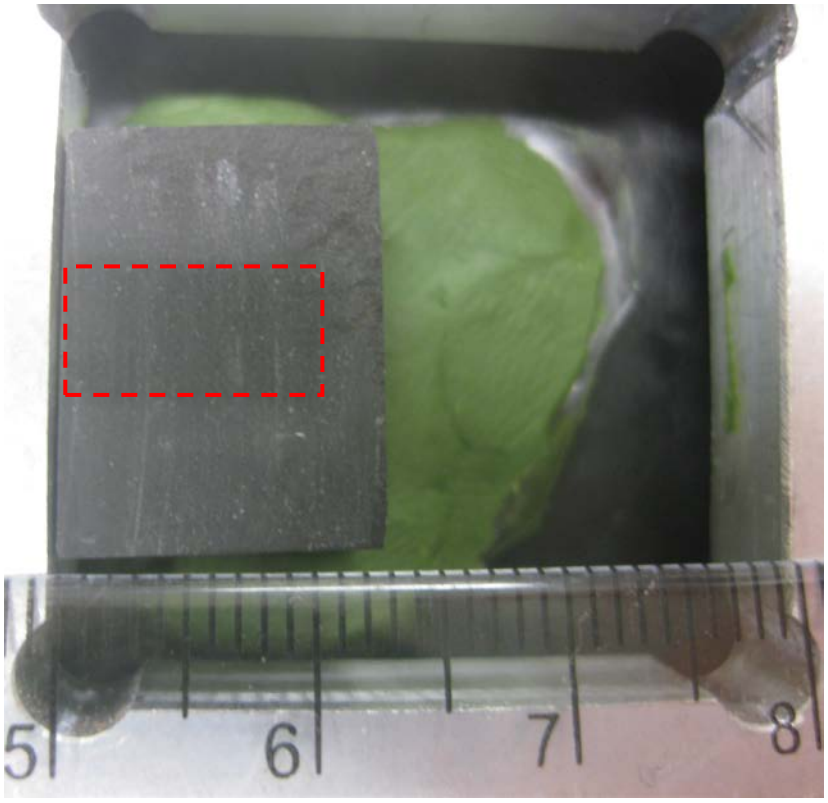

Figure 14. Mapped area of 10 mm × 5 mm for Figure 13 in a Barnett shale sample from 7,136 ft (Forestburg limestone).

Task 4: Pore Structure Imaging using Wood's Metal Alloy Intrusion

Objectives

In contrast to the porosimetry, isotherm, imbibition, and edge-accessible porosity methods described above, the Wood's metal intrusion and consequent SEM imaging and LA–ICP–MS provides direct connection of surface-accessible pore structure. Rock pore networks can be examined by injecting the rock with molten Wood's metal alloy (50% Bi, 26.7% Pb, 13.3% Sn, and 10% Cd; melting point around 78 °C), a method pioneered by Swanson (1979) and Dullien (1981). Because of its high bismuth (Bi) content, Wood's metal alloy does not shrink as it solidifies (Hildenbrand and Urai, 2003). Because this metal alloy is solid below 78 °C, pore structures filled by Wood's metal can be readily imaged and mapped for the presence of alloy component elements. Injecting molten Wood's metal alloy also offers the possibility of "freezing" the invaded network at any stage of the injection, allowing micro-structural studies to be made on the iteratively-filled pore networks (Kaufmann, 2010). Dultz et al. (2006) explored injecting Wood's metal alloy into feldspars to determine their porosity and pore connectivity.

Methods

We collaborated with Dultz to examine pore connectivity of a range of rock samples (Hu et al., 2012). Following the method of Dultz et al. (2006), dried cylindrical samples (maximum size 5 mm dia., 15 mm length) were submerged in Wood`s metal alloy in a 100 °C autoclave. The autoclave was evacuated to <0.001 bar. Then the molten alloy was forced into the accessible pores by applying an argon pressure of ~600 bar, invading pores with equivalent diameters >20 nm. The estimation of the diameter is based on a surface tension of 0.4 N/m and a contact angle of 130° (Darot and Reuschle, 1999), according to Equation 1 (Washburn, 1921). After the molten alloy solidified, 150 µm thick sections were prepared and imaged with an environmental SEM (Quanta 200, FEI, Hillsboro, OR) with back-scattered electrons.

However, invasion of pores down to 20 nm is not sufficient for the predominantly nano-sized pore spaces in shales. We therefore established collaboration with Dr. Josef Kaufmann at Empa (Switzerland), whose lab can inject Wood's metal alloy at pressures up to 6,000 bars, which corresponds to a pore diameter of only 2.35 nm. In this project, shale samples were shipped to Dr.

Kaufmann for high-pressure Wood's metal alloy impregnation, then to Dr. Dultz's lab for sample polishing and 2-D cross-sectional SEM imaging. Finally, samples were returned to UTA for LA–ICP–MS analyses to map out elemental distribution of Wood's metal components in connected pore spaces. This collaborative approach used the unique capabilities of each lab for cutting-edge pore structure characterization of shale samples.

Shale samples (about 5×5×5 mm^3) were first dried at 110 °C for one week, then glued to the bottom of a cell, which was then filled with solid Wood's metal pieces. The cell was closed by a piston and heated to 85 °C under vacuum (<0.01 mbar); O-rings connecting the piston to the cell wall are able to bear pressures of more than 6,000 bars (Kaufmann, 2010). Once the metal was molten, a load was applied to the piston by means of a press in controlled load mode. Pressure in the cell was increased by 7 MPa/min until the maximum pressure was reached; the maximum pressure was then held for 15 min. After that, the temperature was decreased at a cooling rate of about 1 °C/min to solidify Wood's metal alloy in the intruded pore spaces. The load was regulated during the cooling (solidifying) stage to maintain the desired pressure level. Once cool, the alloy-impregnated sample was removed from the cell and cut horizontally, roughly in the middle of the sample height, to trace Wood's metal alloy intrusion from the sample sides. One cut piece was processed to 150 µm thick, polished and mounted on a glass slide, and imaged with SEM (Dultz et al., 2006). The other cut piece was used for LA–ICP–MS elemental mapping, using the elemental distribution of Wood's metal to identify connected pore spaces.

Results and Discussion

A test Eagle Ford shale sample was first processed at Dultz's laboratory at the University of Hannover (Figure 15). While matrix pores are not invaded at the pressure of 600 bars, a fracture about 5–10 µm across is observed. Image analysis gives a fracture porosity of 1.85%. Pyrite framboids, reported to be 2–6% for Barnett shales (Zhao et al., 2007), are clearly visible.

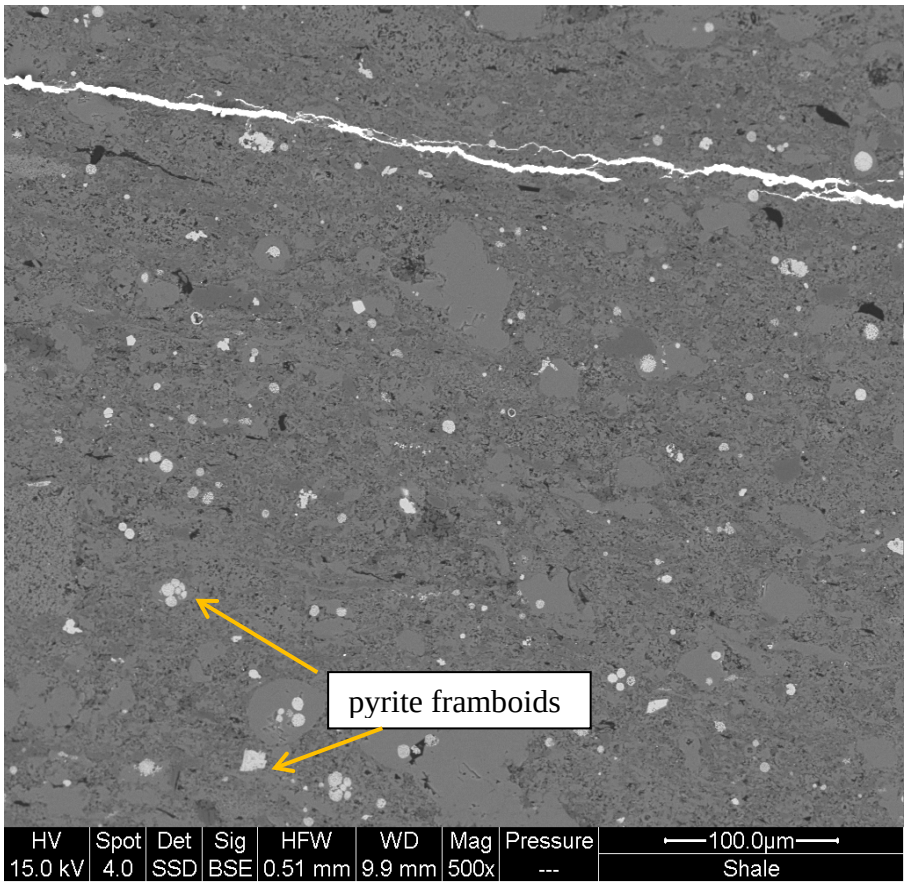

Figure 15. SEM-BSE images of connective pores occupied by the alloy Wood's metal (bright graytone) in an Eagle Ford test shale sample at 600 bars.

A Barnett shale sample from 7,169 ft was then impregnated with Wood's metal at Kaufmann's laboratory (Empa, Zurich, Switzerland), using the high-pressure intrusion system developed for concrete work (Kaufmann, 2010). Figure 16 shows the imaging results for Wood's metal injected at 1,542 bars, which corresponds to about 9.2 nm pore diameter to be invaded. It can be seen that the Barnett shale sample only has slight connected matrix porosity within about 60 µm (red arrow) from the sample's edge. In this sample, Wood's metal occupies small cracks and matrix pores connected to the sample surface (green arrow). As in the case for mercury intrusion, the sample is externally and uniformly surrounded by non-wetting molten Wood's metal alloy, with even pressurization to reduce experiment-related fractures.

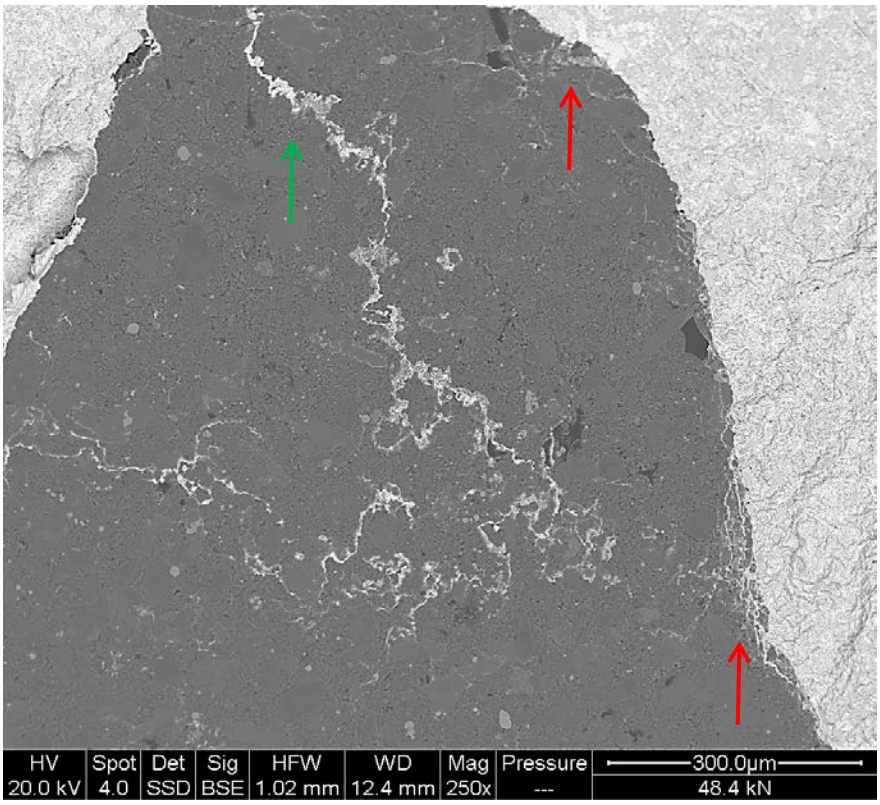

Figure 16. SEM-BSE images of connective pores occupied by the alloy Wood's metal (bright graytone) in Barnett shale sample of 7,169 ft at 1,542 bars.

Finally, samples from 7,136 ft (Forestburg limestone) and 7,219 ft (upper part of lower Barnett) were impregnated with Wood's metal at Kaufmann's laboratory at pressure of 4,000 and 6,000 bars, respectively corresponding to pore diameters of approximately 3.5 and 2.4 nm (Figures 17–18). From SEM imaging results, the 7,136 ft sample, which is a Forestburg limestone and has the lowest porosity among the 5 sample depths, does not show noticeable connected matrix porosity from the edge under either pressure (Figure 17). The shale sample from 7,219 ft (Figure 18) shows a crack, and also sporadic and very limited penetration of Wood's metal to about 60 µm from the sample edge.

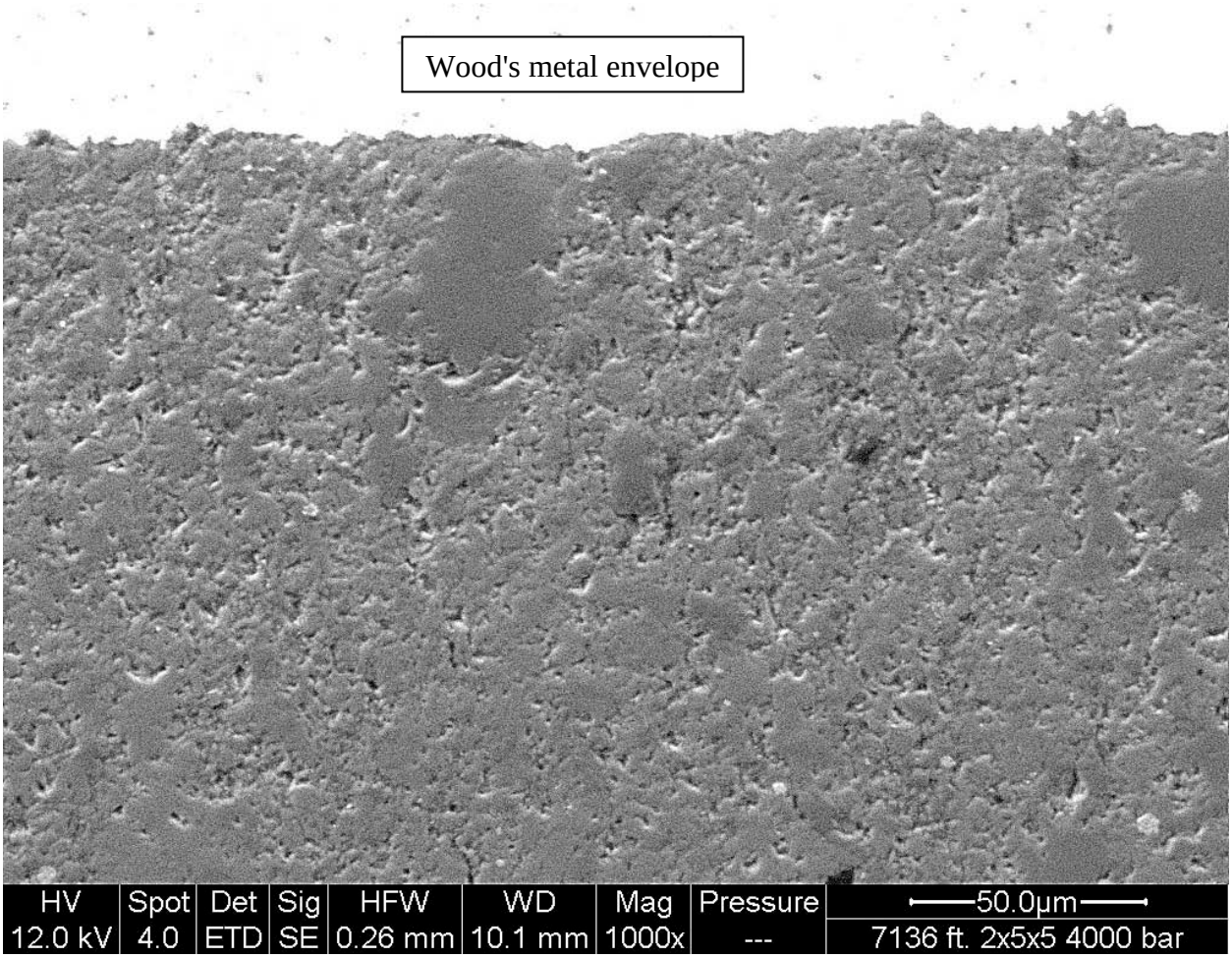

Figure 17. SEM-BSE images of Wood's metal impregnated Barnett shale sample from 7,136 ft (Forestburg limestone) at 4,000 bars.

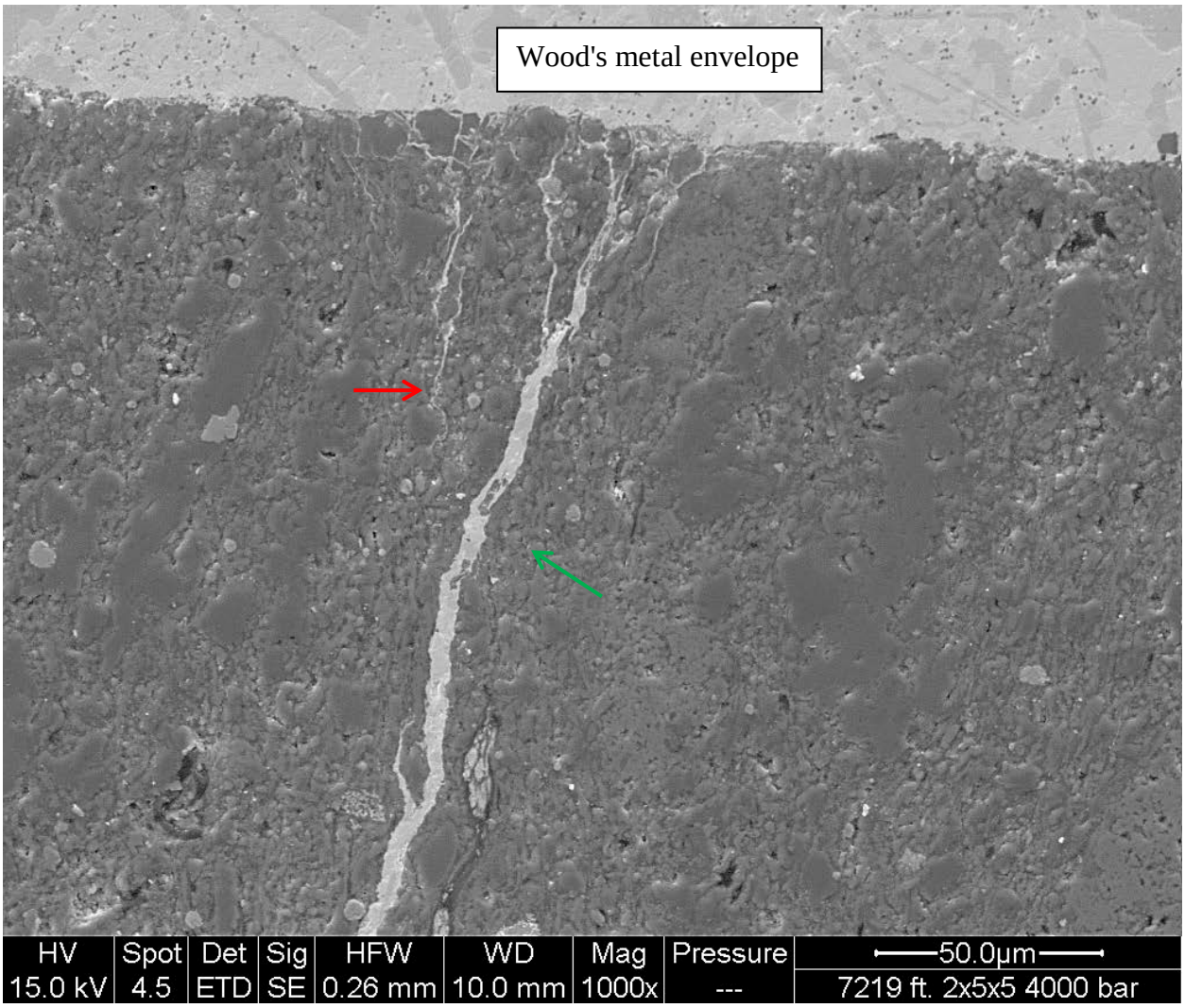

Figure 18. SEM-BSE images of Wood's metal impregnated Barnett shale sample from 7,219 ft (lower Barnett) at 6,000 bars.

Among our 5 Barnett sample depths, samples from 7,109 ft and 7,136 ft (upper Barnett and Forestburg limestone) do not have visible cracks, from the random microscope observation of prepared rectangular prism samples. The 7,169 ft sample seems to have short cracks, while the deepest samples, from 7,199 ft and (especially) 7,219 ft, have cracks, with widths of several µm, that transverse the sample domain (Figure 19). This is consistent with the Wood's metal imaging of observed crack in Barnett shale 7,219 ft (Figure 18).

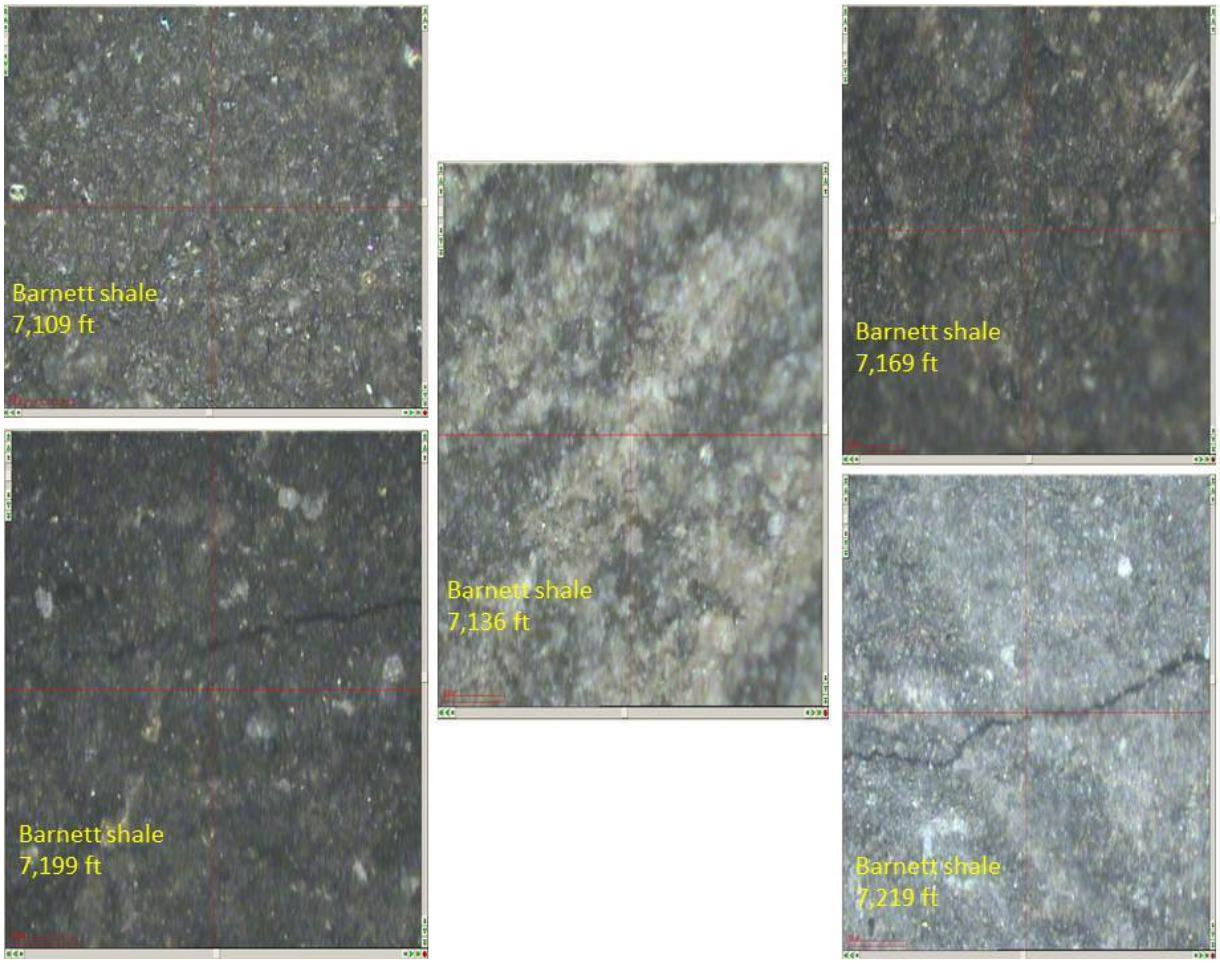

Figure 19. Microscope images of micro-cracks in Barnett shale samples.

The Barnett 7,136 ft shale sample (Forestburg limestone), impregnated with Wood's metal at 4,000 bars, was mapped by LA–ICP–MS for the presence of Wood's metal component elements (Bi, Cd, Pb, and Sn). Distribution of all these elements inside the shale sample was similar, so only the plot for Pb is presented (Figure 20). Wood's metal alloy has 26.7% Pb (267,000 mg/kg, consistent to the concentration detected by LA–ICP–MS), while it's natural abundance in the shale matrix is only about1 mg/kg, so Pb can be used as a proxy for Wood's metal. We see that, within about 5 mm, the Pb concentration decreases to only about 1/1,000th (about 1,000 mg/kg out of 267,000 mg/kg) of the concentration in the Wood's metal (Figure 20), even though the Wood's metal alloy did penetrate throughout the interior of this sample (2×5×5 mm^3). The observed penetration is not uniform near the sample edge: there is relatively gradual penetration

on the left side and top-left side of the sample, and much steeper decline on the right. LA–ICP–MS has higher chemical resolution, though lower spatial resolution than SEM (Figure 17), and reveals connected pore spaces that were not visible with SEM imaging (Figure 20).

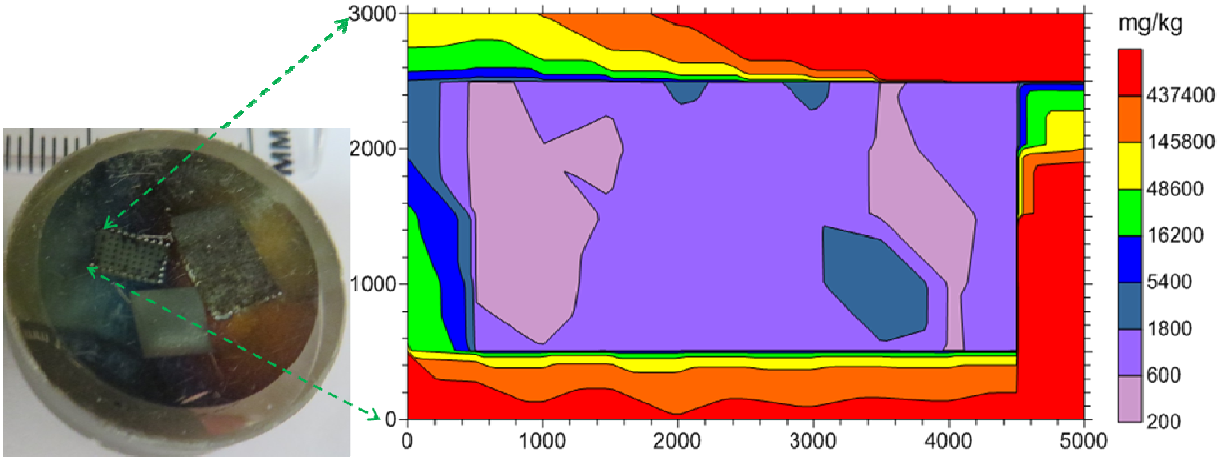

Figure 20. 2-D mapping by LA–ICP–MS of Pb (lead) distribution in a Barnett shale sample from 7,136 ft (Forestburg limestone). Wood's metal alloy is high in Pb, so Pb concentration identifies porous regions that are connected to the sample's exterior. Laser spot size is 100 µm; spacing between spots is 500 µm.

For the 7,219 ft sample with Wood's metal alloy injected under the higher pressure of 6,000 bars, LA–ICP–MS mapping used a tighter spacing of 175 µm between spots, better illustrating the sparse and heterogeneous presence of Pb (Figure 21). Two chains of higher Pb presence coincide with the cracks seen in the SEM image (Figure 18). Wood's metal alloy penetrates most pore spaces within the 5-mm sided cube sample. However, the surface-accessible connected pore space makes up a very low percentage of the shale matrix, with detected Pb concentrations in the range of 100 mg/kg, compared to 267,000 mg/kg of the Pb content in Wood's metal alloy itself. Connected porosity comprising about 1/1000th of the sample interior volume is consistent with other experimental approaches examining edge-accessible porosity (Task 3) and diffusion (Task 6), and our interpretation of pore connectivity based on percolation theory.

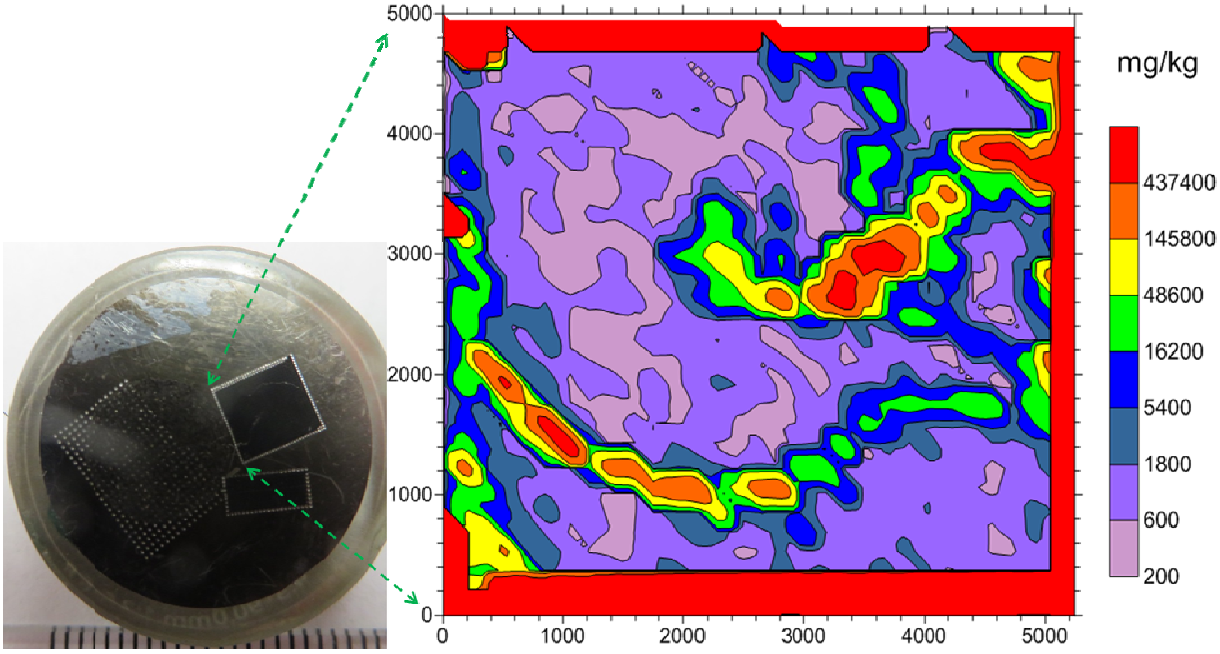

Figure 21. 2-D mapping by LA–ICP–MS of Pb (lead) distribution in a sample from 7,219 ft (lower Barnett) following Wood's metal alloy injection at 6,000 bars pressure. Laser spot size is 100 µm, and spacing between spots is 175 µm.

Task 5: Methane Sorption and Gas Diffusion in Crushed Shale

Objectives

Gas in shale source rocks is created by organic matter decomposition. It is then stored in two principal ways: (1) as free gas occupying pore spaces and fractures from diagenetic or tectonic processes, and (2) as gas adsorbed (chemical) and absorbed (physical) to or within the organic matrix (Jarvie et al., 2007). For the Barnett shale, Hill et al. (2007) reported 55% free gas and 45% sorbed gas; others put the sorbed gas closer to 20% (Curtis, 2002). Produced gas is mainly free gas stored in micropores at ambient reservoir pressures (1,000–3,000 psia, or 6.9–20.7 MPa). Gas desorbing from the organic matrix is believed to be a very small percentage of the produced gas during the early years of development (Zhao et al., 2007). Gases in the Barnett shale are typically about 90% methane (Jarvie et al., 2007). Characterization of the process of methane sorption and desorption is important to the understanding of methane transport and production in

shale formations. There are few studies on gas sorption behavior at reservoir pressure and temperature conditions (Zhang et al., 2012).

From a total of 391 well measurements, the Barnett shale has average porosity of 5.52±0.28%, and average water saturation of 28.9±7.2% (Gale et al., 2007). Bowker (2007) noted that water saturation is quite difficult to measure in shales. Despite the importance of water saturation on methane sorption/desorption and molecular diffusion, there are few efforts extended in this regard with shale samples under either dry or wet conditions.

Methods

Sorption experiments were conducted on Barnett shale to evaluate methane retention as a function of temperature, pressure, and reversibility, using an apparatus and methodology developed by Dr. Tongwei Zhang of the Bureau of Economic Geology (BEG; Zhang et al., 2012; Figure 22). The apparatus does not work with mm-sized samples, for which sorption/desorption is largely controlled by the coupled sorption and migration processes in tortuous nanopores in shales; instead, these experiments used powdered shale samples, for which sorption/desorption is dominated by surface physical chemistry.

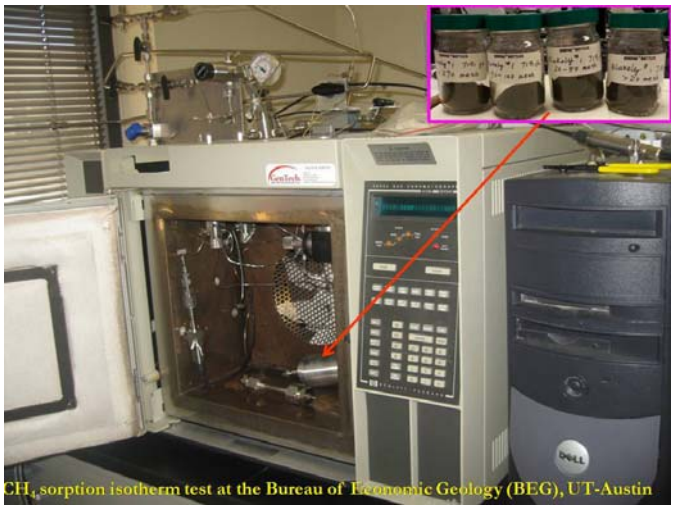

Figure 22. The BEG apparatus for measuring methane sorption isotherms.

The CH_4 sorption isotherm, which is the relation between amount of adsorbed CH_4 and gas pressure at a constant temperature, was measured in a gas adsorption measurement system at

BEG (Figure 22). Isothermal adsorption experiments were conducted at 35°C, 50°C, and 65°C, using ultra-high purity (99.999%) CH_4 as the adsorbate. The range of experimental pressure was 0–14.5 MPa (0–2,100 psia). Powdered samples of <75 μm were first pre-heated to remove moisture and other adsorbed gases before the gas adsorption test. Samples were then placed into the sample cell (7.15 mL in volume), and following a leak test the experimental setup was evacuated with a vacuum pump. Void volume measurements were individually conducted at 35°C, 50°C and 65°C, and applied in the calculation of the corresponding CH_4 adsorption isotherms. The experimental setup was then evacuated, and CH_4 was introduced into the reference cell. After equilibrium was reached (indicated by monitoring pressure variation less than 6.9×10^{-4} MPa within 5 minutes), the valve between the reference cell and the sample cell was opened, and the gas was expanded into the sample cell for gas sorption. By measuring the pressures before and after expansion, gas molar densities at different stages were calculated using an appropriate equation of state, and the amount of gas adsorbed at one pressure level could be determined. The isotherm was obtained by repeating these procedures with increasing gas pressure, until the highest desired gas pressure was measured. The detailed experimental construction is described in Zhang et al. (2012).

For the molecular diffusion measurement in powdered Barnett shale samples, we performed laboratory experiments using crushed shale powder samples. This removes other transport process encountered in larger-sized shale matrix (the focus of Task 6 below). An oxygen sensor was used to measure atmospheric oxygen diffusing through the sample, using the gas diffusion apparatus and methodology of Peng et al. (2012a; Figure 23). The results were then analyzed based on Equation 6 (Rolston and Moldrup, 2002; Peng et al., 2012a):

$$C_r = \frac{C_t - C_s}{C_0 - C_s} = \frac{2h\exp\left(-D_e\alpha_1^2 t/\phi_a\right)}{L\left(\alpha_1^2 + h^2\right) + h} \tag{6}$$

where C_t and C_0 are oxygen concentrations in the diffusion chamber at times t and 0, respectively, and D_e is the desired effective diffusion coefficient. An oxygen sensor (model Figaro KE-12, GS Yuasa, Japan) was used to detect the oxygen concentration, which was recorded with a CR 1000 data logger (Campbell Scientific, Inc., Logan, UT).The value of C_s is the atmospheric oxygen

concentration (20.93% under normal conditions). The parameter ϕ_a is air-filled porosity, and L is the sample length. The parameter h takes the value $h = \phi_a / a$, in which a is the volume of the chamber per sample area. The value of α_n is the positive root of the equation $h = \alpha_n \tan(\alpha_n L)$. The logarithm of C_r becomes linear in time (t) with a slope of $-D_e \alpha_1^2 / \phi_a$, so if values of α_1 and ϕ_a are known, then the value of D_e can be calculated.

Gas diffusion experiments were conducted using crushed shale (a mixture sample of Barnett shale powder of 7,105–7,164 ft; <75 µm). Four initial water saturations (dried at 60±2 °C, 10%, 20%, and 30%) were studied for their effect on gas diffusion in shale powder. To achieve initial uniform water saturation, an appropriate amount of de-ionized water is added to the shale powder, and held in a closed environment while it equilibrated. Water saturation of the shale was measured gravimetrically at the end of the gas diffusion tests.

Figure 23. An apparatus for measuring gas diffusion of crushed shale powder.

In geologic media, the effective diffusion coefficient (D_e) is considered to be the diffusion in the bulk fluid, as affected by the medium properties and fluid content. The value of D_e in Equation (7) is related to the tortuosity τ (>1), porosity ϕ (<1), and the aqueous molecular diffusion coefficient (D_0) of the diffusant (Gommes et al., 2009).

$$\frac{D_e}{D_0} = \frac{\phi}{\tau^2} \tag{7}$$

The tortuosity τ is purely geometric and accounts for a tortuous path around the solid particles in the porous medium. The τ value is usually expressed as:

$$\tau = L_e/L \tag{8}$$

where L is the straight-line distance between the endpoints defining the diffusion path, and L_e is the length of the actual diffusion pathway between those same two points ($L_e>L$). (Some researchers define L/L_e as the tortuosity, in which case $\tau< 1$, and τ is placed in the numerator in Equation 7). Tortuosity (L_e/L) reduces diffusion in two ways: (1) increasing the travel path length by a factor L_e/L; and (2) decreasing the concentration gradient along the pathway, again by a factor L/L_e (Epstein, 1989). Therefore, the tortuosity is squared in its relation to D_e to provide a geometrical meaning (Gommes et al., 2009).

Sometime a tortuosity factor ζ is defined as τ^2 (e.g., Hu and Wang, 2003). The relationship between D_e in porous media to tortuosity (or tortuosity factor) in the literature is quite inconsistent. The work of Gommes et al. (2009) justified using the square of the tortuosity. In most cases, this inconsistency is not detrimental because tortuosity is commonly treated as a numerical factor, and there is no attempt to give it a precise geometrical meaning (when it is to be interpreted as the ratio of the diffusive path lengths to the straight length across the solid). Sometimes a dimensionless diffusivity (D_e/D_0) is used to describe the reduced chemical diffusion in a porous media, without reference to tortuosity and constrictivity (Peng et al., 2012a).

In addition, the combination of the porosity, tortuosity and the constrictivity factor δ ($\leq$1) can be considered to relate D_e in a porous medium (Hu and Wang, 2003), to give Equation 9. The value of δ would be 1 except for the diffusion in narrow pores (e.g., <10 nm). In these pores, the value of D_e may be reduced through an increase in drag resulting from a greater fluid viscosity near the solid. This drag effect is especially applicable in small pores or narrow pore throats that have diameters of the same order of magnitude as the diffusant. The value of δ accounts for this steric hindrance effect, and can be estimated using empirical equations reported from the chemical engineering literature (Rekin, 1954; Grathwohl, 1998). Most diffusing species of

interests have a molecular diameter < 1 nm; for these, significant steric hindrance is expected when pore diameter is < 10 nm (Grathwohl, 1998). This narrow pore situation is applicable for the tight shales, which have a median pore-throat diameter about 5 nm for Barnett shale, but we are not aware of publications that quantify the constrictivity factor of gas and oil molecules in shale nanopores.

$$\frac{D_e}{D_0} = \frac{\phi}{\tau^2 \delta} \tag{9}$$

Results and Discussion

The reservoir conditions for Barnett shale are reported to be 3,500 psi and 170 °F (77 °C) (Steward, 2007). Our methane sorption data (Figure 24) show that sorption onto Barnett shale powder samples is strongly pressure-dependent, and marginally related to temperature, similar to the report of Zhang et al. (2012). Miller (2010) also reported a strong pressure dependency of methane sorption.

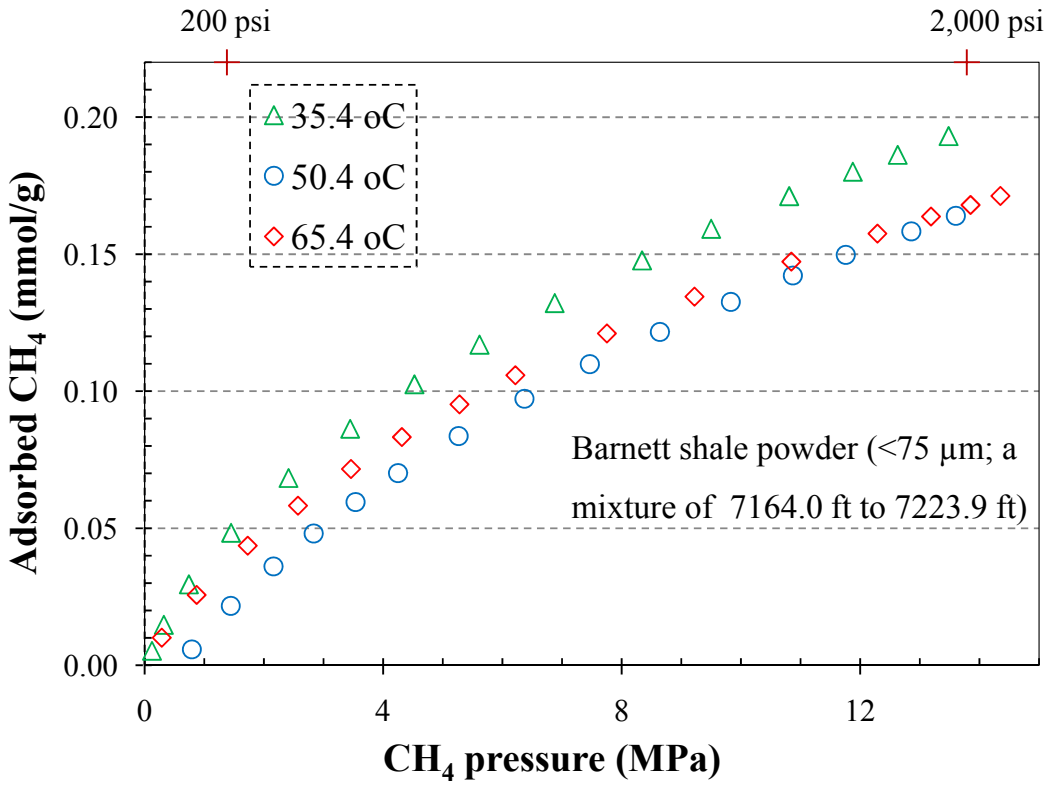

Figure 24. Methane sorption as a function of pressure and temperature. For Y-axis, 1 mmol/g = 711.2 scf/ton. Experimental temperatures of 35.4, 50.4, and 65.4°C are equivalent to 95.7, 123, and 150°F.

Figure 25 shows the reversible CH_4 sorption-desorption isotherm onto and from the Barnett shale powder samples. There is almost no hysteresis in this isotherm. We are not aware of other reports about the reversibility of methane sorption onto shales. Such methane sorption parameters can be used for production decline analyses.

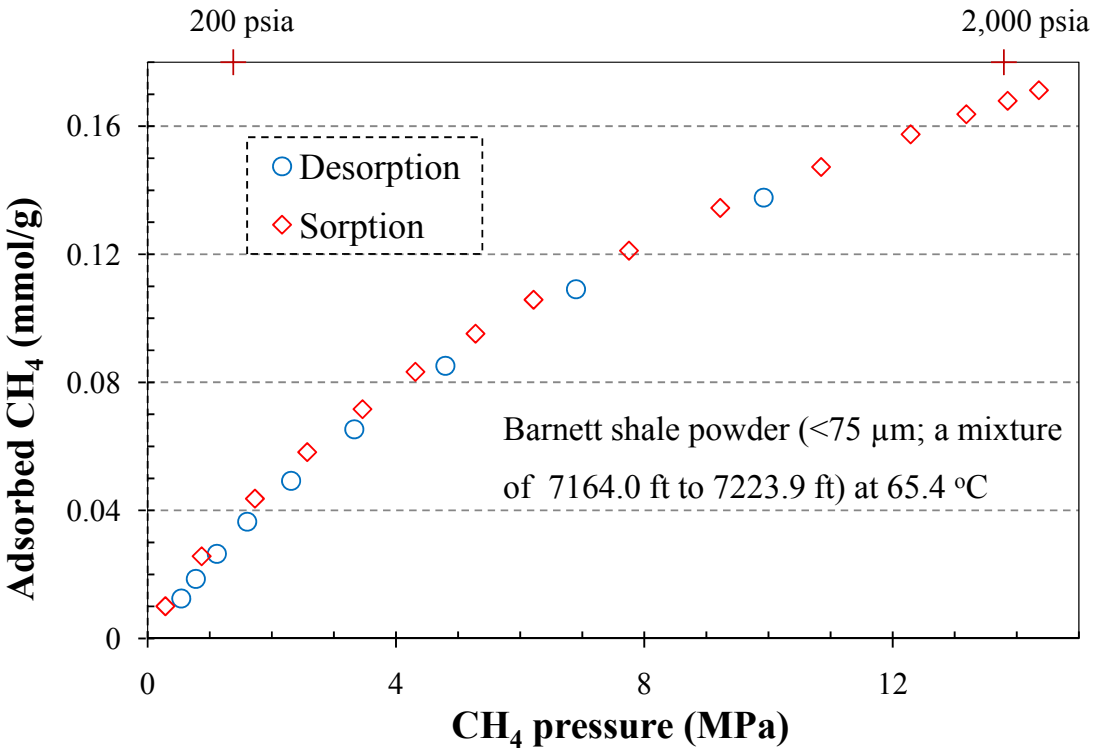

Figure 25. Methane sorption and desorption as a function of pressure at 65.4°C (150°F).

As shown in Figure 26 for an example diffusion test result, the processed data are quite linear (values of R^2 for the linear regression are larger than 0.99) on a log-linear plot, confirming the validity of the experimental methodology. According to Equation 6, the effective diffusion coefficient, D_e, is given by the slope of the linear data (Figure 26).

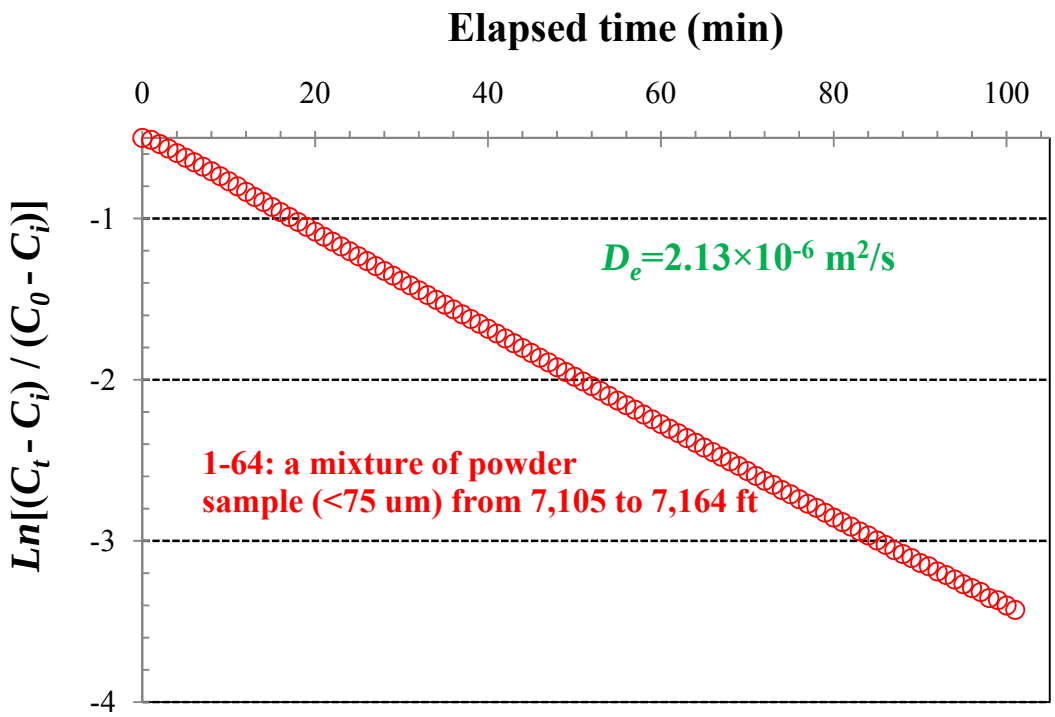

Figure 26. Measured oxygen concentration in natural log scale vs. experimental time for Barnett shale powder.

Effective diffusion coefficients D_e, and associated tortuosities are presented in Table 5 for different water saturations. The results show that even a modest increase in water saturation will greatly decrease the D_e value. As the water saturation increases, the air-filled porosity decreases, which results in a decrease in the D_e value. When the air-filled porosity decreases by one-half (from 39.2% at air-dry condition to 20% at 20% water saturation), the D_e value decreases by a factor of 4, from 2.0×10^{-6} to 0.5×10^{-6} m^2/s.

These results indicate a simple relationship: D_e is proportional to the square of air-filled porosity. This relationship agrees with the predictions of percolation theory (Hunt et al., 2014; Ghanbarian and Hunt, 2014), indicating that there is no additional tortuosity contributed by the shale nanopores. The implication is that gas-phase diffusion through moist shale powder is like gas-phase diffusion through any other moist powder: it's about the pores between the powder grains, and their connectivity, rather than being about the nanopores inside the powder grains.

Table 5: Measured effective diffusion coefficient and tortuosity of Barnett shale powder as a function of water saturation

Water saturation	Air porosity (%)	D_e (m^2/s)	Tortuosity
Air-dry	39.2	2.13×10^{-6}	1.94
10%	33.9	1.56×10^{-6}	2.10
20%	20.0	5.11×10^{-7}	2.82
30%[#]	20.0	3.96×10^{-7}	3.21

[#] The sample height is 1.0 cm, compared to 5.1 cm for other tests.

Following hydraulic stimulation of a shale reservoir, some10–30% of the hydraulic fracturing fluid remains in the shale formation, probably imbibed only a few mm deep into the matrix block. Reduced gas diffusion rates as a function of increased water saturation would lead to low gas production. The success of commercial gas production suggests that the imbibed hydraulic fluid mostly ends up in mineral pore spaces of the shale because of the wettability attraction; there it does not totally block the migration pathways of gas, which predominately resides in organic pores.

Task 6: Fracture-Matrix Interaction in Intact Shale

Objectives

In low-permeability unsaturated fractured shale, fluid flows predominantly through the interconnected fracture network, with some fluid imbibing into the neighboring matrix rock. Both imbibition (from the capillary pressure gradient) and diffusion (from the concentration gradient) drive mass transfer of chemicals between the fractures and shale matrix. In low-permeability shale after hydraulic stimulation, fluid (gas and liquid) flows predominantly through the interconnected fracture network, with some fluid moving into or out from the neighboring matrix rock. Diffusion transports hydrocarbon molecules from the matrix into fractured pathways for production; once in the fracture network, fluid flows relatively easily to the well bore. Much of the natural gas (about 45% for the Barnett) is sorbed to the shale matrix, so it must desorb into the interconnected pore spaces before diffusing to the fracture network.

Both desorption and diffusion are slow in the shale matrix, so initial production rates quickly decline to below economically sustainable rates. In other words, **commercial viability is limited by low hydrocarbon diffusion rates in tortuous pathways in nano-sized pore spaces**, as illustrated schematically in Figure 27. Quantifying matrix diffusion is critically missing in understanding fluid migration in the fractured shale and the production decline behavior. But despite the importance of diffusion to gas/oil production, there is no systematic study examining permeability and diffusivity of the Barnett (Bowker, 2007). This work addresses this knowledge gap.

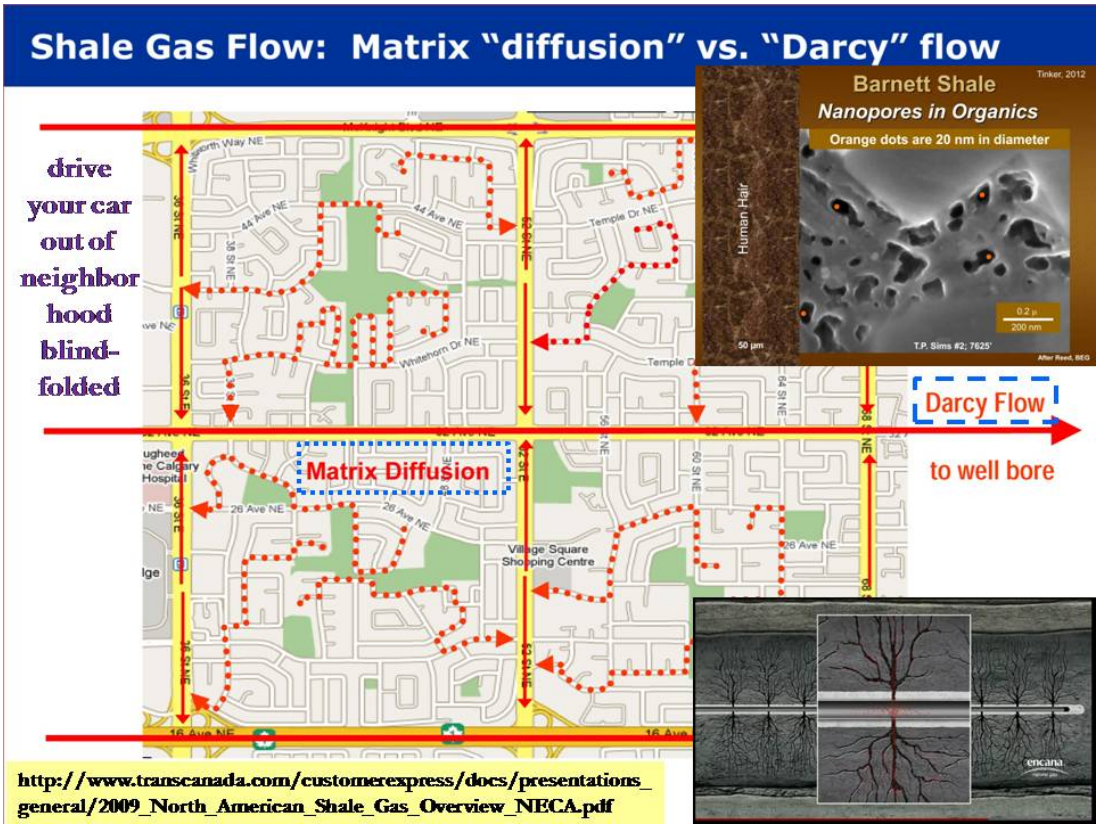

Figure 27. Conceptual model of fracture-matrix interaction and resultant shale gas production (modified from Pflug, 2009).

This task is to experimentally measure solute diffusion in cm-sized samples of Barnett shale. In addition, we will assess the tracer imbibition into shales at different initial water saturations from its relevance to fluid distribution during hydraulic stimulation and consequent implications

on hydrocarbon recovery. The success of commercial gas production suggests that the imbibed hydraulic fluid ends up in mineral pore spaces of the shale because of the wettability attraction; there it does not totally block the migration pathways of gas that predominately reside in organic pores. In this study, we used tracers dissolved in water or *n*-decane (water and oil phases) to target their association to mineral or kerogen phases.

Methods

For both imbibition and diffusion experiments, the tracer solutions discussed in Task 3 were used; these solutions contained both non-sorbing (bromide and perrhenate) and sorbing (cesium, cobalt, samarium, and strontium) tracers.

Using an approach similar to that reported by Hu et al. (2002), tracer imbibition tests were carried out to investigate the coupled processes of chemical sorption and transport under unsaturated conditions. This unsaturated-transport-sorption technique overcomes some shortcomings (e.g., use of micrometer-sized crushed samples and saturated conditions) of conventional transport experiments in rock, and yields a more realistic evaluation of chemical transport in unsaturated intact rock at the centimeter scale.

Similar to the water imbibition experiments described in Task 2, the tracer imbibition tests were carried out by suspending from a balance a rectangular prism (about15 mm-sized) shale sample inside a humidity-controlled chamber. After a predetermined period of time (about 1–2 days for shales of this sample length), the sample was lifted out of the reservoir, frozen with liquid nitrogen, freeze-dried, and kept in dry storage until LA–ICP–MS analysis. Tracer distribution was mapped by LA–ICP–MS on the tracer-entry and tracer-exit faces to evaluate source concentration and to determine the presence of tracers at the sample top. Then, after crack-opening, tracer distributions on the interior face and side face were mapped as a function of distance above the imbibing bottom (i.e., tracer-entry face).

Aqueous tracer imbibition was conducted at three initial water saturation levels: drying at 60±2°C, then partial water-saturating to equilibrium at both 75% and 98% relative humidity (RH). Partial saturationwas achieved by holding the shale samples in chambers with a constant RH value, as controlled by over-saturated salts (Table 6), and periodically weighing samples

until they reach a stable weight (i.e., saturation). According to Kelvin's equation, each RH value relates to a capillary pressure, which also relates to a specific curvature of the air/water meniscus. At a given RH, water vapor will condense inside pores with equivalent diameter less than or equal to the meniscus curvature. These RH chambers are held at a constant temperature of 22.5°C inside an incubator. After 3 months, equilibrium having been attained, the partially saturated shale samples were used for tracer imbibition tests.

Table 6: Humidity and capillary pressure over saturated salt solutions at 22.5°C

	NaCl	**$CaSO_4$**
RH (%)	75.4	98
P_c (MPa)	38.5	3.52
Diameter of meniscus curvature (nm)	7.55	106

In addition to tracer imbibition in water (aqueous phase), we also conducted tracer imbibition in organic *n*-decane phase to examine the tracer's association with kerogen phase. The identified tracer chemicals include >99% pure tracer-containing organic reagents [1-iododecane $CH_3(CH_2)_9I$, and trichlorooxobis (triphenylphosphine) rhenium(V) ($[(C_6H_5)_3P]_2ReOCl_3)$], with the elements iodine (I) and rhenium (Re) from these organic chemicals readily detected by LA–ICP–MS. Trichlorooxobis (triphenylphosphine) rhenium(V) was first dissolved in a non-polar organic solvent (acetone) until over-saturated, filtered to obtain the over-saturated liquid, and then added to *n*-decane at a volume ratio of 1:30. In addition, 1-iododecane was added into the above fluid at a volume ration of 1/100.

After tracer imbibition tests, whether with water or *n*-decane, the shale samples were frozen with liquid nitrogen, kept at -60°C in a freezer, freeze-dried, then stored at <10% relative humidity until LA–ICP–MS analysis. Both the top (tracer-exit) and bottom (tracer-entry) faces were spot-checked for the presence of tracers, and then the sample was cut in the middle from the top face, transverse-wise with respect to the imbibition direction, using a low-speed diamond saw (Buehler IsoMet). De-ionized water was used as the saw lubricant following *n*-decane

imbibition. Following aqueous solution imbibition, the saw was lubricated with a general purpose vacuum pump fluid (Varian Technologies, Lexington, MA), after which the sample was cleaned by sonicating in acetone for 20 min before laser ablation. A grid of spot analyses was then performed by LA–ICP–MS on the saw-opened interior face, as well as the side face after peeling off the quick-cure epoxy (Task 2), to map the tracer distribution from imbibition.

For chemical diffusion into saturated Barnett shale, dry shale samples were evacuated for one hour at 99.91% vacuum, and saturated by allowing de-ionized water to invade the evacuated sample. Following the approach published in Hu and Mao (2012), samples were then placed on a Teflon mesh inside the tracer solution reservoir, such that only the bottom of the sample (to reduce hydraulic head differences) touched the tracer solution, which was constantly stirred with a magnetic stirrer. The reservoir volume was on the order of 800 mL, compared to the samples' pore volume of less than 1 mL; this high volume ratio ensured an approximately constant tracer concentration (as required to satisfy the boundary condition of the applicable mathematical solution of the diffusion equation). The lidded reservoir was held at a constant 23°C by being placed inside an incubator. At fixed diffusion times (about 1, 2, and 3 days), some shale samples were removed from the reservoir, frozen with liquid nitrogen, freeze-dried, then stored at low relative humidity prior to LA–ICP–MS analyses. First we spot-checked for presence of tracers at the diffusion-bottom and upper faces. Then a line survey was conducted on the sample wall surface, followed by two survey lines on the interior face after the shale sample was cracked open (Hu and Mao, 2012); the use of a low-speed diamond saw with dry cutting to create a smooth interior surface for 2-D mapping was developed and employed later.

An analytical solution (Equation 10) can be used to calculate the diffusion distance into a homogeneous semi-infinite medium (Hu and Mao, 2012):

$$C(x,t) = C_0 erfc\{x/[2(D_e\, t)^{0.5}]\} \qquad (10)$$

where $C(x, t)$ (M L^{-3}) is the observed concentration based on an initial concentration C_0 (M L^{-3}), x (L) is the distance from the inlet boundary into the medium, t (T) is the time, D_e ($L^2\, T^{-1}$) is the effective diffusion coefficient of the diffusant in the porous medium, and *erfc* is the complementary error function. The fitted D_e value is then used to calculate the tortuosity of shale matrix, according to Equation 7.

Results and Discussion

Tracer imbibition results under three initial water saturations for Barnett shale 7,136 ft (Forestburg limestone) are shown in Figure 28. In the imbibition experiment with low initial saturations of dry and 75% RH initial conditions (Figure 28A and 28B), the non-sorbing perrhenate front is steep because a strong capillary force drives advective flow and tracer transport; a relatively uniformly distributed concentration of about 50 mg/kg is detected at the mapped area of 5 mm×10 mm. For the test of wet sample initially equilibrated at 98% RH, the capillary force is weak (Table 6), only imbibing non-sorbing tracer into about 2 mm. During imbibition into a moist medium, tracers in the "new" water disperse by mixing with "old" water, and so a more gradual perrhenate front is observed (Figure 28C). In other words, dispersion becomes more pronounced for chemical transport under high initial saturation.

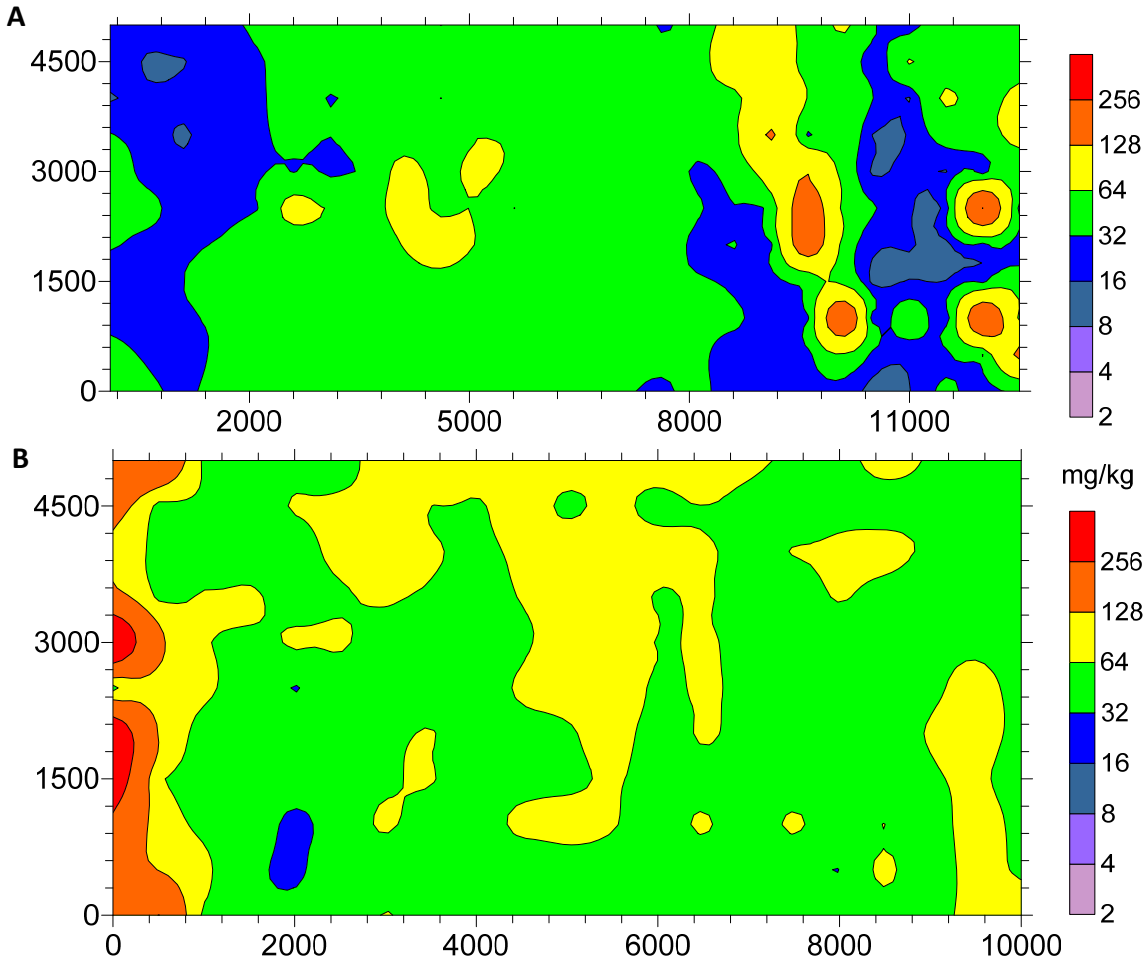

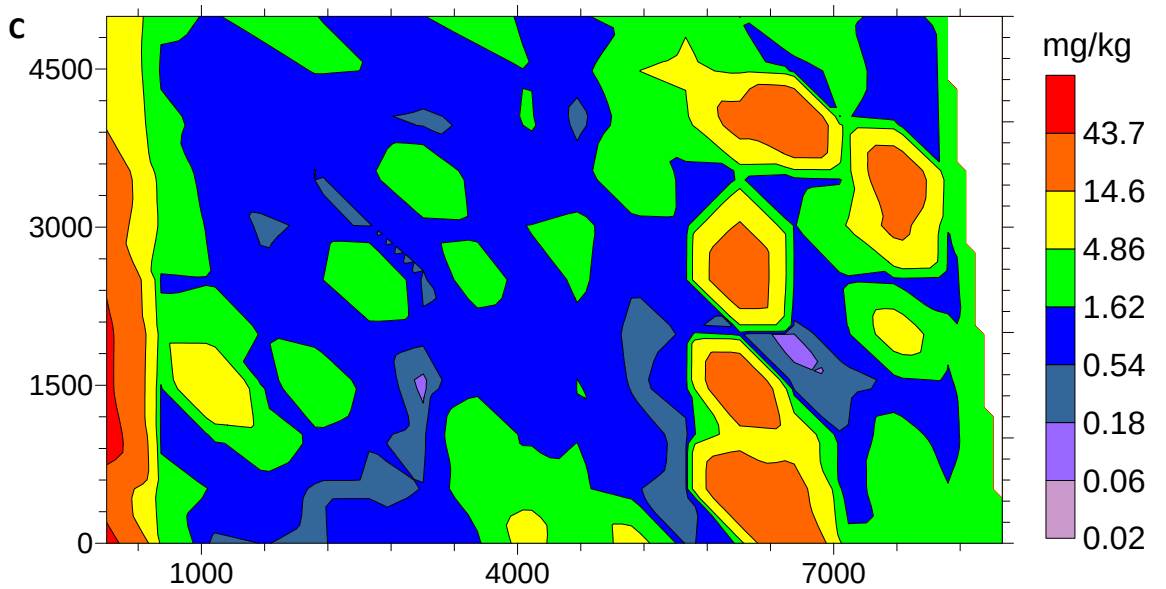

Figure 28. Aqueous tracer imbibition penetration profile, mapped on the interior face, for the non-sorbing tracer ReO_4^- in Barnett shale 7,136 ft, the Forestburg limestone. Top (A) initially dry (imbibition time of 46.6 hr); Middle (B) equilibrated at 75% RH (imbibition time of 47.9 hr); and Bottom (C) equilibrated at 98% RH (imbibition time of 48.4 hr). Imbibition proceeded from left to right, and the X- and Y-scales are in µm. The LA–ICP–MS detection limit for Re in Barnett shales is about 0.05 mg/kg.

Figure 29 presents the measured concentration distribution for non-sorbing perrhenate tracer at 2 mm×2 mm grid on the bottom (imbibing) face. Except for the high concentration area to the right, the other places in the grid have perrhenate concentration at 30–70 mg/kg, consistent with the concentrations of the interior face (Figure 28A), for the same sample.

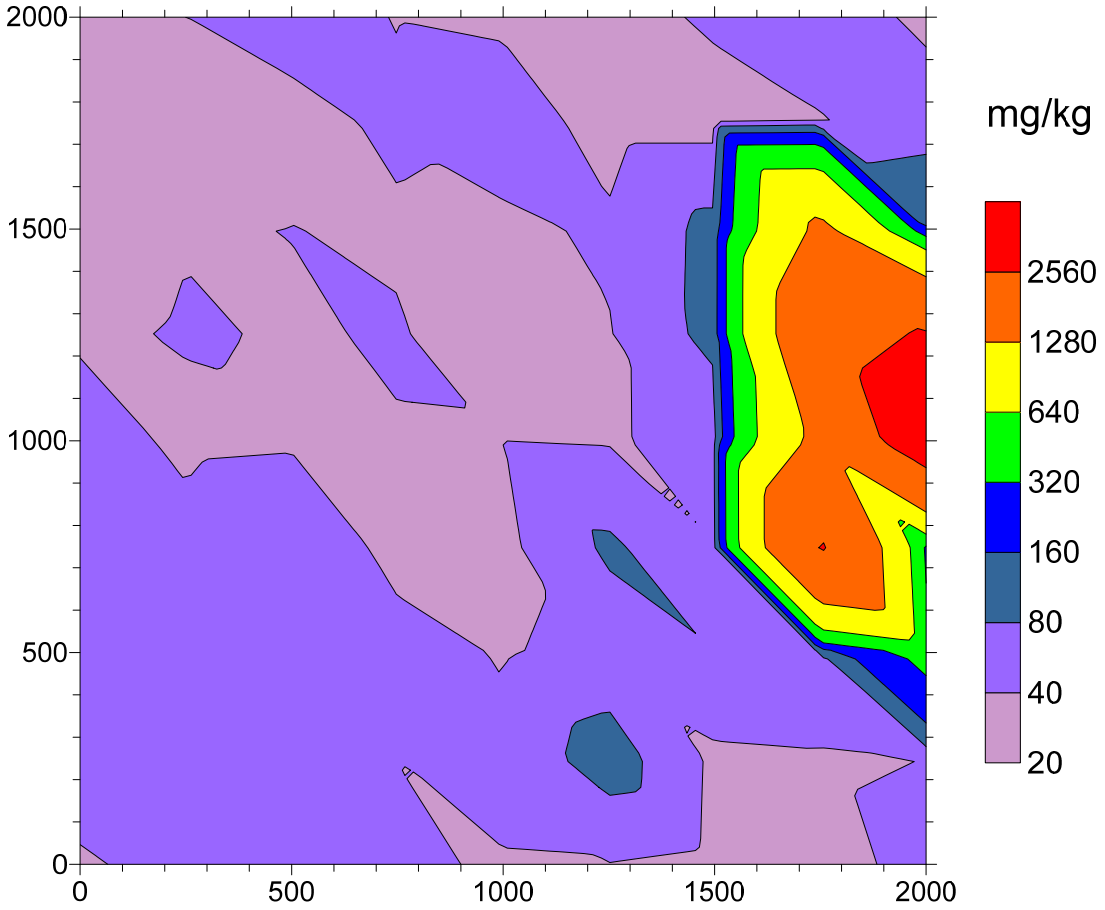

Figure 29. Aqueous tracer distribution, mapped on the imbibing face in the middle region of 15 mm×15 mm face, for non-sorbing tracer ReO_4^- in Barnett shale 7,136 ft (Forestburg limestone) under initially dry condition after imbibition time of 46.6 hr. The X- and Y-scales are in µm.

In contrast with the imbibition distance of nearly 15 cm for non-sorbing perrhenate tracer under initially dry and water saturation equilibrated at 75% relative humidity, the imbibition penetration for sorbing tracer Cs^+ lags far behind, confined to less than 1 mm from the imbibition bottom (Figure 30) by its interactions with shale minerals.

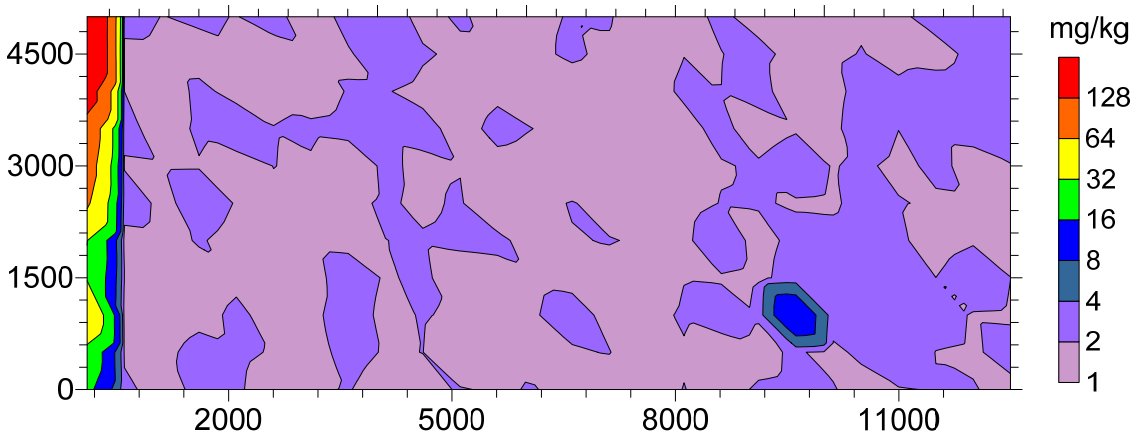

Figure 30. Aqueous tracer imbibition penetration profile, mapped on the interior face, for sorbing tracer Cs^+ in Barnett shale 7,136 ft (Forestburg limestone) under initially dry condition after an imbibition time of 46.6 hr. Imbibition proceeded from left to right, and the X- and Y-scales are in µm. Pink areas indicate a concentration below 2 mg/kg, and the Cs background level detected by LA–ICP–MS in Barnett shales is about 1.5 mg/kg.

Consistent with the limited penetration of about 0.5 mm for non-sorbing perrhenate tracer observed for the interior face (Figure 28C), perrhenate movement along the sample side is also mostly limited to about 0.75 mm (Figure 31). However, it's noticeable that a portion (up to about 10 mg/kg out of the concentration of about 500 mg/kg; i.e., a factor of 1/50) detected near the imbibition bottom. Note that the shale under *in-situ* reservoir conditions is expected to be at a similar water saturation, so this work provides direct evidence regarding chemical imbibition during hydraulic fracturing.

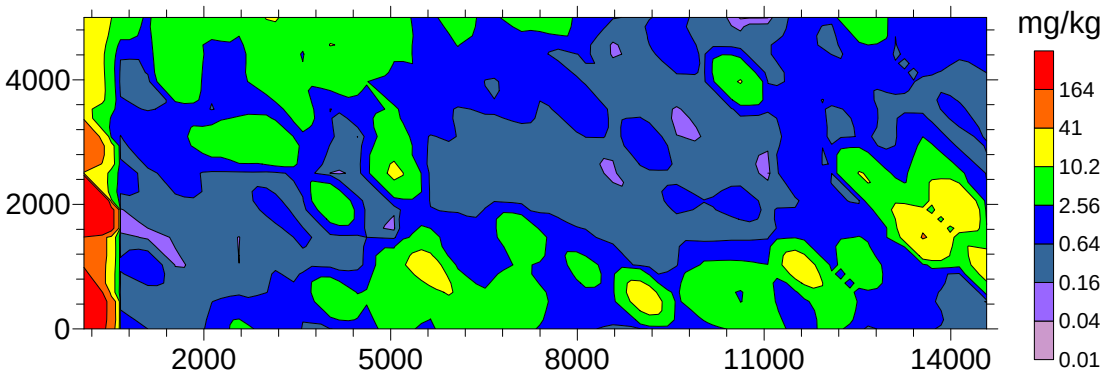

Figure 31. Aqueous tracer imbibition penetration profile, mapped on the side face, for the non-sorbing tracer ReO_4^- in Barnett shale 7,136 ft (Forestburg limestone) under initial sample saturation equilibrated at 98% relative humidity after an imbibition time of 48.4 hr. Left side is the imbibition face, and the X- and Y-scales are in µm.

Results for *n*-decane tracer imbibition into Barnett shale 7,169 ft are shown in Figure 32. Compared to the aqueous tracer imbibition (Figure 28A), the distribution of organic fluid based tracer seems to be more sporadic. The high presence of Re tracer in the top side of the sample is probably a wall effect: *n*-decane may imbibe along the wall faster than through the tortuous interior pathways. A similar faster wall migration is observed in tracer diffusion tests (pages 68–71). Because of this faster exterior surface flow, some tracer appears to have imbibed from the far side (i.e., top face). Note the low background concentration zones at about 7,000–9,000 µm region from the sample imbibing bottom, which separate the imbibing fronts from both ends.

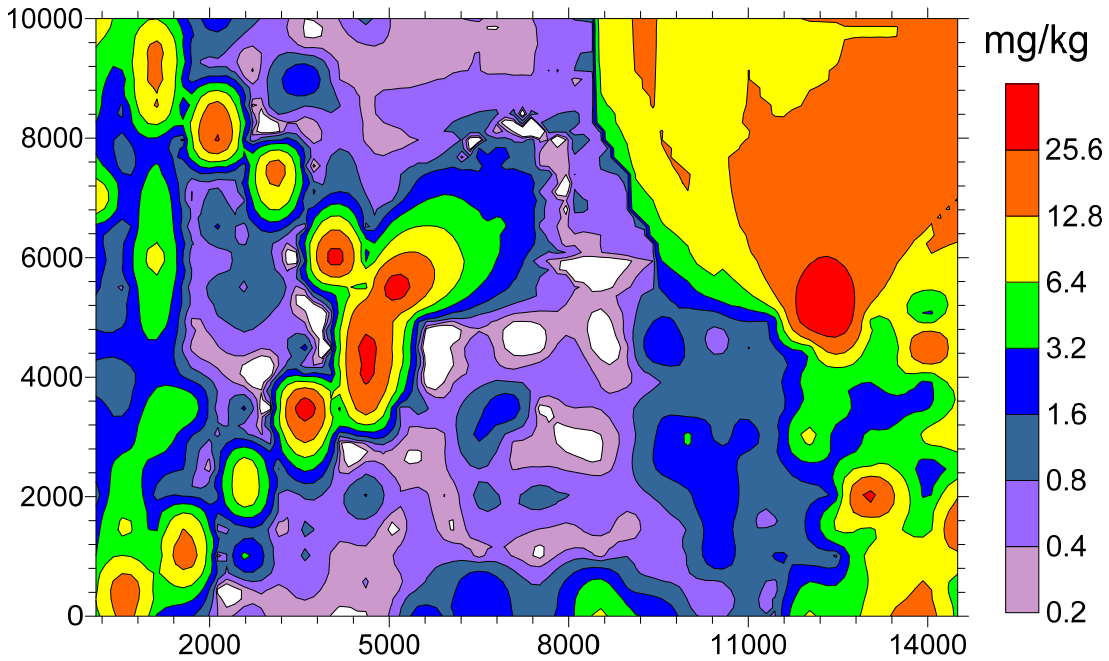

Figure 32. *n*-decane tracer imbibition penetration profile for non-sorbing tracer Re in Barnett shale 7,169 ft under initially dry condition at imbibition time of 72.2 hr. Left side is the imbibition face, and the X- and Y-scales are in µm. White areas indicate a concentration below 0.2 mg/kg.

The organic fluid (*n*-decane) is expected to be preferentially attracted to the hydrophobic component (kerogen) of the shale matrix, which for Barnett shale is reported to have pore sizes ranging from less than 1 µm to tens of µm (Loucks et al., 2009). Our own field emission-SEM work on Barnett shale samples also show that kerogen grains are found dispersed through the shale matrix (Figure 33). The porosity of kerogen grains can be as much as 20% for Barnett shale

(Loucks et al., 2009). An understanding of the distribution and migration of the hydrocarbons stored in these organic pores is critically needed. We are continuing our SEM-based studies of how shale phases (mineral versus kerogen) correlated with the distribution of phase-based tracers (brine versus *n*-decane).

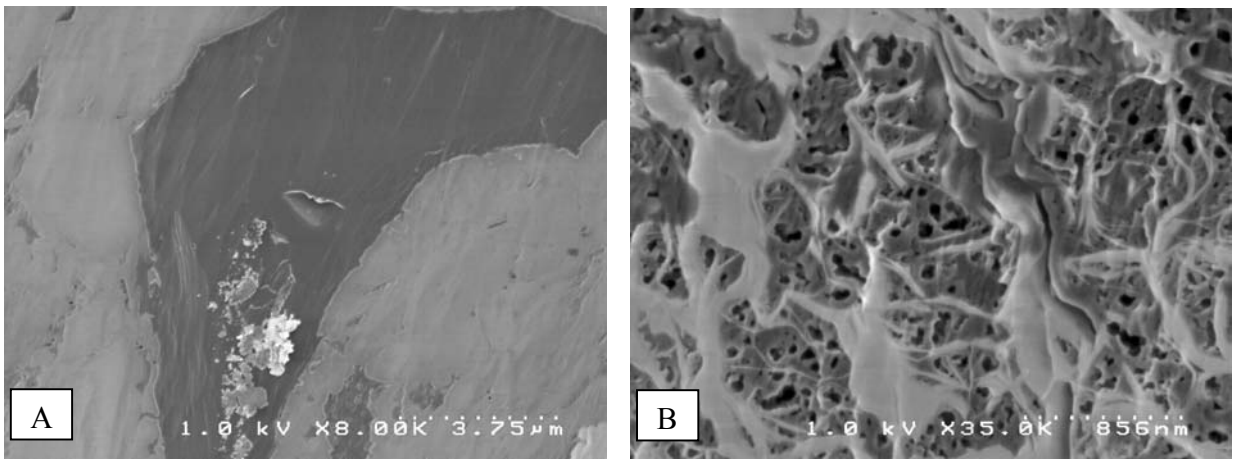

Figure 33. Field Emission-SEM images of kerogen and mineral phases and associated pore spaces in Barnett shale 7,109 ft, obtained from UTA's Hitachi S-3000 variable pressure SEM. Figures 33A and 33B are shown at different observational scale bars and associated resolutions, with Figure 33B focusing on the kerogen area.

We now present the results of saturated diffusion tests. Figure 34 presents relative tracer concentration profiles, as measured with LA–ICP–MS, in a representative Barnett shale sample following one day of diffusion time. The "surface" data were obtained from the outside surface of the shale sample, where 2-D surface diffusion is much faster than diffusion through the interior face (data obtained by cracking open the sample for LA–ICP–MS mapping) where tracers have to migrate through tortuous 3-D pathways. Only a very small amount (1/1,000th of stock concentration) of non-sorbing perrhenate ReO_4^- molecules has diffused about 3 mm through the interior, and the line surveys of LA–ICP–MS mapping show high spatial variability of tracer concentration along the diffusion distance. These interior tracer concentrations, limited by tortuous 3-D pathways, are barely above the background detection limit of ReO_4^-, and four orders of magnitude lower than the results of bottom diffusion face. This indicates that only a very small portion of the nanopores in the Barnett shale are connected to the sample surface for

diffusion. The practical implication is that the out-diffusion of natural gas is also expected to be slow, of limited quantity, and largely from shale matrix that is within some small distance from a fracture. Note that such results are obtained under atmospheric pressure; under reservoir pressure conditions, the distance of connected shale nanopores from the sample edge (i.e., the fracture face) will be somewhat larger. Follow-up investigations on this issue are needed. However, probably the pressured diffusion distance will still be very limited for shale samples, given the high-pressure Wood's metal test discussed in Task 4.

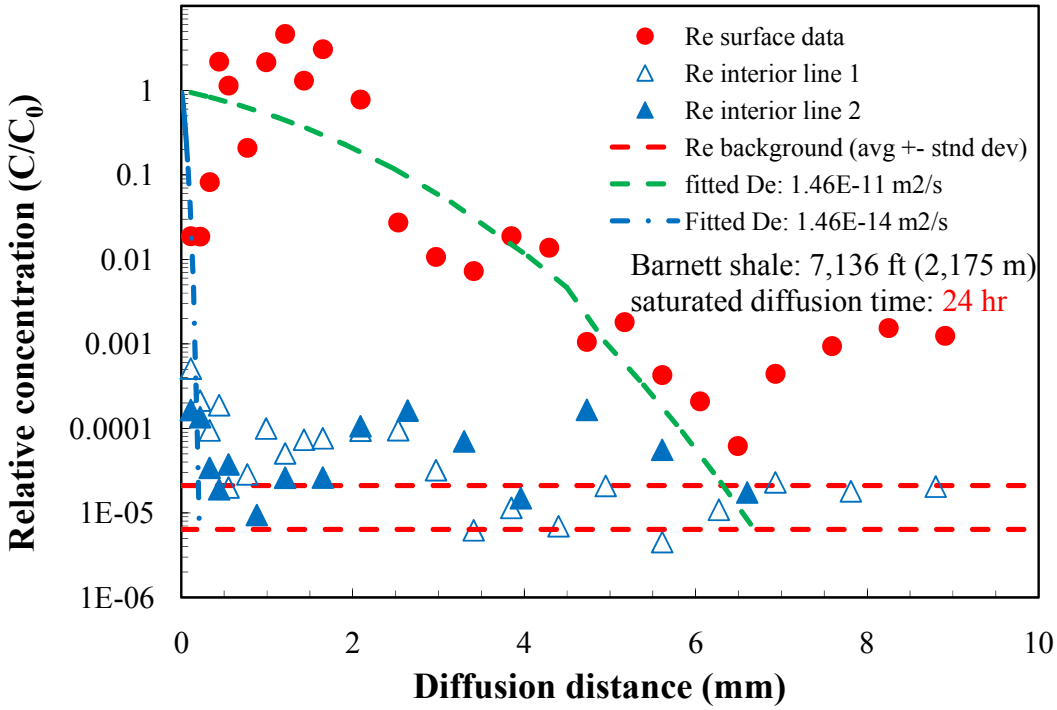

Figure 34. Diffusion profile and measured effective diffusion coefficient for non-sorbing tracer ReO_4^- in surface (sample exterior) and interior faces of Barnett shale 7,136 ft (Forestburg limestone); red dashed lines are the background levels (±1 standard deviation) of ReO_4^-.

Effective diffusion coefficients based on the analytical solution (Equation 9) were fitted to the observed relative concentration values. The fitted ReO_4^- effective diffusion coefficients were 1.46×10^{-11} m^2/s for the exterior (sample surface wall diffusion) and the very low value of 1.46×10^{-14} m^2/s for the interior face, corresponding to tortuosity values of 1.13 and 35.6, based on Equation 7 and given the ReO_4^- D_0 value of 1.46×10^{-9} m^2/s. Note that the analytical solution.

i.e., the classic Fickian diffusion, assumes a well-connected pore space (see Task 2). That solution apparently does not capture the diffusion profile of interior diffusion, which results from tortuous pathways in poorly connected pore spaces. Experimental results from Tasks 2–6 consistently indicate poor pore connectivity of Barnett shales. The larger interior tortuosity from the diffusion tests is similar in magnitude to that from the MICP data (Table 2).

Two-dimensional elemental mapping for tracer ReO_4^- was also conducted for both the side (exterior) wall and interior face (Figure 35). Consistent with the line survey of Figure 34, the 2-D side wall diffusion is much quicker than the 3-D interior diffusion, with the concentration of non-sorbing ReO_4^- tracer differing in several orders of magnitude. While for the interior face, this detailed 2-D mapping results are also consistent with the line survey of Figure 34, with the sub-mg/kg ReO_4^- concentration confined within the first 0.5 mm region into the sample, and a sporadic and very low, yet detectable, concentration into 4 mm. Note that four "hot" zones to the right shows up from a single value of measured high concentration.

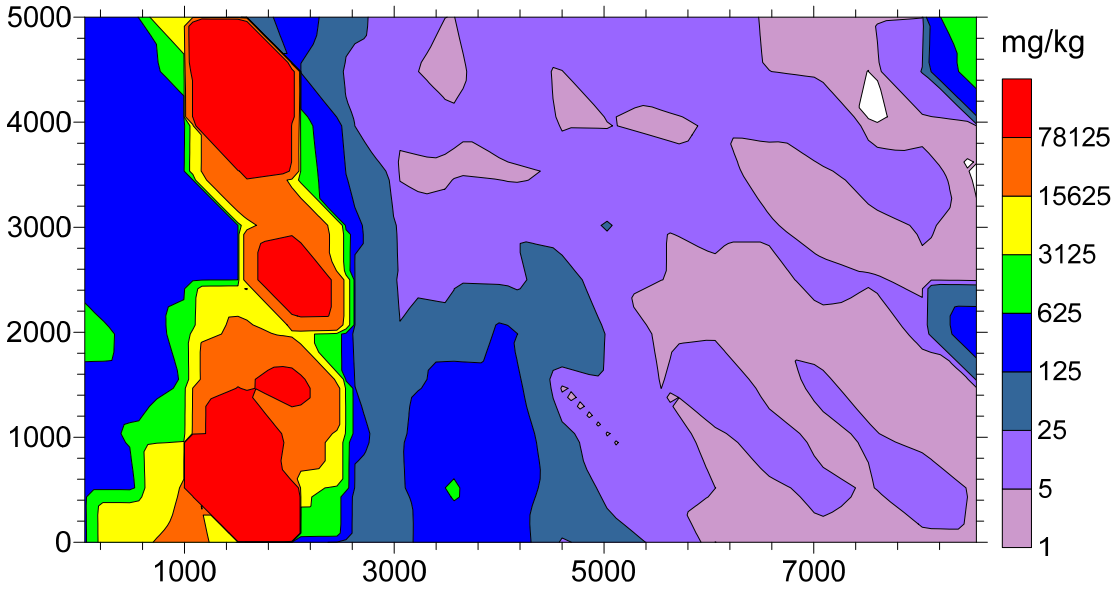

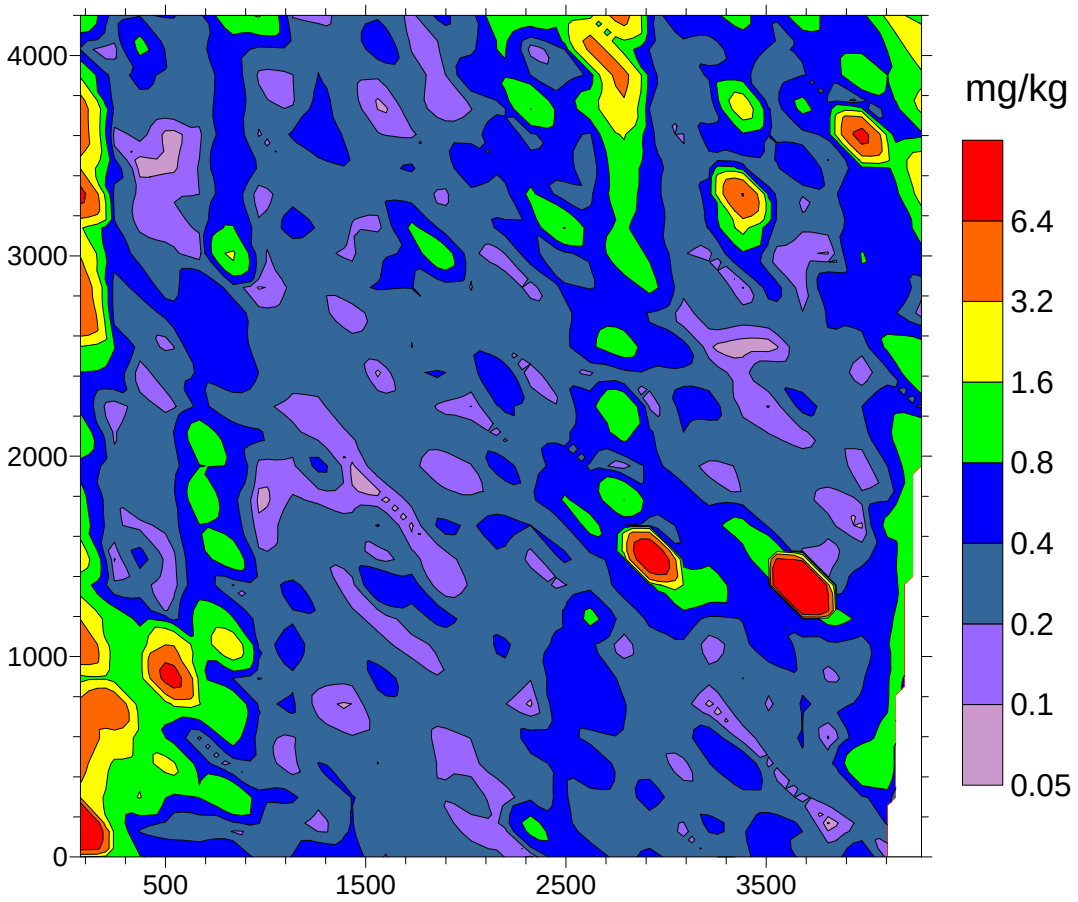

Figure 35. Diffusion profile for non-sorbing tracer ReO_4^- on the sample's exterior (top panel; 500 µm spacing between spots) and interior (bottom panel; 150 µm spacing between spots) faces. Sample is Barnett shale from 7,136 ft (Forestburg limestone).

Task 7: Pore-Scale Network Modeling

Objectives

The insights gained regarding pore structure in Barnett shale from the above complementary tasks were evaluated for how this pore structure might control hydrocarbon production at the field scale. We examine the production decline curves of wells in the Barnett shale formations. Gas production rates were obtained from the Texas Railroad Commission and DrillingInfo database, which has been provided to UTA for academic research and teaching usage.

The near-universal reliance on the empirical Arps equation (1945) for production decline curves has been recently challenged by (for example) power law exponential decline and

modified hyperbolic decline equations, but these lack a theoretical basis. Examining gas production from Barnett shale, Silin and Kneafsey (2012) reported a square-root-of-time relationship at early times, followed by an exponential decline for later time; this may be interpreted as a transition from linear to boundary-dominated flow.

The Arps equation (1945) is presented as

$$Q_g = \frac{Q_{gi}}{(1 + bD_i t)^{(1/b)}} \tag{11}$$

where q_g is gas production rate; q_{gi} is initial gas production rate; D_i is initial decline rate (percent per year); t is cumulative time since start of production; and b is the decline exponent. The b value is very important in the long-term production behavior. When b= 0, decline is exponential (very fast decline); when b=0.5, it is hyperbolic; and when b=1, decline is harmonic. The key assumptions for the Arps equation are that the well is producing (i) at constant bottomhole pressure; and (ii) from an unchanging drainage area with no-flow boundaries.

When verifying the dimensionality of equations 34–36 of Silin and Kneafsey (2012) with the help of Dr. Zhiming Lu of Los Alamos National Laboratory, we saw that the equations as published were in error. The correct equations are:

$$t^* = \left(1 + \frac{\rho_0 \rho_k S_k c_f}{c_g \phi}\right) \frac{\mu \phi D^2}{k p_R} \frac{1}{\alpha^2} \tag{12}$$

$$Q(t) = 2A \frac{c_g}{\rho_0} \sqrt{\left(\phi + \frac{\rho_0 \rho_k S_k c_f}{c_g}\right) \frac{k}{\mu p_R}} \frac{p_R^2 - p_w^2}{\alpha \sqrt{t}} \tag{13}$$

$$Q(t) = 2A \frac{c_g}{\rho_0} \frac{k}{\mu D} \left(p_R^2 - p_w^2\right) \exp\left[-3 \frac{p_w}{p_R} \frac{1}{\left(\phi + \frac{\rho_0 \rho_k S_k c_f}{c_g}\right)} \frac{k p_R}{\mu D^2} t - \frac{1}{\alpha^2}\right] \tag{14}$$

$Q(t)$ in Equations13 and 14 has units m^3/s. Definitions of all parameters in these equations are given in Silin and Kneafsey (2012).

Methods

Monthly gas production data for all wells in the Barnett shale are available from the Texas Railroad Commission (http://webapps.rrc.state.tx.us/PDQ/home.do), and these data were later supplemented by the complimentary access to DrillingInfo database. We first analyzed 22 horizontal wells drilled from one pad at the edge of UTA campus, by Carrizo Oil and Gas Inc. (Figure 36). We then selected the first eight wells drilled in Johnson County in 2004 by Devon Energy, the largest producer of the Barnett play. These horizontal wells have the longest production history in Johnson County, which has been recognized as a good gas-producing area.

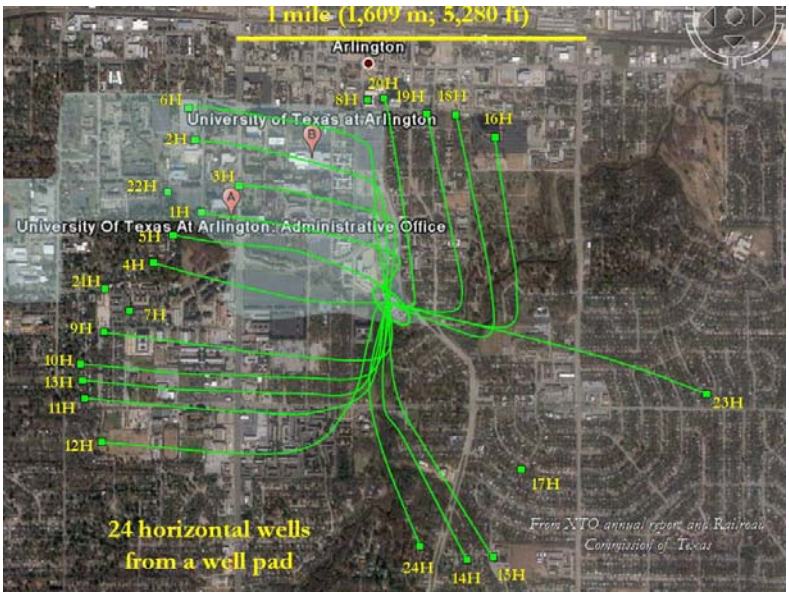

Figure 36. The drilling pad and 24 horizontal wells into the Barnett shale near UTA campus.

Results and Discussion

Gas production data for all 22 horizontal wells at UTA are presented in Figure 37. The data are also plotted in log-log space (Figure 38).

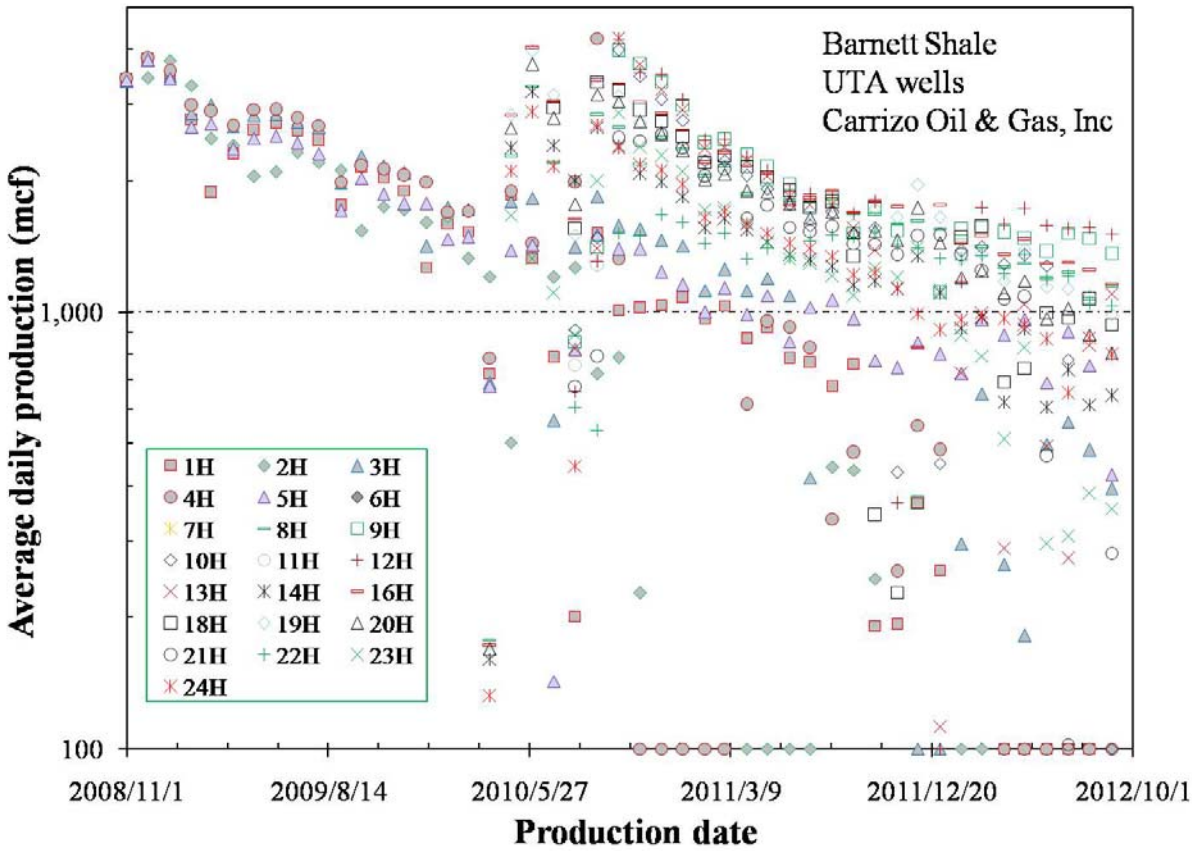

Figure 37. Gas production data from all 22 UTA wells in Tarrant County. Wells 1–6 went operational on Nov.-Dec. 2008, while the rest came online during or after April 2010. mcf: thousand cubic feet.

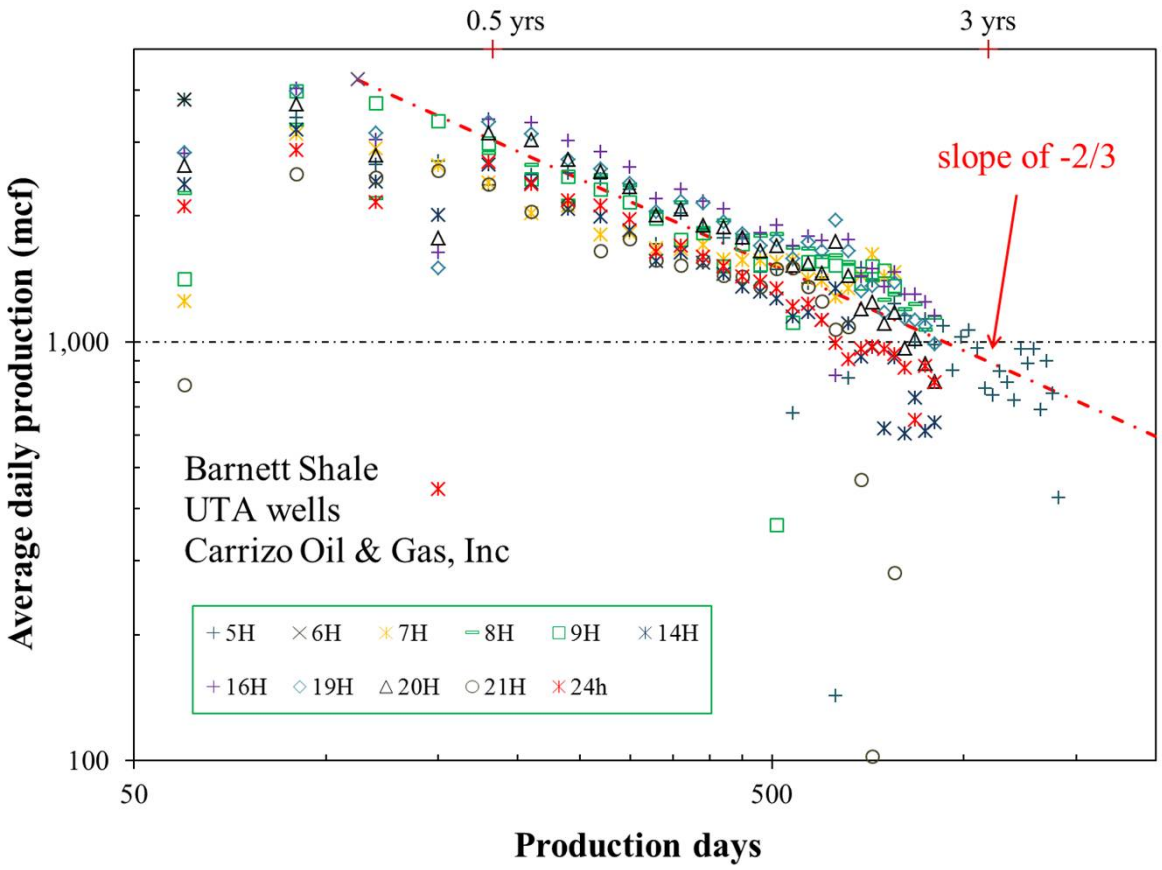

Figure 38. Gas production data in log-log scale from eleven UTA wells in Tarrant County.

Gas production data for the eight earliest producing wells in Johnson County, as well as eleven UTA wells, plotted in log-log space (Figures 38–39), show production rates declining with an exponent of approximately -2/3.

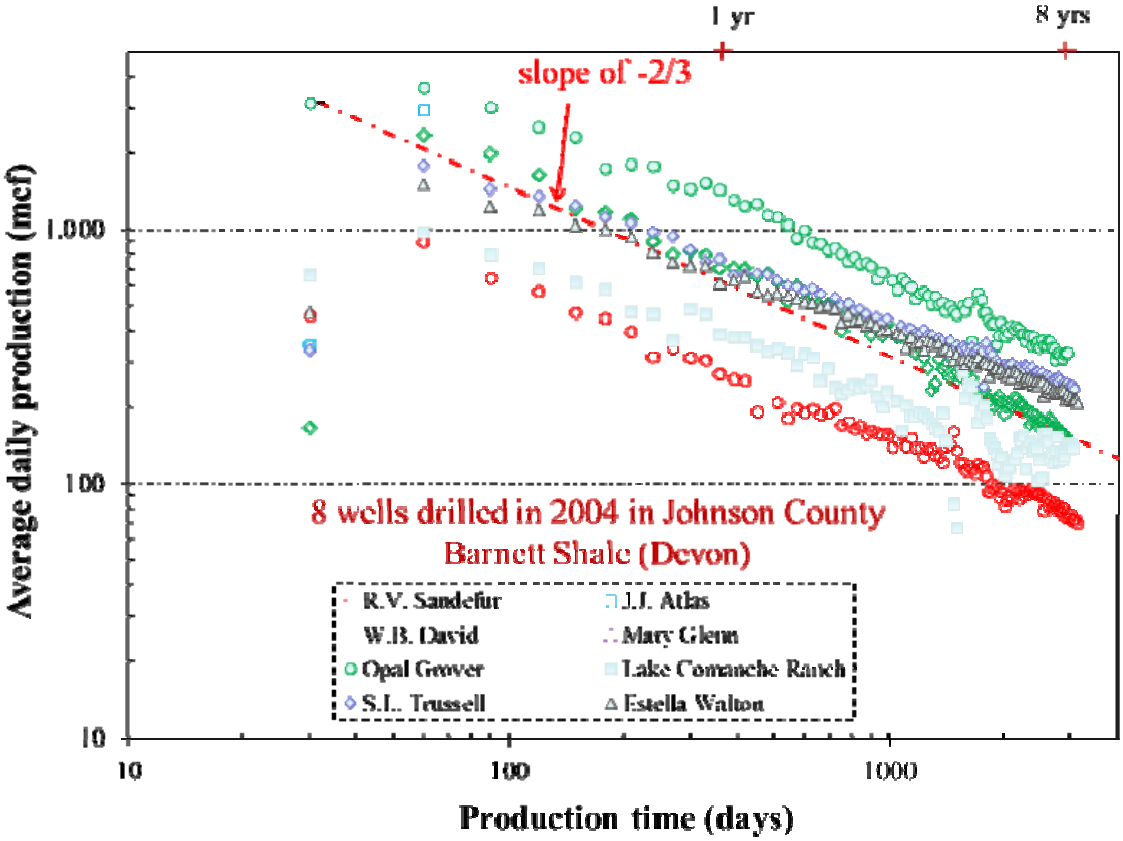

Figure 39. Gas production data in log-log scale from the eight earliest Barnett Shale wells in Johnson County.

Monteiro et al (2012) presented a mathematical model of fluid and gas flow in nanoporous media. Their model assumes that the rock consists of two components: (i) a matrix, which is more or less an ordinary porous or fractured-porous medium, and (ii) specific organic inclusions composed of kerogen. These inclusions have substantial porosity but only nanodarcy permeability, and the inclusions contain the majority of fluid: oil and gas. The model is based on the hypothesis that the permeability of the inclusions substantially depends on the pressure gradient. Their resulting formulae for the production rate of this conjectured matrix-inclusion system are presented and solved in explicit form. The formulae demonstrate that the production rate of inclusions decays with time following a power law whose exponent lies between -1/2 and -1. This value is consistent with our exponent of -2/3, considering the analog of Monterio et al.'s model of matrix-inclusion to fracture-matrix system in fractured shale formation.

Patzek et al. (2013) considered the simplest model of gas production consistent with the basic physics and geometry of the extraction process. At early times the scaling curve production rate declines as 1 over the square-root-of-time; later it declines exponentially, similar to that of Silin and Kneafsey (2012). This simple model provides a surprisingly accurate description of gas extraction from 8,294 wells in the Barnett shale. There is good agreement with the scaling theory for 2,057 horizontal wells in which production started to decline exponentially in less than 10 y. The remaining 6,237 horizontal wells in the analysis are too young to predict when the exponential decline will set in.

Our decline slope of -2/3 considers the fracture-matrix interactions, and does not have a setting-in period (e.g., 10 y for Patzek et al., 2013). A prediction without a setting-in or transition time would forecast the ultimate gas recovery no matter how long the current production has lasted. Nevertheless, our results are currently based on an analysis of limited data, and we need to analyze the gas production behavior for more producing wells to verify the application of this -2/3 decline slope on the log-log production timescale.

The extremely low permeability of shale raises the possibility that gas recovery is limited by pore topology (e.g., density of connections) rather than geometry (e.g., radius). We therefore examined production data from the perspective of percolation theory, which leads to alternative interpretations. Constraints imposed by the range of possible values of rock properties (e.g., porosity, fractal dimension) serve to eliminate some possibilities. Possibilities we examined include (1) accessible porosity and diffusion coefficient varying with distance from a fracture, resulting in anomalous diffusion; (2) a cross-over from invasion percolation to random percolation as the fracture network dewaters following hydraulic fracturing; and (3) a cross-over from 2-D to 3-D percolation behavior as the rock immediately adjacent to the fractures desorbs gas. Invasion percolation (Wilkinson and Willemsen, 1983) is the form of percolation theory that applies to dynamic changes in pore occupancy, for example when one fluid displaces another by successively invading pores. The exponents of invasion percolation are from a different "universality class" than those of random percolation, the form that describes pore connections without reference to fluid history.

In contrast to the Arps equation and the Silin and Kneasfey (2012) approach, our preliminary analysis of production decline sees many production curves exhibiting a slope transition from a moderate decline (time exponent around -0.5) to a much steeper decline after a few months or years (Ewing et al., 2013). The exponents suggest this is not a transition from linear to boundary-dominated flow. Specific values of the exponents, and the timing of apparent transitions, are affected by both matrix connectivity (as given by the crossover distance χ) and the effectiveness of the fracturing (as given by the size distribution of shale matrix equivalent spheres accessed by the resulting fracture network). We are currently examining this explanation, which appears to fit both theory and industry observations, but which is sufficiently different from existing theories that we do not want to publish it prematurely.

Conclusions

Hydrocarbon production in tight shales is technically challenging. The primary economic challenge facing producers is the relatively high cost of new wells, combined with their rapid initial depletion rate and low recovery factor. Historical average first year declines were reported to be 64% for Barnett, 77% for Haynesville, 64% for Marcellus, and 65% for Utica (Jarvie, 2011). The oil recovery factor in the middle member Bakken formation ranges from 2–5% to as high as 20% (Jarvie, 2012). The rapid production decline requires that new wells be drilled, and old wells re-fractured or re-stimulated, just to maintain production levels. As a consequence, Hughes (2013b) voiced strong concern that shale hydrocarbon production will peak by 2017, then decline by 40% per year. At SPE's Applied Technology Workshop "*Production Decline in Oil and Gas Shale Reservoirs: What Can We do to Improve the Performance?*"(March, 2013), geology was identified as the main factor that influences rapid production decline. But scientific understanding of low hydrocarbon recovery is weak and fragmented, despite the significant economic benefits that would derive from improved understanding (Howarth et al., 2011; Rogers, 2013). This work directly addresses root causes of steep decline and low overall recovery.

We used multiple approaches to investigating pore structure, and the resulting anomalous fluid migration, in Barnett shale. These experimental approaches include imbibition, tracer diffusion, mercury injection capillary pressure, and Wood's metal alloy impregnation followed by SEM imaging and LA–ICP–MS mapping. Results show that the Barnett shale pores are

predominantly in the nm size range, with a measured median pore-throat diameter of about 6 nm. The small pore size and low pore connectivity lead to extremely low diffusion rates in shale matrix, as measured using liquid tracer diffusion approach and laser ablation–ICP–MS mapping. Tracer diffusion was not well described by classical Fickian behavior; the anomalous behavior suggested by percolation theory gave a better description, as shown by imbibition tests. Wood's metal alloy intrusion and imaging/mapping showed that intruded pores are largely limited to the sample surface, another indication of low pore connectivity. In fact, Wood's metal concentrations in the interior are only about $1/1000^{th}$ of those near the sample surface, indicating that few of the interior pores are connected to the outside by a continuous pathway of at least 3.5 or 2.4 nm. Monthly gas production data for wells in the Barnett shale were obtained from the Texas Railroad Commission and DrillingInfo, and gas production decline behavior from producing wells was analyzed considering topological aspects of shale pores.

Several complementary and innovative experimental approaches to systematically studying pore connectivity in Barnett shale consistently show that connected matrix pores in shale seem to be only limited to a few mm from the sample edge, followed with a sporadic and sparse connection deeper into the sample. This poor pore connectivity and limited connected distance into shale matrix from sample edge (i.e., fracture) will lead to steep initial decline and low overall production. The overall outcomes of this project fill knowledge gaps regarding the effects of pore connectivity on diffusion-limited gas transport and steep first-year decline, as well as low overall hydrocarbon production observed in hydraulic-fractured shales.

Acknowledgements

We greatly appreciate the complimentary donation of DI Pro Database from DrillingInfo in support of this project. The assistance of Stefan Dultz (Leibniz Universität, Hannover, Germany) and Josef Kaufmann (Swiss Federal Laboratories for Materials Science and Technology) with Wood's metal intrusion and SEM imaging, of Shoichiro Hamamoto (formerly at Saitama University, now at University of Tokyo) with nitrogen sorption isotherms, and of Tongwei Zhang (BEG, University of Texas at Austin) with methane sorption isotherms, is much appreciated.

This research was supported by RPSEA through the "Ultra-Deepwater and Unconventional Natural Gas and Other Petroleum Resources" program authorized by the U.S. Energy Policy Act of 2005. RPSEA (www.rpsea.org) is a nonprofit corporation whose mission is to provide a stewardship role in ensuring the focused research, development and deployment of safe and environmentally responsible technology that can effectively deliver hydrocarbons from domestic resources to the citizens of the United States. RPSEA, operating as a consortium of premier U.S. energy research universities, industry, and independent research organizations, manages the program under a contract with the U.S. Department of Energy's National Energy Technology Laboratory. The views and opinions of authors expressed herein do not necessarily state or reflect those of the United States Government or any agency thereof.

References

Arps, J.J. 1945. Analysis of decline curves. *Trans. AIME*, 160: 228–247

Barrett, E.P., L.G. Joyner, and P.H. Halenda. 1951.The determination of pore volume and area distributions in porous substances. I. Computations from nitrogen isotherms. *J. Am. Chem. Soc.*, 73: 373–380.

Bear, J. 1972. *Dynamics of Fluid in Porous Media*, Dover, New York.

Bowker, K.A. 2007. Barnett shale gas production, Fort Worth Basin: Issues and discussion. *AAPG Bull.*, 91(4): 523-533.

Browning, J., S. Ikonnikova, G. Gülen, and S. Tinker. 2013. *Barnett shale production outlook*.165585-PA SPE Journal Paper.

Brunauer, S., P.H. Emmett, and E. Teller. 1938. Adsorption of gases in multimolecular layers. *J. Am. Chem. Soc*., 60:309–319.

Chalmers, G.R., R.M. Bustin, and I.M. Power. 2012. Characterization of gas shale pore systems by porosimetry, pycnometry, surface area, and field emission scanning electron microscopy/transmission electron microscopy image analyses: Examples from the Barnett, Woodford, Haynesville, Marcellus, and Doig units. *AAPG Bull.,*96(6): 1099–1119.

Clarkson, C.R., N. Solano, R.M. Bustin, A.M.M. Bustin, G.R.L. Chalmers, L.He, Y.B. Melnichenko, A.P. Radlinski, and T.P. Blach.2013. Pore structure characterization of North American shale gas reservoirs using USANS/SANS, gas adsorption, and mercury intrusion.

Fuel, 103: 606–616.

Comisky, J.T., M. Santiago, B. McCollom, A. Buddhala and K.E. Newsham 2011. *Sample Size Effects on the Application of Mercury Injection Capillary Pressure for Determining the Storage Capacity of Tight Gas and Oil Shales*, SPE 149432-MS.

Crowley, M.M.2003.*Physicochemicaland Mechanical Characterization of Hot-Melt Extruded Dosage Forms*. Ph.D. Thesis, College of Pharmacy, University of Texas, Austin, TX.

Curtis, J.B. 2002.Fractured shale-gas systems. *AAPG Bull.*, 86(11): 1921–1938.

Darot, M. and T. Reuschle.1999. Direct assessment of Wood's metal wettability on quartz. *Pure Appl. Geophy.*, 155(1): 119–129.

DOE (Department of Energy). 2009. *Modern Shale Gas Development in the United States: A Primer*, 116 pp.

Dullien, F.A.L. 1981.Wood's metal porosimetry and its relation to mercury porosimetry. *Powder Technol., 29: 109–116.*

Dullien, F.A.L. 1992. *Porous Media: Fluid Transport and Pore Structure* (2nd Ed.). Academic Press, San Diego.

Dultz, S., H. Behrens, A. Simonyan, G. Kahr, and T. Rath. 2006. Determination of porosity and pore connectivity in feldspars from soils of granite and saprolite. *Soil Sci.*, 171(9): 675–694.

EIA (Energy Information Administration). 2011. http://www.eia.gov/todayinenergy/detail.cfm?id=2170.

EIA (Energy Information Administration), 2014. Annual Energy Outlook 2014: With Projections to 2040. U.S. Department of Energy, http://www.eia.gov/forecasts/AEO/.

Eldieb, A.S., and R.D. Hooton. 1994. Evaluation of the Katz-Thompson model for estimating the water permeability of cement-based materials from mercury intrusion porosimetry data. *Cement Concrete Res.*, 24(3): 443–455.

Epstein, N.1989.On tortuosity and the tortuosity factor in flow and diffusion through porous media. *Chem. Eng. Sci.*, 44(3): 777–779.

Ewing, R.P., and R. Horton. 2002. Diffusion in sparsely connected pore spaces: Temporal and spatial scaling. *Water Resour. Res.*, 38: 1285, doi:10.1029/2002WR001412.

Ewing, R.P., Q.H. Hu, and C.X. Liu. 2010. Scale dependence intra-granular porosity, diffusivity, and tortuosity. *Water Resour. Res.*, 46, W06513, doi:10.1029/2009WR008183.

Ewing, R.P., C.X. Liu, and Q.H. Hu. 2012. Modeling intragranular diffusion in low-connectivity granular media. *Water Resour. Res.*, vol. 48, W03518, doi:10.1029/2011WR011407.

Ewing, R.P., Q.H. Hu, and A.G. Hunt. 2013. *Pore topology-based interpretations of gas production decline curves*. 2013 GSA South-Central Section Annual Meeting, Austin, TX, April 4-5, 2013.

Gale, J.F.W., R.M. Reed, and J. Holder. 2007. Natural fractures in the Barnett Shale and their importance for hydraulic fracture treatments. *AAPG Bull.*, 91(4): 603–622.

Gao, Z.Y. and Q.H. Hu. 2013. Estimating permeability using median pore-throat radius obtained from mercury intrusion porosimetry. *J. Geophy. Eng.,*10, 025014, doi:10.1088/1742-2132/10/2/025014.

Garboczi, E.J. 1990. Permeability, diffusivity, and microstructural parameters - A critical review. *Cement Concrete Res.*, 20(4): 591–601.

Ghanbarian, B. and A.G. Hunt.2014. Universal scaling of gas diffusion in porous media. *Water Resour. Res*., doi: 10.1002/2013WR014790.

Gommes, C.J., A.-J.Bons, S. Blacher, J. Dunsmuir, and A. Tsou. 2009. Practical methods for measuring the tortuosity of porous materials from binary or gray-tone tomographic reconstructions. *Amer. Inst. Chem. Eng. J.*, 55: 2000–2012.

Gregg, S.J., and K.S.W. Sing. 1982. *Adsorption, Surface Area, and Porosity*, 2nd ed., Academic Press, New York, 98 pp.

Graue, A., and M.A. Fernø. 2011. Water mixing during spontaneous imbibition at different boundary and wettability conditions. *J. Petrol. Sci. Eng.,* 78: 586–595.

Grathwohl, P. 1998.*Diffusion in Natural Porous Media: Contaminant Transport, Sorption/Desorption and Dissolution Kinetics*. Kluwer Academic Publishers, Boston, MA.

Grieser, W.V., R.F. Shelley, B.J. Johnson, E.O. Fielder, J.R. Heinze, and J.R. Werline. 2008. Data analysis of Barnett shale completions. *SPE J.,* SPE 100674,doi:10.2118/100674-PA.

Guidry, F.K., D.L. Luffel, and J.B. Curtis. 1996. *Development of laboratory and petrophysical techniques for evaluating shale reservoirs*. GRI (Gas Research Institute)Final Report GRI-95/0496, April 1996.

Hager, J. 1998. *Steam Drying of Porous Media*. Ph.D. Thesis, Department of Chemical Engineering, Lund University, Sweden.

Halamickova, P., R.J. Detwiler, D.P. Bentz, and E.J. Garboczi. 1995. Water permeability and chloride-ion diffusion in Portland-cement mortars - Relationship to sand content and critical pore diameter. *Cement Concrete Res.*, 25(4): 790–802.

Heller, R., and M. Zoback. 2013. *Laboratory measurements of matrix permeability and slippage enhanced permeability in gas shales*. Society of Petroleum Engineers, SPE 168856.

Hildenbrand, A. and J.L. Urai. 2003. Investigation of the morphology of pore space in mudstones - First results. *Marine Petrol. Geol.*, 20(10): 1185–1200.

Hill, R.J., E. Zhang, B.J. Katz, and Y.C. Tang. 2007. Modeling of gas generation from the Barnett Shale, Fort Worth Basin, Texas. *AAPG Bull.*, 91(4): 501–521.

Howarth, R.W., A. Ingraffea, and T. Engelder. 2011. Should fracking stop? *Nature*, 477(7364): 271–275.

Hu, Q., P. Persoff, and J.S.Y. Wang. 2001. Laboratory measurement of water imbibition into low-permeability welded tuff. *J. Hydrol.*, 242(1-2): 64–78.

Hu, Q., T.J. Kneafsey, R.C. Trautz, and J.S.Y. Wang. 2002. Tracer penetration into welded tuff matrix from flowing fractures. *Vadose Zone J.,* 1: 102–112.

Hu, Q., and J.S.Y. Wang. 2003. Aqueous-phase diffusion in unsaturated geological media: A review. *Crit. Rev. Environ. Sci. Technol.*, 33(3): 275–297.

Hu, Q.H., and X.L. Mao. 2012. Applications of laser ablation–inductively coupled plasma–mass spectrometry in studying chemical diffusion, sorption, and transport in natural rock. *Geochem. J.*, 46 (5):459–475.

Hu, Q.H., R.P. Ewing, and S. Dultz. 2012. Pore connectivity in natural rock. *J. Contam. Hydrol.*, 133: 76–83.

Hu, Q.H., and R.P. Ewing. 2013. Comment on "Energy: A reality check on the shale revolution" (Hughes, J.D., *Nature*, 21 February 2013, Vol. 494, pp. 307-308. doi:10.1038/494307a. http://www.nature.com/nature/journal/v494/n7437/full/494307a.html

Hughes, J.D. 2013a. *Drill, Baby, Drill: Can Unconventional Fuels Usher in a New Era of Energy Abundance?* Post Carbon Institute, 178 pp.

Hughes, J.D. 2013b. Energy: A reality check on the shale revolution. *Nature*, 494: 307–308.

Hunt, A.G., R.P. Ewing, and B. Ghanbarian. 2014. *Percolation Theory for Flow in Porous Media* (3rd ed.), Lect. Notes Phys. 880, Springer, Heidelberg.

Jarvie, D.M. 2010.*Worldwide shale resource plays and potential*. AAPG European Region ICE, October 17–19, 2010, Kiev, Ukraine. http://www.searchanddiscovery.com/documents/2011/80144jarvie/ndx_jarvie.pdf.

Jarvie, D.M. 2012. Shale resource systems for oil and gas: Part 1—Shale-gas resource systems, in J. A. Breyer (ed.), Shale reservoirs—Giant resources for the 21st century: *AAPG Memoir* 97, pp. 69–87.

Jarvie, D.M., R.J. Hill, T.E. Ruble, and R.M. Pollastro. 2007. Unconventional shale-gas systems: The Mississippian Barnett Shale of north-central Texas as one model for thermogenic shale-gas assessment. *AAPG Bull.*, 91(4): 475–499.

Katz, A.J., and A.H. Thompson. 1986. A quantitative prediction of permeability in porous rock. *Phys. Rev. B.,* 34: 8179–81.

Katz, A.J., and A.H. Thompson. 1987. Prediction of rock electrical conductivity from mercury injection measurements. *J. Geophy. Res.,* 92(B1): 599–607.

Kaufmann, J. 2010. Pore space analysis of cement-based materials by combined nitrogen sorption – Wood's metal impregnation and multi-cycle mercury intrusion. *Cement Concrete Comp.*, 32(7): 514–522.

King, G.E. 2012. *Hydraulic fracturing 101: What every representative, environmentalist, regulator, reporter, investor, university researcher, neighbor and engineer should know about estimating frac risk and improving frac performance in unconventional gas and oil wells*. SPE 152596.

Lawrence, G.P. 2006. Stability of soil pores during mercury intrusion porosimetry. *J. Soil Sci.,* 29(3):299–304.

Li, K. 2007. Scaling of spontaneous imbibition data with wettability included. *J. Contam. Hydrol*., 89: 218–230.

Loucks, R.G. and S. C. Ruppel. 2007. Mississippian Barnett Shale: Lithofacies and depositional setting of a deep-water shale-gas succession in the Fort Worth Basin, Texas. AAPG Bull., 91(4): 579-601.

Loucks, R.G., R.M. Reed, S.C. Ruppel and D.M. Jarvie. 2009. Morphology, genesis, and distribution of nanometer-scale pores in siliceous mudstones of the Mississippian Barnett Shale. *J. Sed. Res.*, 79(11-12): 848–861.

Luffel, D.L., and F.K. Guidry. 1992. New core analysis methods for measuring reservoir rock properties of Devonian shale. SPE 20571.

Luffel, D.L., C.W. Hopkins, and P.D. Schettler. 1993. Matrix permeability measurement of gas productive shales. SPE 26633.

Miller, R. 2010. *Gas shale evaluation: Critical elements of reservoir characterization*. Core Laboratories, Houston.

Montgomery, S.L., D.M. Jarvie, K.A. Bowker, and R.M. Pollastro. 2005. Mississippian Barnett Shale, Fort Worth basin, north-central Texas: Gas-shale play with multitrillion cubic foot potential. *AAPG Bull.*, 89(2): 155-175.

Monteiro, P.J.M., C.H. Rycroft, and G.I. Barenblatt. 2012. A mathematical model of fluid and gas flow in nanoporous media. *Proc. Natl. Acad. Sci.USA*, 109(50): 20309–20313.

Neimark, A.V., P.I. Ravikovitch, M. Gruen, F. Schueth, and K.K. Unger.1998.Pore size analysis of MCM-41 type adsorbents by means of nitrogen and argon adsorption.*J. Colloid Interface Sci*., 207(1): 159–169.

Neimark, A.V., and P.I. Ravikovitch. 2001. Capillary condensation in MMS and pore structure characterization. *Microporous Mesoporous Mater.,* 44–45: 697–707.

Nokken, M.R., and R.D. Hooton. 2003. Using pore parameters to estimate permeability or conductivity of concrete. *Mater Struc.*, doi:10.1617/s-11527-006-9212-y.

Patzek, T.W., F. Male, and M. Marder. 2013. Gas production in the Barnett shale obeys a simple scaling theory. *Proc. Natl. Acad. Sci. USA*, 110(49): 19731–19736.

Peng, S., Q.H. Hu, and S. Hamamoto.2012a. Diffusivity of rocks: Gas diffusion measurements and correlation to porosity and pore-size distribution. *Water Resour. Res.*, Vol. 48, No. 2, W02507, doi:10.1029/2011WR011098.

Peng, S., Q. Hu, R.P. Ewing, C. Liu, and J.M. Zachara. 2012b. Quantitative 3-D elemental mapping by LA-ICP-MS of basalt from the Hanford 300 area. *Environ. Sci. Technol.*, 46: 2035–2042.

Penumadu, D. and J. Dean. 2000. Compressibility effect in evaluating the pore-size distribution of kaolin clay using mercury intrusion porosimetry. *Can. Geotech. J.,* 37: 393–405.

Pflug, G. 2009. *North America shale gas overview*.http://www.transcanada.com/customerexpress/docs/presentations_general/2009_North_American_Shale_Gas_Overview_NECA.pdf

Renkin, E.M. 1954. Filtration, diffusion and molecular sieving through porous cellulose membranes. *J. Gen. Physiol.*, 38(2): 225–243.

Rogers, D. 2013. *Shale and Wall Street: Was the decline in natural gas prices orchestrated?* Energy Policy Forum, 30 pp.

Rolston, D. E., and P. Moldrup. 2002, Gas diffusivity. In J. H. Dane and G. C. Topp (Eds.), *Methods of Soil Analysis: Physical Methods. Part 4*.Soil Science Society of American, Madison, Wisconsin, , pp1113–1139.

Schembre, J.M., and A.R. Kovscek. 2006. Estimation of dynamic relative permeability and capillary pressure from countercurrent imbibition experiments. *Transp. Porous Media*, 65: 31–51.

Seaton, N. 1991. Determination of the connectivity of porous solids from nitrogen sorption measurements. *Chem. Eng. Sci.*, 46: 1895–1909.

Shahri, M.P., M. Jamialahmadi, and S.R. Shadizadeh. 2012. New normalization index for spontaneous imbibition. *J. Petrol. Sci. Eng.*, 82-83: 130–139.

Shi, D. and D.N. Winslow. 1985. Contact angle and damage during mercury intrusion into cement paste. *Cem. Concr. Res.*, 15: 645–654.

Sigal, R.F., and B. Qin. 2008. Examination of the importance of self diffusion in the transportation of gas in shale gas reservoirs. *Petrophys.*, 49(3): 301–305.

Silin, D. and T.J. Kneafsey. 2012. Shale gas: Nanometer-scale observations and well modelling. *J. Can. Petrol. Technol.,* 51(6): 464–475.

Sinha, S., E.M. Braun, Q.R. Passey, S.A. Leonardi, A.C. Wood, III, T. Zirkle, J.A. Boros, and R.A. Kudva. 2012. *Advances in measurement standards and flow properties measurements for tight rocks such as shales*, SPE 152257.

Slatt, R.M., and N.R. O'Brien. 2011. Pore types in the Barnett and Woodford gas shales: Contribution to understanding gas storage and migration pathways in fine-grained rocks. *Am. Assoc. Pet. Geol. Bull.*, 95(12): 2017–2030.

Standnes, D.C. 2010. Scaling spontaneous imbibition of water data accounting for fluid viscosities. *J. Petrol. Sci. Eng.,* 73: 214–219.

Stauffer, D., and A. Aharony.1994. *Introduction to Percolation Theory* (2nd ed.). Taylor and Francis, London.

Steward, D. 2007. *The Barnett Shale Play: Phoenix of the Fort Worth Basin*. F. Paniszczyn (ed.), The Fort Worth Geological Society, Fort Worth, Texas, 202 pp.

Swanson, B.F. 1979. Visualizing pores and nonwetting phase in porous rock. *J. Petrol. Technol.*, 31: 10–18.

Tumidajski, P.J. and B. Lin. 1998.On the validity of the Katz-Thompson equation for permeabilities in concrete. *Cement Concrete Res.*, 28(5): 643–647.

Vennard, J.K., and R.L. Street. 1975. *Elementary Fluid Mechanics*. John Wiley and Sons, Inc., New York.

Washburn, E.W. 1921. Note on a method of determining the distribution of pore sizes in a porous materials. *Proc. Nat'l Acad. Sci.,* 7: 115–116.

Webb, P.A. 2001. *An introduction to the physical characterization of materials by mercury intrusion porosimetry with emphasis on reduction and presentation of experimental data*. Micromeritics Instrument Corporation.

Wilkinson, D. and J.F. Willemsen. 1983. Invasion percolation: A new form of percolation theory. *J. Phys. A*, 16: 3365-3376.

With, G.D. and H.J. Glass. 1997. Reliability and reproducibility of mercury intrusion porosimetry. *J. Europ. Ceramic Soc.*, 17: 753–757.

Zhang, T.W., G.S. Ellis, S.C. Ruppel, K. Milliken, and R.S. Yang. 2012. Effect of organic-matter type and thermal maturity on methane adsorption in shale-gas systems. *Org. Geochem.*, 47: 120–131.

Zhao, H., N.B. Givens, and B. Curtis. 2007. Thermal maturity of the Barnett shale determined from well-log analysis. *AAPG Bull.*, 91(4): 535–549.

Impact on Producers

The main goal of this work is to improve fundamental understanding of fracture–matrix interaction and its implications in hydrocarbon recovery in shales. This process–level understanding enables economic and sustainable production from unconventional reservoirs. The focus on pore structure (geometry and connectivity) in this work in particular could have a major impact on hydrocarbon production from shale resources, because steep production decline and low recovery has been plaguing the oil and gas industry.

The oil and gas industry has paid attention to the research findings of this work, from the news report (*Petroleum Technology Transfer Council Tech Talk*, *World Oil Online*, and *EnergyWire*), and comments posted on the web versions of high–impact journals (*Nature*, *Science*). ConocoPhillips Company has expressed strong interest in the capabilities established from this work, and since May 2013 has been under negotiation to set up a contract to financially support sample characterization to better understand the production behavior in shale oil plays. The contract work started in February, 2014.

Technology Transfer Efforts

Technology transfer is an important component of this project. During the three years of the project, we have utilized various venues (peer-reviewed journal publications, conference presentations, invited presentations at academic and oil/gas industry, and media coverage) to showcase our research findings to the industry, and also seek comments and suggestions to better align the research to industry needs. As detailed below, our track record of technology transfer is extremely impressive for the funding level of the project.

Peer-Reviewed Journal Publications

(*student 1st author; corresponding author)

1. Gao*, Z.Y., and Q.H. Hu. 2013. Spontaneous imbibition affected by median pore-throat diameter obtained from mercury intrusion porosimetry. *Journal of Petroleum Science and Engineering* (submitted)
2. Gao*, Z.Y., and Q.H. Hu. 2013. Wettability and pore connectivity of Barnett shale at different depths: Investigation from directional spontaneous imbibition and mercury intrusion porosimetry. *Journal of Petroleum Science and Engineering* (submitted).

3. Webber, B., P. Corbettc, K.T. Sempled, U. Ogbonnayad, W.S. Teele, C.A. Masiellof, Q.J. Fisherg, J.J Valenza II, Yi-Qiao Song, and Q.H. Hu.2013. An NMR study of porous rock and biochar containing organic material. *Microporous and Mesoporous Materials*, 178:94-98.
4. Gao*, Z.Y., Q.H. Hu,and H.C. Liang. 2013. Gas diffusivity in porous media: Determination by mercury intrusion porosimetry and correlation to porosity and permeability. *Journal of Porous Media*. 16(7): 607–617.
5. Gao*, Z.Y., and Q.H. Hu. 2013. Estimating permeability using median pore-throat radius obtained from mercury intrusion porosimetry. *Journal of Geophysics and Engineering*. 10, 025014, doi:10.1088/1742-2132/10/2/025014.
6. Hu, Q.H., R.P. Ewing, and S. Dultz. 2012. Pore connectivity in natural rock: Evidence and implications. *Journal of Contaminant Hydrology*, 133: 76-83.
7. Peng*, S., and Q.H. Hu. 2012. LA-ICP-MS calibration with internal standard and modified constant-sum methods. *American Journal of Analytical Chemistry*, 3: 168-174.

Conference Presentations

(* student 1st author; *presenting author*)

1. *Hu, Q.H.*, Z.Y. Gao, and R.P. Ewing. Characterization, Diffusion, and Sorption in Shale. Session "Geochemistry and Reactive Transport in Shale Nanopores", Division of Geochemistry, 247th *ACS* National Meeting & Exposition, Dallas, TX, March 16–20, 2014 (invited speaker).
2. *Gao*, X.B.*, Q.H. Hu, Z.Y. Gao, and R.P. Ewing. Pore Accessibility and Connectivity of Mineral and Kerogen Phases for Shales. 2013 Fall Meeting of the American Geophysical Union, San Francisco, CA, December 9–13, 2013.
3. *Ewing, R.P.*, A.G. Hunt, and Q.H. Hu. Pore Accessibility and Molecular size: A Percolation Approach. 2013 Fall Meeting of the American Geophysical Union, San Francisco, CA, December 9–13, 2013.
4. *Hu, Q.H.*, Z.Y. Gao, R.P. Ewing, S. Dultz, J. Kaufmann, S. Hamamoto, B. Webber, and M. Ding. Multiple Approaches to Characterizing Nano-Pore Structure of Barnett Shale. 2013 Fall Meeting of the American Geophysical Union, San Francisco, CA, December 9–13, 2013.
5. *Gao*, Z.Y.*, and Q.H. Hu. Experimental Investigation of Reservoir Rocks by Spontaneous Imbibition and Mercury Intrusion Porosimetry. 2013 Fall Meeting of the American Geophysical Union, San Francisco, CA, December 9–13, 2013.
6. *Hu, Q.H.*, Z.Y. Gao, and R.P. Ewing. Diffusion-Limited Fracture-Matrix Interaction and Gas Recovery in Barnett Shale. Session "A Comprehensive Look at Hydraulic Fracturing for Hydrocarbon Recovery and Other Purposes", 2013 Geological Society of America Annual Meeting and Exposition, Denver, CO, October 27–30, 2013.
7. *Hu, Q.H.*, Z.Y. Gao, and R.P. Ewing. Diffusion-Limited Fracture-Matrix Interaction and Gas Recovery in Barnett Shale. Session "A Comprehensive Look at Hydraulic Fracturing for Hydrocarbon Recovery and Other Purposes", 2013 Geological Society of America Annual

Meeting and Exposition, Denver, CO, October 27–30, 2013.

8. *Hu, Q.H.*, Z.Y. Gao, and R.P. Ewing. Tortuous Migration Pathways and Gas Production Behavior of Barnett Shale. Division of Energy and Fuels. The 246th ACS National Meeting and Exposition, Indianapolis, Indiana, September 8–12, 2013 (invited speaker).
9. *Hu, Q.H.*, and X.B. Gao. Pore structure, Diffusion, and Gas Recovery in Barnett Shale. 1st Joint Scientific Meeting, Geological Society of China and Geological Society of America, Chengdu, Sichuan Province, China, June17–19, 2013.
10. *Hu, Q.H.*, Z.Y. Gao, S. Peng, R.P. Ewing, S. Dultz, S. Hamamoto, and B. Webber. Multiple Approaches to Characterizing Pore Structure in Barnett Shale. 2013 GSA South-Central Section Annual Meeting, Austin, TX, April 4–5, 2013.
11. *Gao*, Z.Y.*, and Q.H. Hu. Evaluating the Wettability of Different Reservoir Rocks by Spontaneous Imbibition. 2013 GSA South-Central Section Annual Meeting, Austin, TX, April 4–5, 2013.
12. *Ewing, R.P.*, Q.H. Hu, and A.G. Hunt. Pore Topology-Based Interpretations of Gas Production Decline Curves. 2013 GSA South-Central Section Annual Meeting, Austin, TX, April 4–5, 2013.
13. *Hu, Q.H.*, S. Dultz, S. Hamamoto, and R.P. Ewing. Multiple Approaches to Characterizing Pore Structure in Natural Rock. 2012 Fall Meeting of the American Geophysical Union, December 3–7, 2012, San Francisco, CA.
14. Peng*, S., *Q.H. Hu*, and R.P. Ewing. Gas Recovery in Fractured Barnett Shale. 2012 Fall Meeting of the American Geophysical Union, December 3–7, 2012, San Francisco, CA.
15. Gao*, Z.Y.,*Q.H. Hu*, and R.P. Ewing. Nanopores and Tortuous Pathways in the Barnett Shale. 2012 Fall Meeting of the American Geophysical Union, December 3–7, 2012, San Francisco, CA.
16. *Hu, Q.H.*, S. Peng, Z.Y. Gao, and R.P. Ewing. Pore Structure and Gas Recovery in Barnett Shale. Session "Petroleum Geology: Past to Present, From the Appalachias to China, Pore Size to Basin Scale Topics", 2012 Geological Society of America Annual Meeting and Exposition, November 4–7, 2012, Charlotte, NC.
17. *Hu, Q.H.*, Z.Y. Gao, S. Peng, and R.P. Ewing. Low Pore Connectivity in Barnett Shale. Session "Hydrogeology and Geochemistry of Shales", 2012 Geological Society of America Annual Meeting and Exposition, November 4–7, 2012, Charlotte, NC.
18. *Gao*, Z.Y.*, and Q.H. Hu.Application of Mercury Intrusion Porosimetry in Pore Structure Characterization. 2012 AAPG Southwest Section Convention, May 19–22, 2012, Fort Worth, TX.
19. *Hu, Q.H.*, Z.Y. Gao, S. Peng, and R.P. Ewing.Pore Structure Inhibits Gas Diffusion in the Barnett Shale.2012 AAPG Southwest Section Convention, May 19–22, 2012, Fort Worth, TX.

20. *Hu, Q.H.*, Z.Y. Gao, S. Peng, and R.P. Ewing.Pore Structure and Chemical Diffusion in the Barnett Shale. 2011 Fall Meeting for American Geophysical Union, December 13–17, 2011, San Francisco, CA.
21. *Peng**, *S.,* Q.H. Hu, and S. Hamamoto.Rock diffusivity: Gas Diffusion Measurements and its Correlation to Porosity, Pore-size Distribution, and Permeability. 2011 Fall Meeting for American Geophysical Union, December 13–17, 2011, San Francisco, CA.
22. *Hu, Q.H.*, X.G. Liu, S. Dultz, R.P. Ewing, and H.D. Rowe**.** Fracture-matrix interaction and gas recovery in the Barnett Shale. AAPG/SEG/SPE Hedberg Conference "Critical Assessment of Shale Resource Plays", December 5–10, 2010, Austin, TX.

Invited Presentations to Academia and the Oil/Gas Industry

11/8/2013 "Sustainable Shale Hydrocarbon Development Affected by Environmental and Production-Decline Issues". Department of Civil and Environmental Engineering, the University of Texas, San Antonio, TX.

10/24/2013 "Sustainable Shale Hydrocarbon Development Affected by Environmental and Production-Decline Issues". Energy & Geoscience Institute, the University of Utah, Salt Lake City, UT.

10/7/2013 "Sustainable Shale Hydrocarbon Development Affected by Environmental and Production-Decline Issues". The University of Arizona, Tucson, AZ.

3/15/2013 "Pore Structure: Characterization and Implications in Hydrocarbon Recovery". Geoscience and Reservoir Engineering, ConocoPhillips, Houston, TX.

2/26/2013 "Pore Structure in Porous Media: Implications in Hydrocarbon Recovery of Fractured Shales. Los Alamos National Laboratory, Los Alamos, NM.

2/12/2013 "Pore Structure and Hydrocarbon Recovery in Fractured Shales". SPE Reservoir Study Group, Texas Christian University, Fort Worth, TX.

2/7/2013 "Pore Structure and Hydrocarbon Recovery in Fractured Shales". University of Texas at Arlington, Arlington, TX.

10/4/2012 "Shale Gas Production: Issues and Pore Structure Effect". Department of Earth and Environmental Sciences, University of Texas at Arlington, Arlington, TX.

9/14/2012 "Pore Structure and Gas Recovery in Fractured Barnett Shale". Bureau of Economic Geology, University of Texas at Austin, Austin, TX. http://www.beg.utexas.edu/abs/abstract.php?d=2012-09-14

9/13/2012 "Fluid Flow and Mass Transport in Shale". Shale Gas Research Group, Applied Reservoir Technology Division, B.J. Services (Baker Hughes Inc.), Tomball, TX.

6/12/2012 "Pore Structure and Fluid Flow in Natural Rock". Department of Petroleum Engineering,Texas A&M University, College Station, TX.

Media Coverage

Comment on "Impact of Shale Gas Development on Regional Water Quality" (Vidic, R.D., S.L. Brantley, J.M. Vandenbossche, D. Yoxtheimer, J D. Abad, *Science*, 17 May 2013, Vol. 340, No. 6134, pp. 1235009-0. doi:10.1126/science.1235009). July 29, 2013. http://comments.sciencemag.org/content/10.1126/science.1235009#comments.

Comment on "Energy: A reality check on the shale revolution" (Hughes, J.D., *Nature*, 21 February 2013, Vol. 494, pp. 307-308. doi:10.1038/494307a. http://www.nature.com/nature/journal/v494/n7437/full/494307a.html

Comment on "Drawbacks to natural gas" (Souther, S., *Science*, 12 April 2013, Vol. 340, No. 6129, pp. 141-141. doi:10.1126/science.340.6129.141-a. http://comments.sciencemag.org/content/10.1126/science.340.6129.141-a

"Geology is behind in steep decline in dry gas wells", November 6, 2012, *EnergyWire*, Environment and Energy Publishing, LLC. http://www.wecc.biz/committees/BOD/TEPPC/SPSG/Lists/Events/Attachments/348/Geology%20is%20behind%20rapid%20decline%20in%20dry%20gas%20wells.pdf

"Barnett shale gas production rises despite lower rig count", *World Oil Online*, Vol. 233, No. 2. http://www.worldoil.com/February-2012-Barnett-shale-gas-production-rises-despite-lower-rig-count.html.

Appendix 1

Geochemical properties of samples used in this work (Harold Rowe, Texas BEG, personal communication).

Sample	Mid-depth (ft.)	Classification	TOC	SiO_2	Al_2O_3	CaO	Na_2O	MgO	K_2O	Fe_2O_3	MnO	TiO_2	P_2O_5
								%					
BL-1-6	7109.04	Upper Barnett	3.85	66.7	9.04	7.56	0.508	1.09	1.52	2.80	0.018	0.461	0.835
BL-1-35	7136.77	Forestburg limestone	1.42	26.6	5.22	31.5	0.406	2.14	0.762	1.62	0.016	0.242	0.159
BL-1-70	7168.94	upper part of Lower Barnett	2.41	45.9	9.13	16.9	0.439	1.89	1.14	4.39	0.035	0.444	0.290
BL-1-99	7200.54	upper part of Lower Barnett	4.01	54.4	10.5	11.4	0.592	1.08	1.61	2.56	0.020	0.483	1.17
BL-1-122	7219.54	upper part of Lower Barnett	3.78	60.0	11.2	7.71	0.857	1.04	1.81	2.72	0.019	0.543	1.95

Sample	Mid-depth (ft.)	Classification	Ba	Co	Cr	Cu	La	Mo	Nb	Ni	Pb	Rb	Sr	Th
								mg/kg						
BL-1-6	7109.04	Upper Barnett	161	8	233	25	29	11	10	79	12	68	314	10
BL-1-35	7136.77	Forestburg limestone	128	0	50	12	28	2	6	25	13	28	544	9
BL-1-70	7168.94	upper part ofLower Barnett	132	9	133	17	33	4	7	51	13	42	573	9
BL-1-99	7200.54	upper part of Lower Barnett	155	7	237	28	35	10	10	95	12	69	571	10
BL-1-122	7219.54	upper part of Lower Barnett	232	9	236	32	37	12	12	104	12	78	553	11